Magnetic Resonance Guided Focused Ultrasound (MRgFUS) for targeted drug delivery in Diffuse Intrinsic Pontine Glioma (DIPG)

Saira Banu Alli

Submitted in accordance with the requirements for the degree of Doctor of Philosophy

The University of Leeds
School of Medicine
Faculty of Medicine and Health

January 2022

In Chapters 2 and 4, the candidate Saira Alli is responsible for the study conception and design, data collection, analysis and interpretation of results and was the first author of the subsequent manuscript.

In Chapter 3, the candidate Saira Alli generated the DIPG mouse models and was responsible for their data collection and analysis. The MRI experiments pertaining to BBB integrity were completed by Dr Joji Ishida and the candidate Saira Alli was a second author on this manuscript.

The candidate confirms that the work published is her own and that appropriate credit has been given where reference has been made to the work of others.

This copy has been supplied on the understanding that it is copyright material and that no quotation from the thesis may be published without proper acknowledgement.

The right of Saira Alli to be identified as Author of the above specified work has been asserted by her in accordance with the Copyright, Designs and Patents Act 1988.

Acknowledgements

Lastly, I would like to say a special thank you to my family – my partner Mia for supporting me throughout these years of studentship and my children Eden and Elias who have brought me unparalleled love and fulfilment.

Academic Output

Peer reviewed publications

1. **Alli S**, Figueredo C, Rutka JT et. al. Brainstem Blood Brain Barrier Disruption using Focused Ultrasound: A Demonstration of Safety and Enhanced Doxorubicin Delivery. *J Controlled Release, 2018 July 10; 281:29-41*

2. Ishida J, **Alli S**, Bondoc A et al. MRI-guided focused ultrasound enhances drug delivery in experimental diffuse intrinsic pontine glioma. *J Controlled release*, 2021 Feb 10; 330:1034-1045

3. **Alli S**, Isik S, Rutka JT. Microscopic removal of craniopharyngioma: endoscopic and transcranial techniques for complication avoidance. *J Neurooncol*. 2016 Nov;130(2):299-307

International Presentations

1. MRI Guided Focused Ultrasound: Towards clinical translation in DIPG. *DIPG Collaborative Meeting, Sydney, Australia, September 2019. (Invited Speaker)*

2. MRI Guided Focused Ultrasound: The potential in DIPG. *TD2 Paediatric Brain Tumour Foundation Meeting, San Francisco, May 2019. (Invited Speaker).*

3. MRI guided focused ultrasound. A demonstration of safety in the brainstem. *Society of Neuro-oncology Paediatric Meeting, New York, June 2017.*

4. MRI guided Focused Ultrasound: Targeted drug delivery in DIPG. *DIPG Collaborative Meeting, Cincinnati, Ohio, May 2017.*

5. MRI guided focused ultrasound as a delivery method for DIPG. *International Society of Paediatrc Neuro-oncology, Liverpool, June 2016.*

Grants and Awards

1. International Society of Paediatric Neuro-oncology Cure Starts Now Snap Grant, 2016 (50,000 US$) – "MRI guided focused ultrasound as a delivery method for DIPG"

2. DIPG Collaborative Grant, 2017 (100,560 US$) – "MRI guided focused ultrasound: towards clinical translation in Diffuse Intrinsic Pontine Glioma.

Abstract

Background

Magnetic Resonance Image-guided Focused Ultrasound (MRgFUS) has been used to achieve transient BBB opening without tissue injury. Delivery of a targeted ultrasonic wave causes an interaction between administered microbubbles and the capillary bed resulting in enhanced vessel permeability. The use of MRgFUS in the brainstem has not previously been shown but could provide value in the treatment of tumours such as Diffuse Intrinsic Pontine Glioma (DIPG) where the intact BBB has contributed to the limited success of chemotherapy.

The focus of this study was to determine whether the use of MRgFUS in this eloquent brain region could be performed without histological injury and functional deficits. Thereafter, we wished to determine if we could enhance brainstem delivery of an effective chemotherapeutic against patient derived DIPG cell lines when combined with MRgFUS *in vivo*.

Further to this, we sought to develop two pre-clinical murine models of DIPG; a genetically engineered RCAS/Tv-a model (Nestin tva: RCAS PDGFB, RCAS H3.3K27M, p53KO) and a patient derived xenograft (SU-DIPG XVII) to compare their respective BBB permeability and thus determine their suitability for pre-clinical MRgFUS delivered therapeutics.

Lastly, recognising the need for multi-drug therapy, we set out to identify a highly synergistic drug combination therapy that could be tested in our chosen pre-clinical model.

Methods

Female Sprague Dawley rats were randomised to one of four groups: 1) Microbubble administration but no MRgFUS treatment; 2) MRgFUS only; 3) MRgFUS + microbubbles; and 4) MRgFUS + microbubbles + cisplatin. Physiological assessment was performed by monitoring of heart and respiratory rates. Motor function and co-ordination were evaluated by Rotarod and grip strength testing. Histological analysis for haemorrhage (H&E), neuronal nuclei (NeuN) and apoptosis (cleaved Caspase-3) was also performed. A drug screen of eight chemotherapy agents was conducted in three patient-derived DIPG cell lines (SU-DIPG IV, SU-DIPG XIII and SU-DIPG XVII). Doxorubicin was identified as an effective agent. NOD/SCID/GAMMA (NSG) mice were subsequently administered with 5mg/kg of intravenous doxorubicin at the time of one of the following: 1) Microbubbles but no MRgFUS; 2) MRgFUS only; 3) MRgFUS + microbubbles and 4) no intervention. Brain specimens were extracted at 2 hours and doxorubicin quantification was conducted using liquid chromatography mass spectrometry (LC/MS). BBB opening was confirmed by contrast enhancement on T1-weighted MR imaging and positive Evans blue staining of the brainstem.

Nestin-tv-a;p53$^{fl/fl}$ received brainstem injection of transfected DF-1 chicken fibroblast cells containing RCAS-PDGFB, RCAS Cre and RCAS H3.3K27M at postnatal day 2. NOD/SCID/GAMMA mice received brainstem injections of the SU-DIPG XVII cell line. Following tumour development, radiological and histological assessment was performed. A further measure of SU-DIPG XVII BBB permeability was performed by comparison of brainstem doxorubicin uptake with control mice.

A zero induced potency (ZIP) analysis of synergy was conducted between doxorubicin and several drugs classified as either PARP inhibitors, HDAC inhibitors or TK inhibitors in patient derived DIPG cell lines.

Results

Normal cardiorespiratory parameters were preserved across all cohorts of rats. Grip strength and Rotarod testing demonstrating no decline in performance across all groups. Histological analysis showed no evidence of haemorrhage, neuronal loss or increased apoptosis.

Doxorubicin demonstrated cytotoxicity against all three cell lines and is known to have poor BBB permeability. Quantities measured in the brainstem of NSG mice were highest in the group receiving MRgFUS and microbubbles (431.5 ng/g). This was significantly higher than in mice who received no intervention (7.6 ng/g).

On comparison of the Nestin-tva and SU-DIPG XVII mouse models, both demonstrated the key molecular markers of DIPG. However, the SU-DIPX XVII PDX model more faithfully recapitulated the disease due to a diffuse pattern of tumour growth seen histologically and the preservation of the BBB. In contrast, the Nestin-tva model resulted in a well circumscribed and avidly enhancing tumour.

Drug synergy analysis identified the PARP inhibitors Niraparib and Talazoparib as having potency and highly synergistic activity with doxorubicin *in vitro*. Tyrosine kinase inhibitors (TKI) and Histone Deacetylase inhibitors (HDACi) demonstrated a largely antagonistic action with doxorubicin.

Conclusion

Our data demonstrates both the preservation of histological and functional integrity of the brainstem following MRgFUS for BBB opening and the ability to significantly enhance drug delivery to the region. We have developed the SU-DIPG XVII PDX model which exhibits a diffuse brainstem tumour with an intact BBB as a potential

pre-clinical model of DIPG for MRgFUS delivered therapeutics. In addition, we have identified a potent and synergistic *in vitro* drug combination therapy of doxorubicin and the PARP inhibitors Niraparib and Talazoparib to further assess *in vivo.*

Taken together, these findings give significant promise to the treatment of brainstem tumours using MRgFUS delivered therapeutics

Contents

List of Tables

List of Figures

1 Introduction

This thesis describes work undertaken to assess Magnetic Resonance guided focused ultrasound (MRgFUS) and its ability to achieve Blood Brain Barrier (BBB) disruption as a potential method of drug delivery for the brainstem tumour Diffuse Intrinsic Pontine Glioma (DIPG). This study was based on the hypothesis that the BBB is a key limiting factor to intra-tumoral drug penetration and has contributed to the limited gains in patient survival. There is certainly a consensus agreement amongst those who study the disease that an effective drug delivery platform will be instrumental to effective treatment. As a drug delivery system, MRgFUS is non-invasive, can achieve focal BBB disruption and could be readily translated given the existence of a clinically deliverable system. Recognising the breadth of both clinical and pre-clinical experience in the field of focused ultrasound in Toronto, Canada I chose to conduct most of my research here.

My approach was to firstly confirm the feasibility and safety of the technique in this eloquent location and to then determine if brainstem drug uptake could be enhanced. Following this, I sought to recreate a pre-clinical murine model of DIPG with a preserved BBB with which to test potential therapeutics. Lastly, recognising the need for combination drug treatments, I wanted to identify a synergistic drug combination for pre-clinical testing. The goal of this work is clinical translation, starting with a phase I/II clinical trial of an MRgFUS delivered drug and the hope to some day offer patients with this devastating disease a life prolonging treatment.

The thesis begins with an overview of DIPG and the underlying molecular events that give rise to the disease. I will then discuss existing pre-clinical models and the

treatment challenges that currently exist. I will provide a comprehensive review of CNS drug delivery strategies and introduce MRgFUS, highlighting its current use and specific benefits. I will also briefly discuss several drug classifications of new molecular therapeutics and the rationale for their use in DIPG with an explanation of the potential benefits of drug synergy. Lastly, I will outline the aims and objectives of my PhD work.

1.1 Brain tumours in children

The Central Nervous System is the most common site of cancer in the paediatric population (age 0-14) with an average age adjusted incidence rate of 5.54 per 100,000 population in the United States. Brain tumours are consequently the fourth most common cause of death in this age group[1]. For those children who do survive, the clinical implications of these tumours and their treatment is profound with patients experiencing a combination of physical and cognitive deficits along with endocrine and cerebrovascular dysfunction[2]. As a result, significant efforts have been made to reduce treatment related morbidity with risk-adapted treatment protocols, rationalisation of craniospinal irradiation, utilisation of proton beam treatment and novel therapies[3]. Over the preceding decade, advances in the field of molecular biology have provided a greater understanding of the underlying genetic events giving rise to these tumours which has had significant implications in identifying new tumour subtypes as well as potential molecular targets.

The classification of brain tumours underwent significant revision by the World Health Organisation, (WHO) in 2016[4]. The classification represented the first time that molecular data was incorporated into brain tumour diagnosis with prior versions based primarily on microscopy characteristics[5]. Within this classification system and the subsequent update

in 2021[6], brain tumours affecting children were broadly categorised as; diffuse astrocytic and oligodendroglial tumours, other astrocytic tumours, ependymal tumours, choroid plexus tumours, neuronal and mixed neuronal-glial tumours, tumours of the pineal region, embryonal tumours, germ cell tumours and tumours of the sellar region[2]. Within the diffuse astrocytic and oligodendroglial category, a new entity was described – "diffuse midline glioma, H3K27M mutant". This represents a small group of tumours characterised by K27M mutations in the histone *H3* gene *H3F3A* or related *HIST1H3B* gene with a diffuse growth pattern and midline location (thalamus, brain stem and spinal cord). Incorporated within this glioma subtype is the tumour Diffuse Intrinsic Pontine Glioma, (DIPG).

1.2 Diffuse Intrinsic Pontine Glioma (DIPG)

DIPG is a brainstem glioma arising from the ventral pons in children between the ages of 3 – 10 years[3]. It constitutes 10-15% of all new paediatric brain tumour diagnoses and is the leading cause of brain tumour related death in children[7]. Patients typically present with a short history and relatively rapid progression of cranial nerve deficits, ataxia and long tract signs. Symptoms of raised intracranial pressure may also be apparent due to pontine enlargement resulting in obstructive hydrocephalus. The diagnosis is confirmed by magnetic resonance imaging (MRI) demonstrating a diffuse and expansile tumour centred in the pons which appears hyperintense on T2-weighted and FLAIR images, iso- or hypointense on T1 weighted images and has little to no contrast enhancement[8]. Although not often present at diagnosis, leptomeningeal dissemination and proximal spread of the tumour has been identified at autopsy[9]. The high degree of accuracy with which these tumours can be diagnosed radiologically has historically meant that surgical biopsy was not performed due to the potential morbidity. Although biopsy is now a more frequent occurrence there are differing practices across institutions due to the ethical dilemma of

the low individual patient benefit weighed against the altruistic desire to obtain tumour samples for research and the potential of benefiting future patients. Indeed, it has been the acquisition of tumour material from autopsy and biopsy samples over the preceding decade that has led to our current molecular understanding of DIPG.

The eloquent location and diffuse growth pattern of these tumours precludes the ability to surgically resect them. Chemotherapy agents have been shown to have limited efficacy although very few studies have been conducted to assess combination therapies. Whether used in an adjuvant, neoadjuvant or concomitant manner with radiation therapy, chemotherapy has not conferred a survival benefit[7,10]. Radiation therapy therefore remains the only treatment modality shown to confer benefit. Clinical response is apparent with the improvement of neurological symptoms and signs often allowing the reduction or cessation of steroid therapy. This however does not correlate with radiological response which remains poorly defined and highly variable. No difference in the response to radiation has been identified whether delivered in a hyperfractionated, hypofractionated or conventional manner and similarly, radiosensitizing agents have not enhanced efficacy[3,7,10].

The lack of therapeutic options for patients portends a poor prognosis with a median overall survival of 11 months and only 10% of patients are alive at 2 years[11].

1.2.1 Molecular genetics of DIPG

Focused efforts to safely perform stereotactic biopsies in addition to establishing protocols for autopsy retrieval of tumour tissue in patients with DIPG led to the acquisition of the first tumour specimens which were subsequently utilised for genomic profiling. As such, over the preceding decade significant progress has been made in the molecular characterisation of DIPG.

A seminal finding in DIPG was that of histone mutations found to be present in 80% of DIPG tumours[12]. Histones are highly alkaline proteins found within eukaryotic cell nuclei that form a complex with DNA to form chromatin. A nucleosome is a structural unit of chromatin consisting of an octamer of two copies each of histones H3, H4, H2A and H2B wrapped 1.7 times by 147 base pairs of DNA[13]. Chromatin has a critical role in all cellular processes including cell division, gene expression, DNA replication and DNA repair. It is therefore tightly regulated with post transcriptional modifications of DNA (in the form of DNA methylation) and histones with both the histone tails and histone cores being subject to phosphorylation, acetylation, methylation, ubiquitination, sumoylation and isomerization.

Several variants of histone H3 exist in humans with the most highly related being H3.1, H3.2 and H3.3 which differ in their structure by between one to four amino acid substitutions within their histone core. These substitutions determine which chaperone proteins associate with the histones and therefore where they are inserted and removed from the nucleosome[14]. The H3.3 variant is expressed constitutively, being inserted at regions of high transcriptional activity by the histone cell cycle regulator (HIRA) and at silent or heterochromatic loci by the death-domain associated protein (DAXX) in complex with the transcriptional regulator -thalassemia/mental retardation syndrome X-linked (ATRX)[15]. It is the most prevalent of the H3 variants in neurons and is encoded by two genes , *H3F3A* and *H3F3B*. H3.1 and H3.2 however are cell cycle dependent with their deposition arising in S-phase or during DNA repair[16]. An example of their cell cycle regulation is illustrated by the fact that the replication factor, proliferating cell nuclear antigen (PCNA) is known to recruit the chaperone CAF1 (chromatin assembly factor) to newly synthesized DNA which in turn incorporates H3.1 into nucelosomes[17,18].

The histone H3K27M mutation is the result of a somatic adenine to thymine transversion in the *H3F3A* gene on chromosome 1q causing a substitution of methionine for lysine 27 of histone H3.3. An analogous mutation was identified in *HISTIH3B*, encoding an isoform of histone H3.1 but occurring with a lower frequency. These mutations arise within the highly conserved N-terminal tail of histone H3, in close proximity to where the tail exits the globular histone core of the nucleosome. H3K27 can be mono-, di- or tri-methylated or acetylated with the Polycomb group (PcG) of proteins regulating the methylated states. Polycomb Repressive Complex 2 (PRC2) catalyzes the methylation of H3K27 by its Enhancer of Zeste Homologue 1 or 2 (EZH1/2) methyltransferase domain[1920]. EZH1 and 2 proteins are members of the "SET" domain class which consists of three developmentally important genes; Su(var)39, EZH2 and Trithorax. These genes share a highly conserved S-adenosyl methionine (SAM) dependent methyltransferase domain and therefore use SAM as a cofactor in their methyltransferase activity. Whereas the acetylated state of H3K27 is associated with transcriptional activation, the H3K27 di and tri-methylated state at gene promoters is correlated with transcriptional repression[21]. The latter arises through recruitment of Polycomb repressive complex 1, (PRC1) which causes chromatin compaction and catalyses H2AK119 monoubiquitination which results in inhibition of transcriptional elongation[22].

The presence of the K27M mutation in either H3.1 or H3.3 results in a global decrease in H3K27me2 and K3K27me3[23,24] and therefore transcriptional derepression. Distinct patterns of DNA methylation and RNA expression are observed depending on whether H3.1 or H3.3 is mutated[25] and this in part may be due to H3.3 being more commonly inserted at sites of increased transcriptional activity. The ability of less than 20% of mutant H3 protein to cause a global decrease in H3K27me3 has led to the tethering

and sequestration hypothesis. The model describes high affinity binding of H3K27M to PRC2 with H3K27M both blocking methylation by PRC2 and sequestering it, therefore resulting in a global reduction of K27me3 within cells[26,27]. However, within DIPG some loci actually demonstrate a gain of H3K27me3 and this is particularly true for genes with known cancer association, such as cyclin dependent kinase inhibitor 2A (*CDKN2A*) and Cyclin-dependent kinase 6 (*CDK6*)[23]. In the case of CDKN2A, this results in the repression of the *p16/INK4A* tumour suppressor in a mechanism that is dependent upon EZH2 function[28].

The interaction between H3K27M and PRC2 is gradually being elucidated as complex and dynamic with more recent work by Reinberg et. al. demonstrating that DIPG has comparatively low levels of PRC2 with K27M being present in excess (upto 100 fold) and that following the induction of H3.3K27M, PRC2 can bind to it at novel sites on the nucleosome that are not occupied by PRC2 in a WT setting[29]. However, this binding is transitory with PRC2 being excluded from K27M containing regions at later time points. It is hypothesised that the resultant transcriptional change following loss of K27me3 promotes K36 methylation (H3K36me2) which is a known PRC2 antagonist and occurs adjacent to H3K27M when in cis formation. Therefore, PRC2 inhibition extends beyond the time at which it is bound to H3K27M. In addition, the group showed that following interaction of H3K27M and PRC2, there is a persistent decrease in the activity of the complex which they attribute to either a defect in SAM turnover causing delayed catalysis or an inhibition of EZH2 automethylation which subsequently influences the activity of PRC2 on chromatin[30].

The group went further to hypothesize that the allosterically activated form of PRC2 preferentially binds H3K27M and that the resultant decreased activity of PRC2

causes a global loss of H3K27me3 repressive domains. However, despite its reduced activity, PRC2 is still recruited to strong polycomb foci in H3K27M cells at which it causes a focal gain of H3K27me3 at these sites. This thereby explains focal regions of gain of H3K27me3 on a background of more global H23K27me3 loss in DIPG.

Ultimately, these findings suggest that the H3K27M mutation results in a complex reprogramming of the epigenome causing a differential gene expression profile. Functionally this has been shown to result in altered cell cycle control and inhibition of tumour cell autophagy in addition to potentially limiting the response to radiation therapy[31]. It is a key example of how mutations within chromatin- associated proteins can cause an aggressive cancer despite seemingly simple oncological genomes[32]. Certainly, the presence of a H3 mutation confers a poorer prognosis for patients than those harbouring non-histone mutated tumours[33].

The H3.1 K27M mutation is exclusively found in DIPG whereas H3.3 mutations are linked to midline and supratentorial laterally located Glioblastoma Multiforme (GBM)[33,34]. Within DIPG, the H3.1 and H3.3 subgroups are mutually exclusive and have clinical and prognostic implications, conferring different median overall survival (OS), phenotype and radiation response[33,35]. Histone H3.3 is associated with a shorter median OS of 9 months (15 months in H3.1), greater metastatic recurrence and an inferior response to radiation therapy[33]. However, the mutation alone is insufficient to cause tumorigenesis *in vivo* and additional mutations are believed to synergise, causing an early transformational event in DIPG.

Additional mutational events in DIPG are broadly categorized as those affecting cell cycle regulatory genes (TP53/PPM1D) and growth factor related pathways

8

(ACVR1/PI3KR1). These are regarded as obligate partner mutations to H3K27M mutations in order to achieve gliomagenesis[36].

ACVR1 is the third most mutated gene in DIPG and is located on chromosome 2q23-q24[37]. It is found in 20 – 32% of DIPG patients[38]. Clinically they are associated with younger female patients with a longer overall survival time[39]. Mutations in the gene were initially shown to cause Fibrodysplasia ossificans progressiva (FOP), a rare autosomal dominant musculoskeletal disease which results in endochondral heterotopic ossification within soft tissues such as fascia, ligaments, tendons and skeletal muscle[40]. The gene encodes ALK2, a receptor serine/threonine kinase which is a member of the BMP/TGFß receptor family that consists of an extracellular N-terminal ligand-binding domain, a transmembrane domain, an intracellular glycine-serine rich (GS) domain and a protein kinase (PK) domain[40]. It forms a heterotetrameric receptor complex[41] with receptor-ligand binding resulting in the phosphorylation of SMAD1/5/8 proteins by the receptor's kinase domain[42]. These SMADs then assemble with SMAD4 and enter the nucleus where they bind promoters of downstream targets including ID-1-3, SMAD6, SMAD7, SNAIL and HEY1[43].

ACVR1 mutations in DIPG consist of specific base changes causing seven different amino acid substitutions; R206H (20%), Q207E (2%), R258G (13%), G328E (24%), G328V (28%), G328W (4%) and G356D (9%). These mutations are located in the glycine-serine rich or protein kinase domains and notably, more than half occur at the glycine at position 328. The result of these mutations is an increase in BMP signalling thought to be due to an altered interaction between ACVR1 and FKBP12. FKBP12 is a cytoplasmic FK506-binding protein 1A (*FKBP1A/FKBP12*) that functions as a negative regulator of type I receptors by

binding their GS domain and suppressing their kinase activity thereby preventing receptor activation. However, when ligand binding causes receptor complex formation, BMP type II phosphorylates the GS domain of the type I receptor causing release of FKBP12 and activation of the type I receptor[40]. ACVR1 mutations found in FOP have been shown to effect the inhibition of the type I receptor by FKBP12 causing dysregulation of BMP signaling resulting in an endothelial-to-mesenchymal transition[44,45].

BMP signaling has a role in CNS development in the embryonic, postnatal and adult brain[37]. Patients with FOP have been shown to have structural intracranial malformations involving the brainstem and cerebellum with some specifically showing abnormal soft tissue masses of the ventral pons, brainstem and fourth ventricle[46].

The role of ACVR1 in DIPG oncogenesis has not yet been elucidated. What is known is that the co-expression of mutant ACVR1 and H3.1 K27M work in an additive manner to increase BMP signaling with resultant increased levels of phosphorylated SMAD1 and ID protein expression[39,47]. Mutant *Acvr1* (R206H, G328V, G328E) alone in mouse models did not produce tumours but requires additional genetic mutations found in the human disease (H3.1-K27M, PI3-kinase and PDGFA over-expression) to produce glioma-like tumours[48].

Within DIPG, ACVR1 specifically co-localises with tumours expressing H3.1 rather than H3.3 mutations. It is hypothesized that ACVR1 mutations result in activation of BMP signaling which neurodevelopmentally drives stem cell progenitors toward an astrocytic differentiation with the more astrocytic phenotype conferring extended survival over those DIPG tumours with a more oligodendroglial phenotype[49,50]. It may however be the case that *ACVR1* mutations are participating in a yet undetermined non canonical role in DIPG oncogenesis[39].

Mutations within the tumour suppressor p53 (TP53) have been found to arise in upto 77% of DIPGs. They occur in both H3.3mutated and wild type H3 DIPGs and commonly co-occur in tumours with PDGFR amplification[35,38]. Commonly mutated regions are within the DNA-binding or tetramerization domains which result in altered conformation or premature truncation[51–53]. Mutations in the gene are believed to work in concert with H3.3 K27M, enabling the latter to influence the epigenome whilst evading cell death[54]. More recent work has suggested TP53 mutations as the major cause of radiation resistance in DIPG with TP53 mutant DIPGs demonstrating a reduced response to radiation, earlier relapse and worse prognosis[55]. A CHK1 inhibitor, Prexasertib, was subsequently shown to demonstrate synthetic lethality with ionizing radiation in TP53 mutant DIPG cells.

An additional common genomic occurrence in DIPG is that of mutations and amplifications of platelet-derived growth factor (PDGF) and platelet derived growth factor receptor alpha (PDGFRA) which result in receptor tyrosine kinase (RTK) signaling along both the PI3K/AKT/mTOR and mitogen activated protein kinase (Ras/Raf/MEK/ERK) pathways[56]. These genomic alterations result in constitutively active PDGFRA with resultant auto-phosphorylation of the tyrosine kinase domain, activation of downstream effectors and subsequent phosphorylation of Tyr742 which interacts with the regulatory PI3K p85α subunit or phosphorylation of Tyr720 and Tyr754 which activates SHP2 (Src homology-2 domain containing phosphatas), a regulator of the MAPK pathway[57–59].Over activation of PDGFRA is integral to the generation of gliomas *in vivo* and is believed to be an early event in the development of DIPG[60–62]. There is a strong association with H3.3K27M mutations[38]. PDGFRA amplified tumours display an oligodendroglial subtype that confers a more clinically aggressive and chemotherapy resistant phenotype[49].

Additional mutations resulting in constitutive activation of the PI3K/mTOR signaling pathway have been identified in DIPG and include PIK3CA (12%), PIK3R1 (8%), TSC2 (2%), RPTOR (1%), MTOR (1%) as well as inactivating mutations of PTEN, a tumour suppressor and negative regulator of the pathway[51,63]. As such, the pathway is the integral driver of oncogenesis in H3K27M mutant DIPGs. The downstream effector is activated AKT which triggers multiple pathways required for cell survival and metabolism. Interestingly, intra-tumoral localization of *PIK3CA* and *PIK3R1* differs with the latter co-localising with H3.3K27M and the former being present in all tumour subpopulations[38]. Both however assist tumour development by promotion of angiogenesis.

AKT signalling is activated by multiple means beyond that of PIK3 mutations in DIPG, including over expression of PDGF and VEGF, making it an important therapeutic target[64]. Approaches to managing pathway over-activation have included mTOR inhibitors and multi-tyrosine kinase inhibitors[65,66]. The challenge for single agent inhibitors however, is that of redundancy and compensatory signalling within the activated pathway[64,67].

A rarer mutation to arise in DIPG is that of the serine-protein kinase Ataxia-telangiectasia mutated (ATM) which co-occurs with H3.3K27M in 10% of cases[51]. ATM is a member of the PI3K family and is recruited to sites of double stranded DNA breaks (DSBs) where its autophosphorylation and therefore activation facilitates DNA end resection prior to DNA repair via homologous recombination[68]. Downstream effects include regulation of cell cycle checkpoints via p53 phosphorylation at Ser15 and checkpoint kinase 2 (CHK2) phosphorylation at Thr68[69]. The consequences of ATM mutations in DIPG are not known but likely reduce the efficacy of checkpoint inhibition therefore contributing to genome instability[53].

1.2.2 Pre-clinical models of DIPG

The recognition of DIPG as a separate entity to cortical high grade gliomas and the identification of the key molecular drivers underpinning the disease led to a focus on developing more accurate pre-clinical models. Prior models were transplantation based and involved the stereotactic injection of rat glioma or human glioblastoma cell lines into the murine brainstem[70–75]. Although the efficacy of ionizing radiation was demonstrated in such a glioma based model[73] and was a clinically translatable finding, the therapeutic effects of temozolamide in these models was not replicated in clinical trials[75–77]. Temozolamide is an alkylating chemotherapeutic agent and is commonly used in the treatment of adult high-grade glioma. in This supported the need for models that exhibit both the genetic alterations found in DIPG as well as the appropriate brainstem microenvironment.

An early DIPG specific model was a xenograft utilising cells obtained from a patient autopsy that were subsequently cultured *in vitro* and stereotactically implanted into the hindbrain of immunodeficient neonatal mice[78]. The ability to grow human autopsy derived cells in neural stem cell culture was a key step in the generation of this model and the first time that this was successfully achieved in DIPG. However, it was recognised that autopsy derived cells have likely undergone prior irradiation and possible chemotherapy, thereby potentially displaying genetic or epigenetic alterations not in keeping with the primary tumour. As such, cells harvested from diagnostic biopsy samples were then used to develop *in vitro* cell cultures and DIPG xenograft models[23,66,79–81]. Although these cells reflect a single biopsy site within a tumour, it has previously been shown that DIPG tumours, in contrast to adult HGG's, demonstrate spatial conservation of the key defining mutations including K27M, ACVR1, PIK3CA, FGFR1 and MET[82].

In addition to xenograft models of DIPG, genetically engineered mouse models (GEMM) have been developed. These models enable the development of tumours from their presumed cell of origin, within their own microenvironment and in an immunocompetent animal. The RCAS (replication-competent avian sarcoma-leucosis virus long terminal repeat with splice acceptor)/tumor virus A (TVA) modelling system has been used to develop a DIPG mouse model[83]. The RCAS virus enters cells via the TVA receptor. Given that the receptor is ordinarily found in avian cells but not mammalian cells, transgenic mice have been generated to express the TVA receptor under the control of cell-type specific promoters[84]. Once the virus enters a mammalian cell, a cDNA copy of the viral genome is made and is subsequently incorporated into the host genome during cell division[85]. To generate tumour models, insertions of cDNA encoding proto-oncogenes or dominant negative tumour suppressor genes can be added to the RCAS virus with the key limitation being that of size. Inserts larger than 2.8 kb are either lost or result in truncation mutations or limited viral replication[85]. RCAS virus propagation in culture is commonly done using the DF1 chicken fibroblast cell[86].

Becher *et al.* were the first to use the RCAS-Tva system to develop a brainstem glioma model which used germline Ink4a-ARF loss and PDGFB overexpression localised to Nestin expressing cells in the neonatal mouse pons[83]. These cells were previously identified to be the likely cell type of origin of DIPG[54]. Subsequent evolutions of the brainstem glioma model were generated by injecting RCAS PDGFB, RCAS- Cre and RCAS-H3.3K27M producing cells into the brainstem of neonatal Nestin-Tva; p53 floxed mice[26]. This was the first model to display key genetic alterations in DIPG and determined the resultant global loss of H3K27me3 subsequent to the K27M mutation.

The RCAS model also highlights the ability to achieve multiple genetic mutations in a single mouse model that are expressed in both a tissue and temporal specific manner. By having TVA receptor expression under the control of a Nestin promoter, mutations can be targeted to Nestin-expressing cells of the mouse brainstem which are present during early neonatal life. Such temporal and spatial localisation has been shown to be of significance with RCAS generated brainstem gliomas demonstrating higher levels of the transcription factor Pax3 compared to cortical tumours[87]. This finding is mirrored in 40% of DIPG patient tumours, exclusive of ACVR1 mutations, resulting in both cellular proliferation and an inhibition of apoptosis .

Limitations of the model include the insert capacity of the RCAS vector in addition to each model thus far reflecting only one DIPG subtype. The model also works on the assumption that tumour initiation occurs in early neonatal life, with more recent literature suggesting that the initiating events may well arise in utero[88,89]. Furthermore, genetic mutations are introduced simultaneously suggesting that H3.3K27M assists in tumour formation in the model whereas in the clonal evolution of DIPG, H3K27M is known to be the primary initiating mutation[36,82].

1.2.3 Treatment challenges

Prior to the determination of the underlying molecular events in DIPG, numerous clinical trials were undertaken using combination chemotherapy and radiation regimes[10]. These treatment selections were based on availability, safety and efficacy in other solid tumours. DIPG specific pre-clinical tools were yet to be developed and unsurprisingly, these treatments failed to confer greater benefit than that of conventional fractionated radiation. Furthermore, study designs were heterogenous and critical appraisal highlighted inconsistent eligibility criteria and an absence of statistical endpoints[10].

The ability to biopsy DIPG and the subsequent efforts to maintain and grow these cells *in vitro* as well as the development of increasingly sophisticated DIPG animal models has provided a means of evaluating potential targeted therapeutics[81,90–92]. However, an ongoing challenge for systemically administered agents is that of adequate drug delivery to the tumour. This is a multi-faceted process requiring a favourable pharmacokinetic profile in the systemic circulation (low clearance, unbound state), the ability to cross the blood-brain barrier (BBB) and then to maintain sufficient intra-tumoral concentrations in order to exert a treatment effect without causing concurrent CNS toxicity.

The BBB has historically been regarded as a static structure consisting of specialised endothelial cells linked by impenetrable tight junctions, astrocytic foot processes and pericytes. The tight junctions and associated proteins are known to limit paracellular diffusion therefore agents wishing to cross the BBB must do so either by diffusion through the endothelial cells or via channels and active transport carriers. Favourible agents are lipophilic with a low molecular weight and low hydrogen binding potential[93].

However, the BBB is now recognised to be a highly complex and dynamic interface that communicates with surrounding cells of the CNS resulting in adaptations designed to protect against disease but that can inadvertently perpetuate it[94]. Brain endothelial cells are in constant crosstalk with astrocytes, microglia, neurons, mast cells, pericytes and circulating immune cells[95]. These cells in combination are referred to as the neurovascular unit (NVU), clarifying that although astrocytes and pericytes ultimately provide barrier function, there is significant communication between the body and the brain influencing this.

Transporters are an additional feature of the BBB and can be classified as "blood-to-brain transporters" and "brain-to-blood transporters" [94]. The former enable the uptake of water soluble molecules such as glucose as well as larger molecules into the CNS. The binding affinity of the ligand to its carrier molecule is a key determinant in the success of uptake. In instances where transport against a concentration gradient is required, ATP mediated carriers are used for active transport. "Brain-to-blood transporters" or efflux transporters exist for a wide range of substances and have been shown to restrict the passage of chemotherapeutic agents across the BBB. Examples of efflux transporters include P-glycoprotein (Pgp), breast cancer resistance proteins and multidrug resistance proteins. The distribution of transporters throughout the brain is highly variable with some having a localised anatomical/regional distribution[96,97].

The failure of systemically administered chemotherapeutic agents in the treatment of patients with DIPG is believed to be in part due to regional differences in the BBB and in particular, the presence of a more robust BBB in the pons. This "super BBB" was demonstrated in a study conducted in non-human primates in which temozolamide was administered intravenously and *in vivo* microdialysis was used to sample the extracellular fluid of the cerebral cortex and pons as well as the plasma and CSF[98]. Temozolamide levels in the CSF were found to be consistently lower in the pons than the cerebral cortex and CSF indicating a more limited penetration in the pons.

Furthermore, DIPG remains a predominantly non-contrast enhancing tumour suggesting that there is integrity of the blood:tumour barrier despite it being a highly malignant tumour. This is unique for CNS tumours, with the majority demonstrating areas of prominent contrast enhancement. However, even within these tumours, there are regional differences in the extent of BBB disruption[99]. In addition, there is no clinical

evidence to correlate the presence of contrast enhancement in CNS tumours with enhanced drug penetration or response to chemotherapy. In DIPG, radiation treatment often results in tumour enhancement but adjuvant chemotherapy in this context has not improved outcomes

Intrathecal administration of chemotherapeutic agents has historically been used in the treatment of CNS tumours but currently has limited indications for use. Agents administered this way must overcome the blood:csf barrier which consists of modified epithelial cells at the choroid plexus and arachnoid membrane[100]. CSF is produced by the choroid plexus within the ventricles and circulates through the ventricular system and then into the cisterns and subarachnoid space which contains blood vessels. Several factors limit the ability of drugs delivered within the CSF to penetrate the brain tissue. Firstly, CSF is continually produced and reabsorbed, resulting in dilution of the drug and elimination into the blood stream and CNS lymphatics. Drug distribution within the CSF is also inhomogeneous, affected by gravity as well as the viscosity of CSF which may be higher in the presence of tumours and leptomeningeal disease[93].

Once penetration of a drug is achieved beyond these barriers, the next hurdle is movement through the brain parenchyma and extracellular space to reach the site of the tumour. Here, a drug must remain in its active form for a sufficient period to exert a treatment effect. This is particularly challenging given that movement through parenchyma is limited to several millimetres[101] and may be reduced further in highly cellular tumours with raised intratumoral pressures. The extracellular space, (ECS) although similar in composition to CSF possess additional extracellular matrix molecules which can impede diffusion by both their viscosity and negative charge. This results in the apparent diffusion coefficient of small molecules in the ECS being 40% of that in free

solution[102]. In the diseased brain, additional factors such as oedema, ischaemia, osmolarity and cellularity will further restrict the movement of molecules in the ECS[101].

1.3 Approaches to Drug Delivery in the CNS

A diverse range of approaches to circumvent the BBB and enhance drug delivery to the CNS have been explored and this continues to be an evolving field of research. An early approach for patients with DIPG was the administration of high dose systemic chemotherapy with the premise that high circulating blood concentrations would linearly enhance CNS concentrations. This approach acknowledged the steep dose-response curves of conventional chemotherapeutics and assumed that drug passage across the BBB is by simple diffusion and not influenced by transport or carrier molecules that have the potential for saturation. Similarly, the effect of efflux transporters was not known. The resultant toxicity of high systemic drug exposure led to these treatments being poorly tolerated with no change in disease course or patient outcomes[103–106].

1.3.1 Regional drug delivery

Local or regional drug administration of cytotoxic agent for CNS tumours has also been attempted. Intra-arterial (IA) administration was proposed to reduce the systemic drug distribution of an administered agent and therefore deliver a higher first pass dose to the targeted tumour whilst also delivering it more rapidly. Intra-carotid (IC) infusion restricts the initial volume of distribution to one cerebral hemisphere and a small volume of injected drug can achieve a high initial arterial concentration with a low total dose, resulting in decreased systemic toxicity[107]. It is most suited to drugs that are administered in their active form, ordinarily undergo significant first pass metabolism or whole body clearance and are delivered in conditions of low regional arterial blood flow when the regional extraction is high (i.e. lipophilic or BBB permeable)[108].

19

A disadvantage of IA therapy and specifically of intra-carotid drug delivery is the high resting blood flow to the brain which constitutes 15-20% of the cardiac output. This results in greater dilution of the drug by arterial blood and potentially decreases the drug transit time through the cerebral circulation if cerebral blood volume is not increased in a proportional manner[108]. In addition, the advantage of intracarotid drug delivery is most profound with shorter durations of drug infusion as they lead to a higher peak regional concentration[109].

There are also significant risks associated with IA drug delivery, including that of embolism, haemorrhage, vascular injury and local toxicity in the form of encephalopathy and retinal injury[108]. Local toxicity in part is attributed to drug streaming which is the uneven distribution of drugs in the arterial stream that results in differing drug concentrations within the arterial distribution[110]. Factor contributing to streaming include the rate of infusate, the type of catheter used for drug delivery and its proximity to arterial branching[111]. A proposed method of reducing streaming effects is a pulsed intracarotid infusion which delivers the drug during diastole to increase mixing[112].

Hori *et al.* conducted a small study delivering the water soluble nitrosurea, 1-(4-amino-2-methyl pyridimine-5-yl)-methyl-3-(2-chloroethyl)-3-nitrosurea hydrochloride (ACNU) to 3 cohorts of patients with malignant brain tumours. ACNU was administered intravenously (cohort 1), intra-arterial into the internal carotid artery (cohort 2) and intra-arterial with mannitol co-administered to disrupt the BBB (cohort 3). The study demonstrated no significant difference in the level and pharmacokinetic profile of ACNU in the blood but did show a significant difference in the amount of ACNU detected in tumour tissue with cohort 3 showing the most and cohort 1 showing the least[113]. Whether the statistically significant differences in the quantity of drug in the tumour tissue were

sufficient to result in meaningful differences in clinical outcome was not assessed. However, three phase III randomised studies were published between 1992 and 2006 assessing outcomes in patients administered IA ACNU and the bis-chloro-ethyl nitrosurea (carmustine, BCNU)[114–116].

Shapiro *et al.* conducted a study consisting of 315 patients with newly resected malignant gliomas (glioblastoma, anaplastic astrocytoma and oligodendroglioma) who were randomised to receiving either IV or IA carmustine (200mg/sq m every 8 weeks) with or without the addition of IV fluorouracil[114]. Median survival was 11.2 months for the IA carmustine group and 14 months for the IV carmustine group. The probability of surviving two years was 13% for the IA group and 25% for the IV group and fluorouracil was not found to impact survival. Patients with anaplastic astrocytoma were found to have a significantly reduced survival time with IA carmustine administration and the study was terminated due to the toxicity of IA carmustine which resulted in ipsilateral blindness (15%) and severe leukoencephalopathy (10%). Kochii et al. compared IA ACNU with IV ACNU administration in 82 patients with newly diagnosed GBM. IA ACNU was administered a maximum of 3 times (every 6 weeks) followed by IV administration thereafter. No significant difference was found in overall survival, progression free survival or complication rate in either treatment arm[115].

In 2006, Imbesi *et al*. randomised adult patients with newly diagnosed glioblastoma who had underwent extensive surgical resection to receiving either IA (17 patients) or IV (16 patients) ACNU at a dose of 80-100mg/m^2. Treatments were repeated every 5-8 weeks for a minimum of 2 and maximum of 14 cycles. Despite demonstrating 4-fold higher ACNU levels in the tumour bed when delivered by the IA route, there was no significant difference in either total survival time or time to progression between the two

groups[116]. The authors highlight that it is difficult to know whether the lack of effectiveness was rather due to the intrinsic resistance of GBM to nitrosureas.

Definitive conclusions regarding the efficacy of IA therapy are difficult to determine from these studies. The largest and earliest study by Shapiro et al. demonstrated a concerning adverse effect profile of IA administration of BCNU which is likely related to the specific neurotoxicity of the drug itself given that ACNU appeared to be safer in the subsequent smaller studies. A particular challenge of assessing delivery methods in an incurable tumour such as GBM is the inability to distinguish whether a failure in outcome is due to the method of delivery or the inadequacy of the therapy delivered. Interpretation is also difficult in protocols that utilise combined drug treatments in addition to radiation therapy or protocols with a limited number of IA delivered doses. Optimal drug dosing and duration is often not achieved due to reasons including drug toxicity, the technicalities of administration and at times, a short life expectancy[116]. In addition, IA therapies are most effective in unilateral tumours with a predominant single vessel blood supply. Both GBM and DIPG are diffusely infiltrating tumours and studies involving the former included patients with bilateral supratentorial lesions.

IA drug delivery for DIPG would require administration into the vertebral arteries which converge to form the basilar artery. This convergence is unique, with most intracranial vasculature taking a divergent course, and results in more significant streaming effects. Modelling has shown an unequal distribution of drug to one half of the brainstem ipsilateral to the side of drug infusion[117]. This in turn can result in significant toxicity at areas of high drug delivery and no treatment effect at sites with limited drug delivery[118,119]. Despite this, IA delivery has been tried in a small group of patients with brainstem tumours. Fujiwara *et al.* administered chemotherapy into the vertebral artery

22

of 4 patients, aged 5 - 59 years with brainstem gliomas that were histologically confirmed

to be grade 2 (n = 3) or 3 (n=1) astrocytomas. Treatments protocols were unfortunately

heterogenous with ACNU alone being administered to 1 patient, ACNU with cisplatin being

administered to 2 patients and carboplatin given to 1 patient. Survival ranged from 14 to

36 months with adverse treatment effects being limited to nausea and vomiting. Given

the small patient cohort and predominantly low grade histology, conclusions cannot be

made regarding a survival benefit. There is currently no clinical trial data assessing IA drug

delivery in patients with DIPG.

An additional regional therapy for brain tumours is the direct placement of

chemotherapy agents in the tumour bed which is performed at the time of surgical

debulking. This can take the form of gels, beads or extended release wafers. The most

successful intra-cavitary treatment thus far has been that of Gliadel wafers (Arbor

Pharmaceuticals, Atlanta GA), in the treatment of adult GBM. The wafers consist of

biodegradable copolymers impregnated with carmustine. The first phase III multi-centre

double-blind trial was conducted in 222 patients with recurrent GBM and demonstrated

increased median overall survival with Gliadel wafers as compared to placebo wafers (31

vs 23 weeks, hazard ratio 0.67, 95% confidence interval 0.51-0.90, p=0.006). Given these

findings, two subsequent phase III trials were conducted to assess the efficacy of Gliadel

wafers in newly diagnosed high grade gliomas. Both trials reported a statistically

significant increase in median survival (39.9 weeks to 58.1 weeks, p = 0.012 and 11.6

months to 13.9 months, log rank, p = 0.03)[120–122]. This resulted in subsequent FDA approval

for their use in recurrent GBM in 1997 and for newly diagnosed HGG in 2003.

Despite these findings, Gliadel wafers are rarely utilised in the treatment of high

grade glioma due to their adverse effect profile which includes a CSF leak rate of 5% vs

0.8% in the placebo treated group and delayed intracranial hypertension in 9.1% vs 1.7%[121].

Given the nature of DIPG and the inability to surgically resect these tumour, such regional therapies have not been used to date and are a less likely option in terms of a drug delivery method moving forward.

1.3.2 Inhibition of BBB efflux transporters

A novel approach that has been trialled in patient with DIPG is that of inhibition of the BBB drug efflux transporter, P-glycoprotein. The transporter is found on the luminal surface of brain capillary endothelial cells and has been shown to exclude a variety of anti-cancer drugs from the CNS[123–125]. Additional sites of the transporter include the choroid plexus, liver, kidney, intestines as well as cancer cells resistant to therapy[126]. Due to the widespread location of the transporter and inhibitory agents being non selective, their use results in widespread receptor inhibition which in turn impairs systemic drug elimination[127]. A study in non-human primates administered doxorubicin alone or doxorubicin with the Pgp inhibitor, cyclosporin A (Cys A) noted a 42% reduction in doxorubicin clearance in the latter group[126]. This raises concerns for systemic toxicity and the group chose to reduce the dose of doxorubicin administered with Cys A to compensate for its reduced clearance. The study did not find an appreciable increase in levels of CSF doxorubicin when co-administered with Cys A despite the altered pharmacokinetics indicating peripheral Pgp inhibition.

A phase I study conducted in patients with DIPG administered an induction chemotherapy regime of daily oral etoposide for 21 of 28 days and escalating doses of IV vincristine on days 1, 8, 15, 22, 29 and 36[128]. Cys A was administered as a loading dose for 2 hours prior to the administration of IV vincristine and then continued as an infusion for

36 hours. Cys A levels were monitored to achieve a targeted steady state level previously identified to effectively modulate Pgp. Radiation therapy was delivered during the induction chemotherapy regime and both were followed by a maintenance regime comprising six 28 day cycles of chemotherapy. Vincristine and Cys A were again administered on day 1 and oral etoposide administered of days 1-21.

Seven patients were enrolled but the study underwent early closure due to dose-limiting neurotoxicity. This included seizures, altered consciousness and midbrain dysfunction requiring intubation. Radiologically, tumour necrosis, haemorrhage and progression of diffuse white matter changes were identified in patients with adverse events. Interestingly, two of the three patients who experienced seizures had pre-existing white matter changes in the brain which is not characteristic of DIPG and may indicate a concurrent pathological process contributing to their seizures. However, Cys A has a known association with neurotoxicity causing seizures and encephalopathy[129]. The study also did not demonstrate any improvement in median survival (11 months).

1.3.3 Convection enhanced delivery (CED)

Convection Enhanced Delivery (CED) is a novel drug delivery method that has come to prominence in DIPG over the preceding two decades. It requires the placement of one or more microcatheters into a tumour, attached to a pump that instils a drug solution at a persistent hydraulic pressure[130]. The resultant field of distribution is that of a sphere or ellipse and is determined by the infusion volume and tissue type. The use of hydraulic pressure achieves a larger volume of distribution than that which would be achieved by simple diffusion.

The ability to stereotactically place one and then multiple catheters into the brainstem was a significant development in the advancement of CED for DIPG. Barua et al.

were the first to implant a robotic-guided catheter into the pons of a 5 year old boy with DIPG and via serial daily infusions were able to deliver 49.8 ml of carboplatin to 95% of the tumour volume[131]. Recognising the need for a robust catheter system that can remain in situ for a prolonged time frame and be utilised for repeated dosing, the group developed several iterations of catheter design. A key feature of their system was that of a titanium bone anchored port designed to deter bacterial adhesion, prevent skin overgrowth and achieve both cutaneous and osseous integration. This addressed many of the challenges associated with implantable devices; avoiding catheter migration, reducing the risk of infection and enabling the use of an external pump device which can achieve higher infusion rates as compared to a subcutaneously implanted one[132]. Carbothane catheters (inner diameter 0.35mm, outer diameter 0.6mm) were identified as having a significantly lower blockage rate compared to fused silica and PEEK catheters[133] and adjustable recessed step catheters were found to reduce the extent of drug reflux and provide flexibility in altering the volume of distribution[134]. The group have demonstrated the use of a multi catheter device in the treatment of a patient with recurrent GBM[135] and have presented their experience of a phase I study of carboplatin in patients with DIPG using four catheters inserted in the pons (2 trans-frontal and 2 trans-cerebellar) [unpublished work]. More recently, a pre-clinical study has been conducted demonstrating the feasibility of CED using water soluble panobinostat to the rodent and porcine pons[136].

The key challenge of CED is the optimisation of several variables to achieve an adequate volume of distribution (Vd) to treat the tumour whilst avoiding infusion related injury to healthy tissues. An ideal infusate is one that has stability in the interstitial space. Lipophilic agents may be effluxed too quickly as they are prone to entering the vasculature more rapidly. Agents may also bind or be degraded by the extracellular matrix[137].

Molecules should be small enough to travel within the interstitial space and interestingly, a higher viscosity can improve the Vd as it is less prone to reflux[138]. Given these desired properties of a CED agent, several modifications of agents have been tested, including albumin coating and the generation of nanoparticle formulations[139,140].

Reflux is the phenomenon of retrograde movement of fluid along the outside of the catheter which can reduce the Vd in CED. Features of the catheter can influence the extent of reflux, with smaller diameter catheters and those with a porous or recessed step design reducing the degree of reflux[134,141]. Properties of the tumour or tissue can also affect the Vd. Within the brain, white matter has been shown to have less resistance to extracellular bulk flow compared to grey matter with both tissue types having regional differences in architecture and size of the extracellular space[142,143]. These differences are characterised by defining the relationship between the volume of infusion (Vi) and the volume of distribution (Vd)[144,145]. If the numerical value of this ratio (Vd/Vi) is known for a specific tissue type, it can be used to determine the volume of infusate in a treatment protocol.

Tumours can also have unique features affecting the Vd with CED. They commonly have high interstitial pressures due to a combination of increased cellularity and neo-vascularisation with the latter causing an increase in blood and serum leakage into the tumour[146]. With such high intra-tumoral pressures, this results in a steep pressure differential at the tumour border which can drive the flow of infusate into the surrounding parenchyma. Brain tumours may also have regions of disrupted BBB resulting in a more rapid efflux of drug from the CNS[130]. Regions of necrosis or cystic degeneration may also act as a sink and prevent the infusate adequately dispersing throughout the tumour.

Similarly, depending on the location of the tumour, infusate may leak into the ventricles or sulci[147].

Given the variety of factors that can influence the Vd, the ability to predict and visualise drug delivery via CED has become a specific focus. iPlan Flow is a software package developed by BrainLAB AG (Feldkirchen, Germany) that uses MRI data of brain tissue characteristics to determine cannula placement and infusion parameters to predict drug distribution. The catheter position and number can be adjusted with the subsequent Vd visualised in three dimensions. When such a simulation was compared with a radio-labelled tracer (^{123}I-labelled albumin) in patients with recurrent gliomas, the mean concordance of the Vd was 65.75% and the mean maximal inplane deviation was less than 8.5mm[148]. The software demonstrated a high sensitivity (71.4%) and specificity (100%) for identifying catheter trajectories that failed to deliver drug into the desired anatomical region.

Most commonly, surrogate imaging tracers are used for real-time imaging of CED[149]. These are infused concurrently with therapeutic agents and are detected by either CT or MR imaging. Tracers detectable by CT include iopamidol and iopanoic acid labelled albumin. However, small molecule, gadolinium based MR-surrogate imaging tracers are commercially available and therefore more widely used[143,150–153]. These have been shown to be safe whilst providing high resolution imaging and a high degree of tracking accuracy when infused with both small and large molecules[144,154,155]. Given the variability in the size of proposed agents utilised for CED, changing the concentration of gadolinium based tracer has been shown to improve accuracy with a 1mM concentration used for when nanometre sized molecules are co-infused and 5mM used when tracing molecules between 400 Da and 70,000 Da[154,156–158].

Several limitations of these tracers exist given that they are a surrogate measure of drug distribution and are not conjugated to the therapeutic agent being infused. Small molecule tracers are less accurate when utilised as part of large volume infusions due to a faster rate of diffusion at the leading edge of the infusion. This therefore requires a higher rate of infusion to compensate. Similarly, tracers may have very different rates of efflux, binding and degradation compared to the therapeutic agent they are co-administered with[145,159]. Given these limitations, conjugation of a radionucleotide tracer ([124]Iodine) to a therapeutic compound (antiglioma monoclonal antibody 8H9) has been demonstrated by Luther *et al*. with the tracer enabling detection by positron-emission tomography/CT (PET/CT)[160]. Such theragnostic compounds are likely to become increasingly popular in CED.

CED is a promising choice for drug delivery in DIPG given that the tumour is most commonly localised to the pons at diagnosis, grows focally along white matter tracts and is not amenable to surgical resection. Early studies demonstrated the safety and feasibility of CED for DIPG but were conducted outside of clinical trials[132,161]. Several clinical trials using CED in DIPG are currently ongoing. Souweidane at al. published their results of a single centre phase 1 dose escalation trial in which a radiolabelled antibody [124]I-8H9 was administered to 25 patients. No dose limiting toxicities were identified and drug delivery was well tolerated. Median overall survival appeared to correlate appropriately with dose escalation but cohorts were small and therefore it is difficult to make meaningful conclusions. Ultimately, the trial was the first of its kind and demonstrated the safety and feasibility of delivering CED into the brainstem using a theragnostic compound that enabled visualisation of the Vd [162].

Additional ongoing CED trials in DIPG include that of a nanoparticle formulation of the drug Panobinostat (NCT03566199) and a nanoliposomal formulation of irinotecan with gadolinium (NCT03086616). There are however, several limitations of CED as a drug delivery method in DIPG. The surgery required for catheter placement poses significant risk to patients when we consider that biopsy is still not routinely performed for DIPG patients across the globe due to the potential morbidity and mortality. In addition, given that tumours change with time – either developing oedema or areas of necrosis, particularly following radiation therapy, CED is most suited as a delivery modality in the early stages of the disease course[163]. This is further supported by the fact that in its later stages, DIPG has been shown to spread beyond the pons along perivascular and leptomeningeal pathways throughout the brain[164,165]. As such, CED would need to provide significant early disease control in order to prevent disease dissemination.

1.3.4 BBB disruption

BBB disruption has classically been attempted with the infusion of a hyperosmotic agent such as mannitol resulting in non-selective BBB opening achieved by shrinking of the endothelium and transient opening of tight junctions. The key limitation of this approach has been the unwanted exposure of healthy brain tissue to both the co-administered cytotoxic therapies as well as circulating hydrophilic solutes from which the brain is normally protected[166].

Subsequently, the peripheral vasodilator bradykinin was postulated as an agent capable of increasing BBB permeability but with the advantage of demonstrating selectivity for tumour vasculature when used at lower concentrations[167,168]. This selectivity is attributed to higher concentrations of nitric oxide synthase (NOS) in tumour

vessels with NOS being the downstream effector of bradykinin binding to B_2 receptors and cytosolic calcium release[169]. However, pre-clinical studies demonstrated a variability in the degree of blood-tumour barrier disruption which was attributed to variations in the vasculature between different tumour models[168]. When a comparison between bradykinin and mannitol mediated delivery of radiolabelled tracers was made in a pre-clinical model of lung metastases to the brain, bradykinin conferred minimal change in delivery to both the tumour and surrounding brain[170].

The bradykinin analogue Lobradimil was co-administered with carboplatin as part of a phase II trial for paediatric patients with CNS tumours including DIPG and high grade gliomas[171]. Despite efforts to use a twofold higher dose of lobradimil, no objective responses were seen in patients with gliomas. It is however difficult to say in this instance whether the limitation in this study was that of the efficacy of BBB disruption or that of the chosen cytotoxic agent.

1.3.5 Magnetic resonance guided focused ultrasound (MRgFUS)

The use of ultrasound to achieve BBB disruption is believed to be a novel technique with the therapeutic potential to achieve reversible and focal BBB opening without tissue injury or adverse effects to the surrounding brain. In its most basic form, ultrasound is a pressure wave generated by a mechanical motion that causes molecules within a medium to oscillate around their rest positions. Due to bonds that exist between molecules, adjacent molecules are affected resulting in transmission of a longitudinal pressure wave through the medium[172]. The presence of a medium is essential for the propagation of the wave and the frequency of the wave is above that which is audible by the human ear.

To generate an ultrasound wave, radiofrequency voltage is applied across a piezoelectric material, referred to as a transducer, which expands and contracts in

proportion to the applied voltage. Transducers work maximally when they are operated close to their resonant frequency i.e when the thickness of the transducer is equal to half of the wavelength. This frequency is termed the fundamental resonant frequency and results in the maximum displacement at the transducer face. Although transducers can be driven at frequencies above their fundamental resonant frequency, the efficiency of conversion is reduced. In order to achieve greater control over the electrical and acoustic properties of a transducer, a piezoelectric material can be placed within a polymer matrix to form a piezo composite transducer. Furthermore, transducers are usually produced with a backing material such as air which has minimal impedance in order to maximize the acoustic energy transmission through the transducer face.

Focused ultrasound, (FUS) refers to the ability to direct and localise the ultrasound field compared to the diffuse hemispherical wave that is generated by a planar, circular transducer. This is achieved by increasing the diameter of the ultrasound source such that it exceeds the wavelength in the medium and then using lenses, reflectors or spherically curved, self-focusing transducers to focus the ultrasound wave. Electrical focusing can also be achieved by using arrays of small transducers with each one driven by a radiofrequency signal with a specific phase and amplitude such that the resultant ultrasound waves of all of the elements are in phase at a specific focal point. These phased arrays are the mainstay of diagnostic and therapeutic ultrasound devices and have enabled ultrasound penetration through the skull[173].

Ultrasound is capable of having several biological effects beyond its utility as an imaging modality. It can be used in a thermal capacity to increase perfusion to a tissue or to achieve ablation[174]. Furthermore, it has been shown to enhance the delivery of therapeutics to skin, soft tissue and tumours[175–178]. The ability of ultrasound to achieve

32

BBB disruption was first noted in the 1950s. Backay *et al.* delivered ultrasound lesions to the cat brain and noted trypan blue staining of the targeted regions when the latter was administered intravenously[179]. They concluded that ultrasound could disrupt the BBB and noted that the intervening brain tissue between the transducer and the target remained intact. A later study by Patrick et al. identified that BBB disruption arises in the periphery of ultrasound mediated brain lesions, where the temperature is lower and the potential of achieving BBB disruption without thermal injury was proposed[180]. However, despite attempts at achieving BBB disruption with ultrasound alone, it was shown to be unreliable such that the avoidance of tissue injury could not be guaranteed.

To overcome this limitation, microbubbles were introduced as an intravenously administered agent used to limit the ultrasound effects on the endothelium. Several effects are seen when microbubbles interact with ultrasound energy. Firstly, the bubbles oscillate and expand in size by means of rectified diffusion. At higher acoustic pressures, the bubbles collapse within themselves – a process known as inertial cavitation. The latter is somewhat uncontrolled in its impact on the surrounding tissue, resulting in high velocity jets and an increase in temperature[181,182]. In addition, the interaction of microbubbles and acoustic energy results in acoustic streaming in the surrounding medium which exerts a shear stress on the endothelium wall[183]. It is now recognised that BBB disruption is best achieved when sonication parameters are optimised to achieve a microbubble state of stable cavitation – in which they expand and contract but do not collapse[184]. It should however be stated that although microbubbles are commercially approved as ultrasound contrast agents, their use in conjunction with focused ultrasound for BBB disruption is currently experimental.

The underlying mechanism that leads to BBB disruption is attributed to microbubble cavitation having a mechanical effect on the endothelium, resulting in widening of tight junctions as well as an unexplained phenomenon of increased active transport via transcellular uptake of caveolae and cytoplasmic vacuolar structures[185]. Furthermore, when BBB disruption was performed in mice with a cranial window in the dorsal skull and the intravenous injection of fluorescent tracers, vasoconstriction of blood vessels was observed during ultrasound pulses which preceded the leakage of tracer[186]. This suggests a conformational change in the vasculature contributing to BBB disruption.

Two significant developments in focused ultrasound technology led to the clinical translation of FUS medicated BBB disruption. Firstly, O'Reilly et al. introduced the concept of a wideband polyvinlidene fluoride hydrophone receptor which enabled the detection of ultraharmonic emissions from microbubbles subjected to ultrasound energy[187]. This real-time feedback enabled the development of an algorithm such that focused ultrasound exposures could be controlled in order to achieve stable cavitation of microbubbles and thereby avoid the unpredictable tissue effects of inertial cavitation. By incrementally increasing ultrasound pressures until ultraharmonic emissions were detected from circulating microbubbles, they found that a 50% scaling of the ultrasound pressure at this level produced consistent and reliable BBB disruption without tissue injury. This provided the potential to account for tissue specific variations in the acoustic power required to achieve safe BBB disruption.

The second major development was that of a hemispherical phased array ultrasound delivery system that enabled ultrasound penetration through the skull in a non-invasive manner[173,188]. The resultant clinical prototype device was established by Insightec, Inc., Haifa, Israel in collaboration with scientists at Brigham and Women's

Hospital. The system comprised an array with over 500 elements and provided, focal, trans-skull penetration of ultrasound energy, accommodating for variations in skull thickness and preventing thermal injury to overlying tissues[189,190].

This prototype has undergone clinical translation with Insightec now offering an MRI compatible, commercially available cranial ultrasound delivery system which is utilised in several international hospitals (www.insightec.com). The device has been FDA approved for thermal ablation of targets within the thalamus, subthlamaus and pallidum for the treatment of Essential Tremor and an idiopathic, tremor dominant variant of Parkinson's disease. Furthermore, several clinical trials are currently underway, assessing the use of the ExAblate Model 4000 type 2 "Neuro-System" for the purposes of BBB disruption in several disease states including high grade glioma (NCT03616860), brain metastases (NCT03714243) and Parkinson's Disease Dementia (NCT03608553).

A unique feature of MRgFUS mediated BBB disruption is its transitory nature lasting between 4-6 hours therefore limiting the potential toxicity of more prolonged BBB opening[191,192]. Preclinical work has demonstrated the ability of MRgFUS to concentrate chemotherapeutics and macromolecules in targeted brain tissue as well as tumours with significant treatment effect[193–196].

1.4 Molecular Therapeutics in DIPG

The currently known molecular alterations in DIPG indicate a disruption of epigenetic regulation which cultivates oncogenesis in concert with more familiar secondary mutations in oncogenic pathways. Following the dearth of meaningful treatment responses to conventional chemotherapeutics, molecularly targeted therapies are being increasingly explored. Several classes of drugs have mechanistic potential in the

treatment of DIPG and three such drug classes include HDAC inhibitors, PARP inhibitors and Tyrosine Kinase inhibitors.

1.4.1 Histone Deacetylase Inhibitors (HDAC)

HDAC inhibitors and more specifically, the drug Panobinostat was identified as a potential drug treatment for DIPG in an *in vitro* drug screen of 83 molecular therapies in 14 patient derived DIPG cell lines[81]. The drug was shown to increase H3 acetylation and partially rescue the H3K27 trimethylation phenotype in a dose dependent manner. Furthermore, marked changes in gene expression were identified with lower expression of pro proliferation genes and a restoration of the K27M gene expression signature. A reduction in cell proliferation and increased cell death conferred a survival benefit in a murine xenograft model of DIPG[81].

Despite these promising findings, Hennika *et al*. reported that despite effective tumour penetration and end target effects, drug toxicity was a significant limiting factor[197]. An initial dose of 20mg/kg once daily was gradually reduced to twice weekly dosing and although this was well tolerated, it did not confer an overall survival benefit. In a second orthotopic xenograft, the group attempted the same treatment regimen as Grasso *et al.* with 10mg/kg intra-peritoneal, (IP) panobinostat administered for 5 days followed by 2 days off and a further 5 days of treatment. This again failed to show a significant survival benefit.

A possible explanation for this is a lack of BBB penetration at systemically tolerated doses. This theory is supported by the findings of Rodgers *et al.* who assessed the pharmacokinetics of Panobinostat in a non-human primate model (NHP)[198]. Using Panobinostat levels in the ventricular CSF as a surrogate marker for CNS drug penetration they reported very limited quantities of the drug detectable in CSF following systemic

administration. They postulated that effects seen in murine models may be due to an impaired BBB in these models and that although the properties of the drug suggest the ability to cross the BBB, the low levels seen in NHP's may be due to drug efflux transporters such as P-glycoprotein. These transporters have been shown to have a significantly reduced expression level in mice as compared to humans[199].

Given these findings, local drug delivery has been attempted with administration of water soluble panobinostat via convection enhanced delivery[200]. No neurotoxicity was shown at clinically relevant drug concentrations in both small and large animal models and there was adequate drug distribution by this method. The study highlighted a short tissue half-life of panobinostat in the brain indicating the likely need for repeated drug administration. The drug therefore still has significant potential in DIPG if either a systemically delivered dose could be reduced or more localised delivery could be achieved.

1.4.2 Poly adenosine diphosphate-ribose polymerase (PARP) inhibitors

Poly(ADP) ribose (PAR) polymerase 1 (PARP-1) is a nuclear enzyme which functions as a sensor of cellular DNA damage[201]. The enzyme uses NAD^+ to add mono-ADP-ribose or PAR to itself and other acceptor proteins in a process termed PARylation which is the first response to DNA damage. This facilitates the recruitment of DNA repair proteins to sites of DNA damage whether that be single stranded or double stranded DNA break[202]. A further role in DNA repair is that of modulating the structure of chromatin such that it facilitates DNA repair[203]

PARP-1 also has a role in DNA replication where it recognises unligated Okazaki fragments[204]. Due to its instrumental role in DNA repair and replication, PARP-1 has become a target for cancer therapy being used to treat cancers with known DNA repair defects and for combination therapy with DNA damaging agents or radiation therapy[205].

There are currently four PARP inhibitors approved for clinical use by the Food and Drug Administration (FDA); olaparib, rucaparib, niraparib and talazoparib.

Pre-clinical investigation of the use of PARP inhibitors for DIPG has been conducted and demonstrated *in vitro* efficacy in DIPG cell lines as well as an *in vivo* survival benefit when combined with radiation therapy in a paediatric high grade glioma mouse model[206]. A subsequent phase I/II trial however failed to demonstrate a survival benefit of veliparib with radiation and temozolamide but rather importantly highlighted that this may be due to limited BBB penetration[207]. The peripheral action of PARPi was recorded in this study by assessment of peripheral blood monocytes but this is a measure of peripheral drug action and not specifically of CNS action. Measuring central drug action and delivery is a particular challenge in phase I/II trials conducted for brain tumour treatments.

PARP inhibitor therapy remains an exciting prospect for DIPG where it would likely be part of a combination therapy regimen to overcome documented treatment resistance[207] and could be facilitated by a BBB disrupting therapy.

1.4.3 Tyrosine Kinase inhibitors (TKi)

Mutations in PDGFRA are commonly found in DIPG and ultimately lead to ligand independent activation. In combination with focal PDGFRA amplifications, a drive in receptor tyrosine kinase signalling occurs and consequently activates the PI3K and MAPK pathways[51,56]. This is believed to be an early event in DIPG tumorigenesis and is strongly associated with H3.3K27M mutations[38,60]. In addition, focal amplifications also exist in other receptor tyrosine kinases such as KIT/KDR/MET/EGFR, cycling dependent kinase 6 (CDK6) and the regulators of transcription, MYCN and ID2[51].

More recently, the H3K27M mutation has been shown to directly activate effectors within the RAS signalling pathway thereby promoting tumour growth[208]. Furthermore, inhibiting a key effector in the signalling pathway, Extracellular signal-regulated kinase 5, (ERK5) resulted in prolonged survival in a murine model.

A clinical trial is currently ongoing which seeks to assess the potential of several tyrosine kinase inhibitors including dasatinib, crizotinib, erlotinib and everolimus in patients with DIPG (NCT02233049).

Given the redundancy in these oncogenic pathways, it is unclear whether such inhibitors will prove to be efficacious and it may be that these drugs are more effective as part of combination therapy regimes to assist in slowing tumour growth.

1.5 Combination drug therapy and drug synergy

Given the breadth of the epigenetic dysregulation and the known redundancy in oncogenic pathways, to achieve meaningful treatment outcomes in DIPG will likely require multi-drug therapy. Indeed, this is widely recognised across multiple complex diseases[209–211]

There are multiple benefits to such a therapeutic approach; enhanced efficacy, overcoming drug resistance[212] and rather importantly, the potential for drug synergy[213]. The latter refers to a treatment effect that exceeds the expected or additive effect of two or more drugs. This not only confers potency but also the potential to reduce drug doses and their associated side effects[214]. Much emphasis has been placed on high throughput drug screening in recent years and several reference models now exist to quantify drug synergy[215–218]. To facilitate the ease of implementation of these models, an online platform called SynergyFinder has been developed to enable data processing, analysis and

visualisation[219] . The application enables a comparison of synergy models and has most recently been updated to enable analysis of higher order drug combination therapies[220].

Determining a synergistic drug combination therapy could have significant utility in the treatment of DIPG particularly if combined with MRgFUS mediated delivery.

1.6 Aims and Objectives

Despite significant progress in our understanding of the underlying molecular events giving rise to DIPG, the blood brain barrier remains a potent obstacle for the effective delivery of targeted therapies. Low frequency focused ultrasound is a mode of drug delivery that has undergone clinical translation, being used for investigative purposes in supratentorial diseases arising in the brain. Rather importantly, MRgFUS has significant potential benefits over existing drug delivery methods being non-invasive, conferring transient BBB disruption and the possibility of repeated treatment delivery. However, the ability to disrupt the BBB in the brainstem had not previously been demonstrated and the feasibility and safety of doing so in this eloquent brain region was unknown. As such the objectives of my study were as follows:

1) To assess the feasibility of MRgFUS to achieve BBB disruption in the murine brainstem by demonstrating the uptake of gadolinium contrast enhancement radiologically and Evans Blue staining histologically in MRgFUS treated murine brainstems. Furthermore, using a multi-pronged approach to assess safety by recording key functions of the brainstem following BBB disruption and histological analysis of tissues treated with MRgFUS. In addition, I wished to determine if MRgFUS resulted in a quantifiable difference in brainstem drug delivery of a systemically delivered chemotherapeutic agent at the time of BBB disruption using liquid chromatography-mass spectroscopy (LC-MS).

2) To recapitulate a murine model of DIPG that reflects not only the key molecular changes observed in DIPG but also has preserved integrity of the BBB therefore providing a pre-clinical testing model for MRgFUS mediated brainstem drug delivery. More specifically, two models would be produced and compared; the RCAS-Tva genetically engineered mouse model and the SU-DIPG 17 xenograft model. Radiological gadolinium uptake and histological Evans Blue staining would be used to assess BBB integrity.

3) To conduct a high throughput drug screen of new molecular therapies and conventional chemotherapeutics and use the SynergyFinder web application to identify a highly synergistic drug combination therapy for potential delivery via MRgFUS.

2 Safety and feasibility of brainstem MRgFUS BBB disruption

2.1 Results

2.1.1 MRgFUS parameters for BBB disruption

The average peak pressure amplitude reached across all sonications performed in rats was estimated to be 1.1 +/- 0.3 MPa and in mice was 0.71 +/- 0.15 MPa. The *in situ* pressures were estimated assuming a 55% transmission through the skull bone[221] and attenuation of 5 Np/m/MHz through 5 mm of brain tissue[222]. The assumed transmission of 55% through the skull bone at this frequency may result in an over-estimation of the true *in situ* pressures as this figure was obtained from measurements recorded through a more rostral portion of rat parietal bone[221]. The more posterior trajectory of ultrasound in our study, through a caudal portion of the skull with both an increased degree of curvature and thickness, would be expected to result in a higher insertion loss.

2.1.2 Confirmation of brainstem BBB opening

Sprague Dawley rats

Two methods were used to confirm BBB disruption in the brainstem, namely focal gadolinium (Gad) enhancement on post procedure T1-weighted MR imaging **(Fig. 2.1)** and Evans Blue staining of gross histological specimens **(Fig. 2.2).** Immediately following sonication, only rats which received concurrent intravenous injection of µBs ("MRgFUS + µB" and "MRgFUS + µB + Cis") clearly showed localised Gad enhancement in the brainstem, indicating BBB disruption.
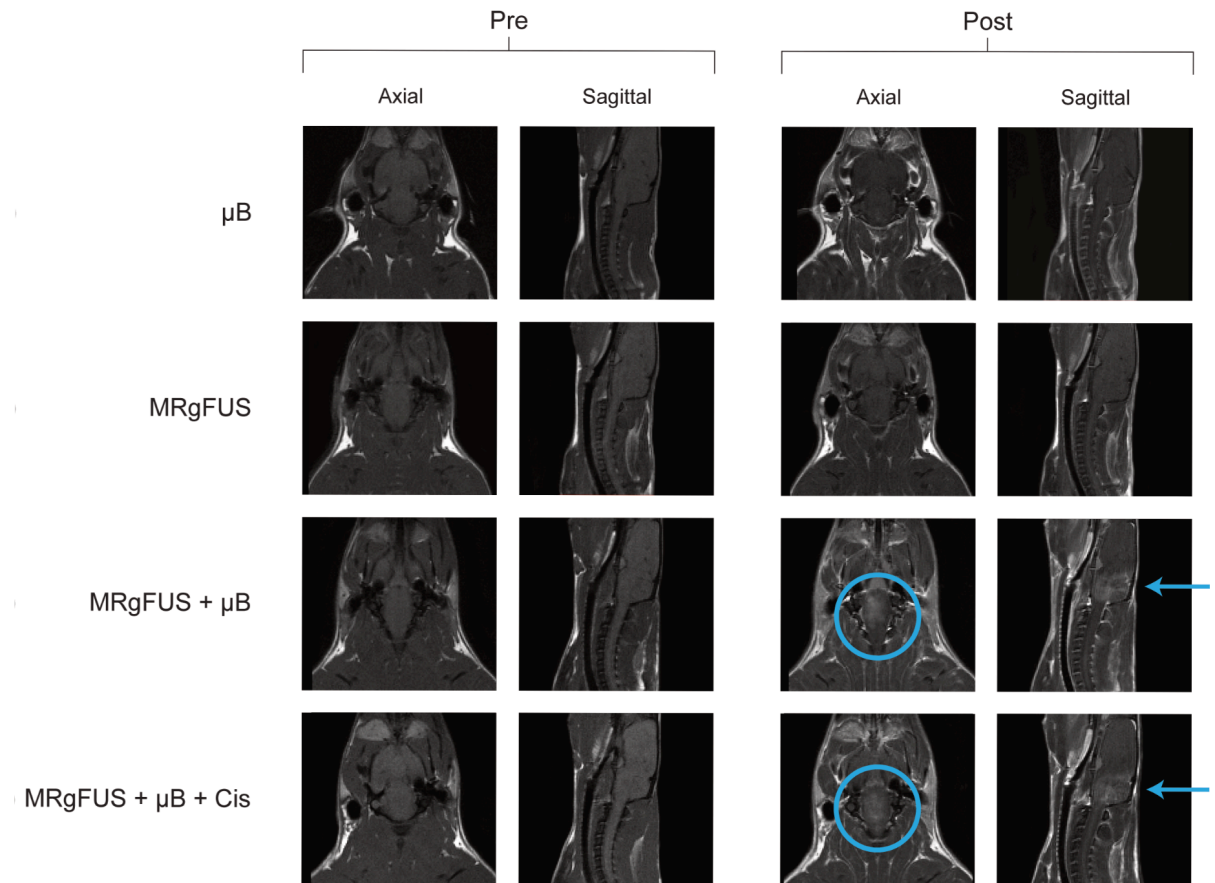
Figure 2.1: Contrast enhanced T1-weighted MR Imaging of BBB opening in rats. Axial and sagittal vies of MR imaging performed pre- and post-MRgFUS delivery to the rodent brainstem. Rats who were treated with microbubbles only (μB) or MRgFUS only did not demonstrate contrast enhancement within the brainstem on post procedure imaging. Animals that received MRgFUS and microbubbles (MRgFUS + μB) did show brainstem enhancement, thereby confirming BBB opening (circles and arrows). The administration of the chemotherapy agent cisplatin (1.5mg/kg) in addition to the focused ultrasound and microbubbles (MRgFUS + μB + Cis) did not affect the ability to achieve BBB opening and contrast enhancement within the brainstem was still seen (circles and arrows).

To further confirm these MRI observations, intravenous Evans Blue was delivered following sonication to demonstrate the extent of BBB disruption histologically. Blue staining was observed on the ventral surface of the brainstem, in and around the region of the pons **(Fig. 2.2 - G)**. On sectioning through the brainstem at the level of the pons, blue staining of both the brainstem and a portion of the ventral cerebellum was evident **(Fig. 2.2 - H)**. This corresponded with the area of focused ultrasound targeted BBB

disruption and contrast enhancement on MR imaging. The presence of dye in the brainstem was again only seen in the "MRgFUS + µB" group (the "MRgFUS + µB + Cis" group was not tested) and not in either the "MRgFUS" , "µB" or "control" groups **(Fig. 2.2 - A-F)**.

Hence the delivery of MRgFUS to the rodent brainstem at the time of IV µB administration results in BBB disruption at the targeted brainstem site and this has been confirmed by both the presence of gadolinium contrast extravasation and Evans blue staining of the area.

Anterior   **Cross section**
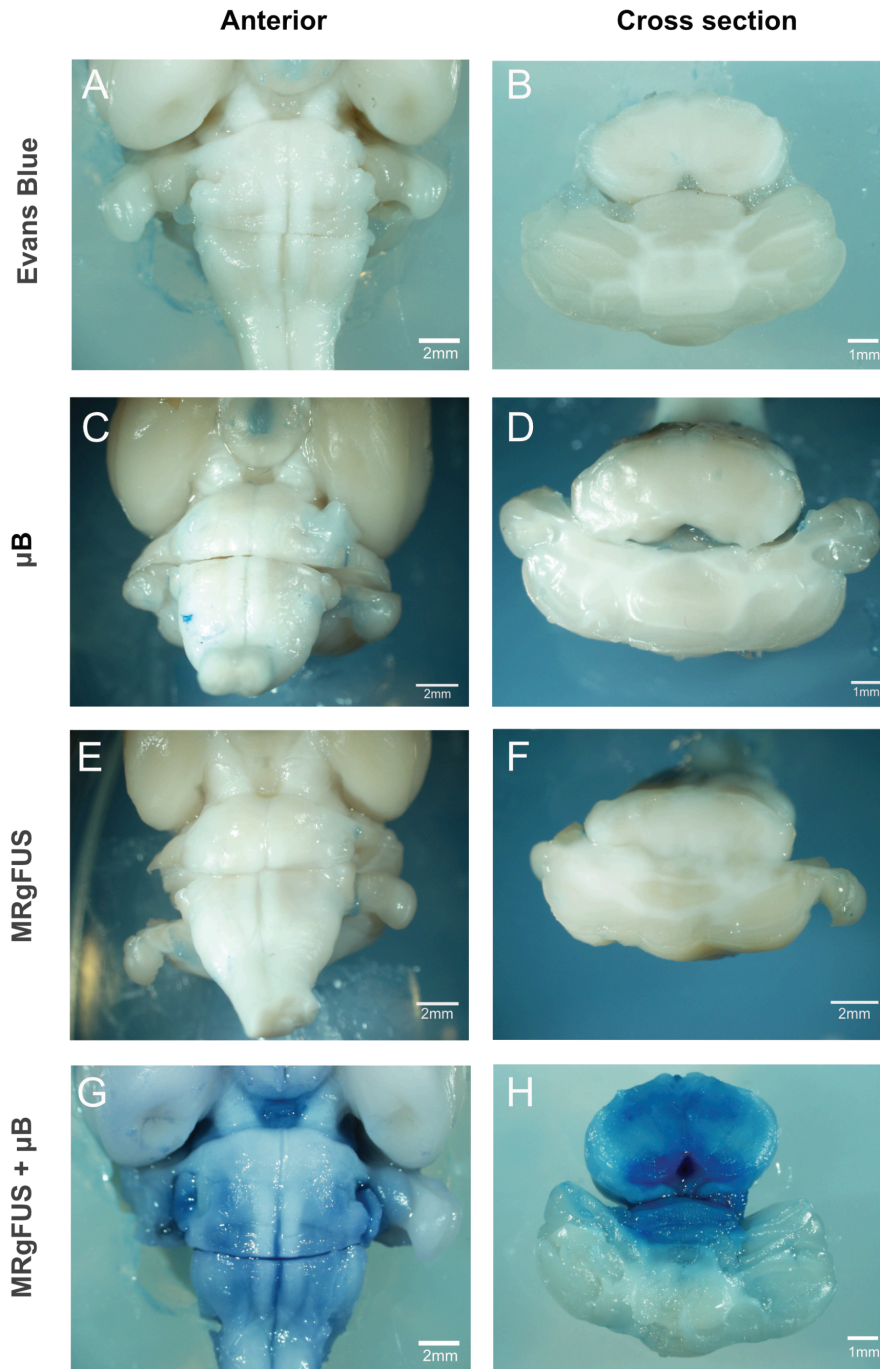
Figure 2.2: Evans Blue staining of rodent brainstem confirming BBB opening. Rats were treated with either microbubbles only (µB), MRgFUS or both (MRgFUS + µB). Control "Evans Blue" rats received no intervention. Following treatment, 4% Evans Blue was administered immediately after. Animals were then perfused (4% PFA) and brainstem specimens were extracted, sectioned and imaged. Blue staining was observed on the anterior aspect of the brainstem and on cross section of animals in the (MRgFUS + µB) group only, thereby confirming BBB permeability in the region. This was not true for the "µ B", "MRgFUS" and "Evans Blue" treated animals.

NSG Mice

Focal gadolinium enhancement on post-procedure T1 weighted imaging was used to confirm BBB disruption in NSG mice administered doxorubicin **(Fig 2.3).** As above, only mice in the "MRgFUS + μB" cohort demonstrated brainstem gadolinium enhancement indicating successful BBB permeability in the region.
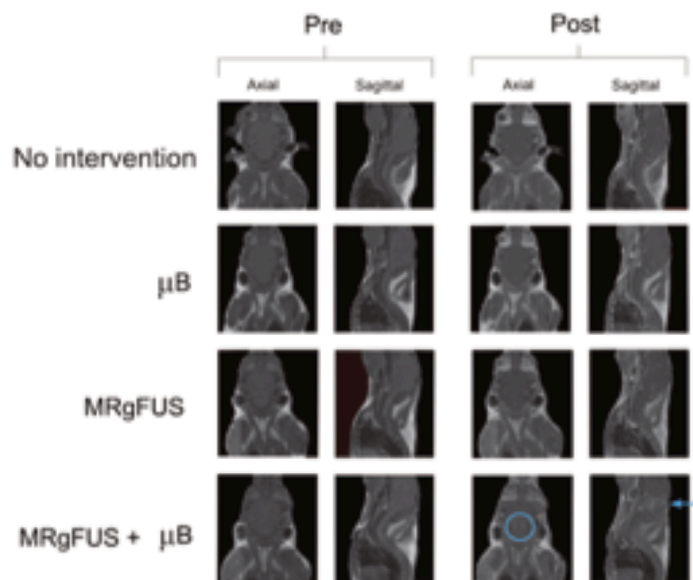
Figure 2.3: Contrast enhanced T1-weighted MR imaging of BBB opening in mice. Axial and sagittal views of MR imaging performed pre- and post-FUS delivery to the murine brainstem. Mice who received "no intervention" or were treated with microbubbles only (μB) or MRgFUS only (MRgFUS) did not demonstrate contrast enhancement within the brainstem on post procedure imaging. Animals that received MRgFUS and microbubbles (MRgFUS + μB) did show brainstem enhancement, thereby confirming BBB opening (circle and arrow).

2.1.3 Physiological parameters are preserved during MRgFUS brainstem BBB disruption

Grey matter nuclei contained within the brainstem include the cardiovascular and medullary rhythmicity centres which together control the heart rate, blood pressure and respiratory rate. As such, tissue injury to this region has the potential to affect these vital functions. Once under anaesthesia, rats were recorded for 4 minutes to determine baseline vital signs and ensure stable signal detection. Monitoring was continued throughout MRgFUS of each half of the brainstem and for a further 4 minutes after. The

normal heart rate in rats varies from 250 - 450 beats per minute with a respiratory rate up to 85 beats per minute. Although variability and fluctuations are seen in both parameters, these were not concurrent with periods of focused ultrasound delivery (**Fig. 2.4** - pink bars) but rather occurred consistently throughout the period of monitoring.
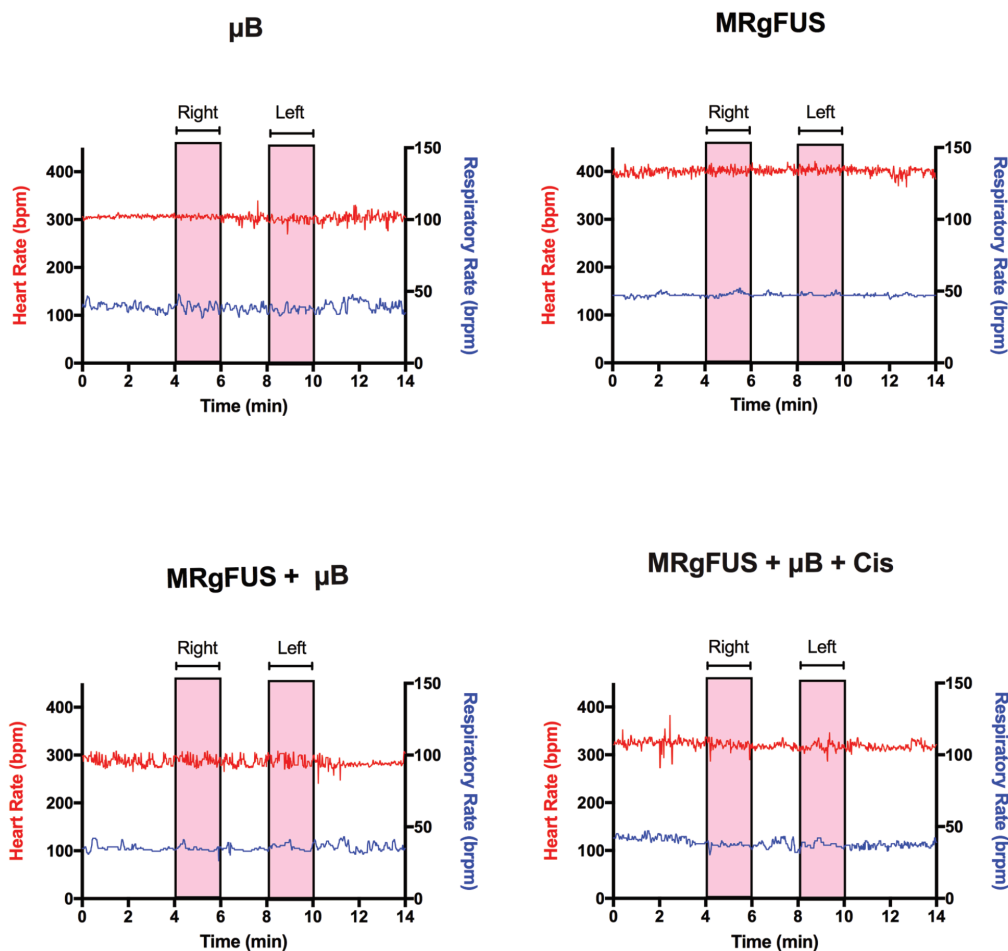
Figure 2.4: Physiological monitoring of heart and respiratory rate. The MouseOx rodent monitoring system was used to monitor the heart rate (in red) and respiratory rate (in blue) of rats (n = 9 per group) during focused ultrasound delivery to the brainstem. Rats were randomised to one of four treatment groups; microbubbles only (µB), focused ultrasound only (MRgFUS), focused ultrasound and microbubbles (MRgFUS + µB) with a final group consisting of the latter in conjunction with intravenous Cisplatin delivery (MRgFUS + µB + Cis).

Statistical comparison was made of the mean heart rate (**Fig. 2.5 - A**) and respiratory rate (**Fig. 2.5 - B**) during and after MRgFUS delivery to that of baseline before intervention recordings and no significant difference was found. Both parameters remained stable

throughout the monitoring period with no persistent fluctuations from baseline or abrupt cessation of parameters. This was true for all animals across the different treatment groups **(Fig. 2.4 & 2.5)** and indicates that MRgFUS and/or µB delivery does not cause tissue injury resulting in impaired autonomic cardiorespiratory function.
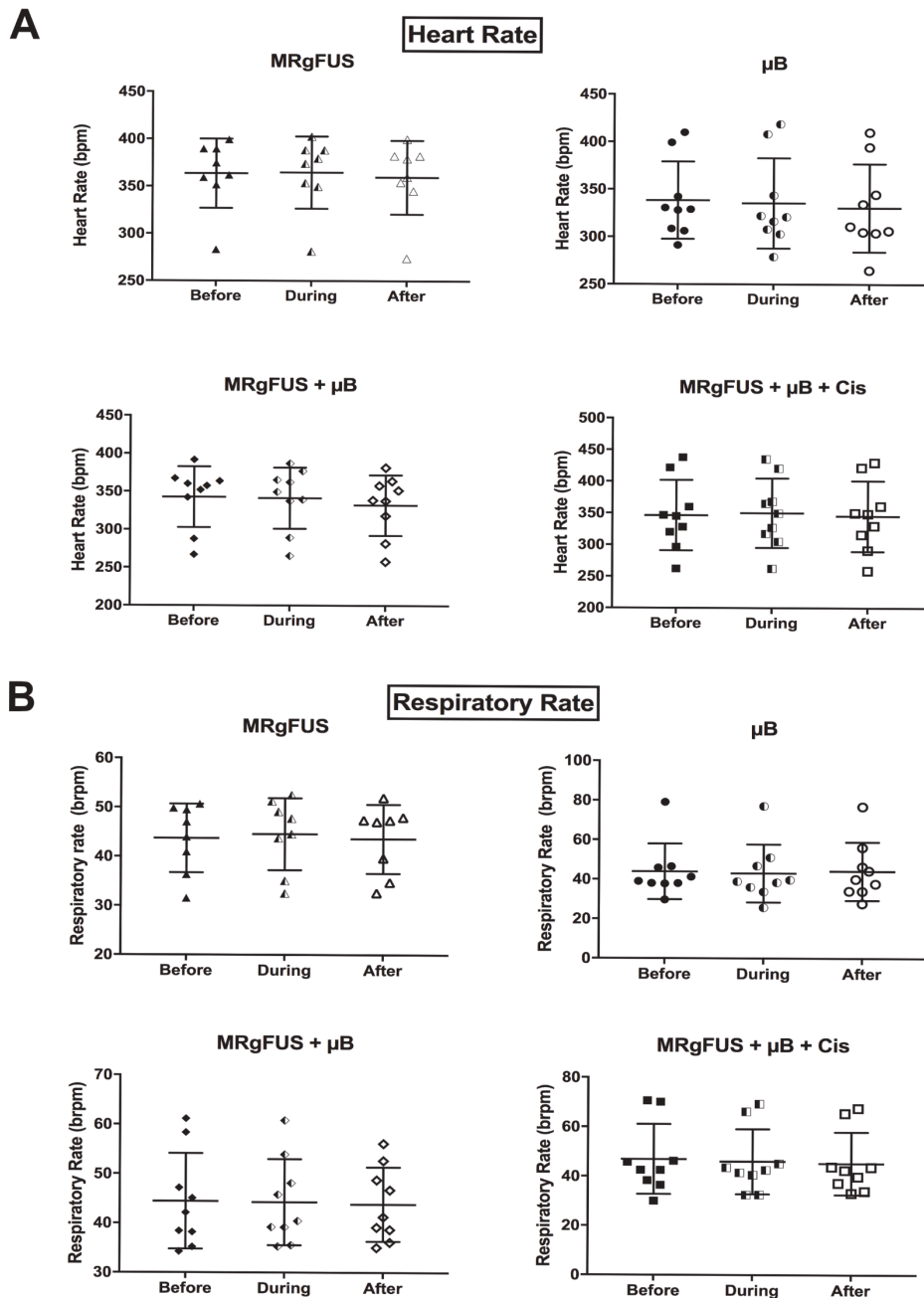
Figure 2.5: Comparison of mean heart rate and respiratory rate recordings of rats before, during and after the specified procedures. The MouseOx rodent monitoring system was used to monitor the heart rate and respiratory rate of rats during focused ultrasound delivery to the brainstem. Rats were randomised to one of four treatment groups; **A)** microbubbles only (µB), **B)** focused ultrasound only

(MRgFUS), **C)** focused ultrasound and microbubbles (MRgFUS + µB) with a final group consisting of the latter in conjunction with intravenous Cisplatin delivery (MRgFUS + µB + Cis) **(D)**. Monitoring was initiated four minutes "before" the sonication (filled shapes) continued "during" sonication (half-filled shapes) and continued for four minutes "after" completion of the sonication (empty shapes). The mean recording for each rat within each treatment group is plotted. The mean and standard deviation of each group is represented by horizontal lines. No statistically significant difference in heart and respiratory rate were noted "during" and "after" any of the interventions when compared to baseline "before" recordings (Two way multivariate mixed model ANOVA, $p > 0.05$).

2.1.4 Motor control and coordination are intact following brainstem BBB disruption

Motor neurons and axonal projections that enable movement and coordination also traverse the brainstem and therefore, rotarod performance and grip strength testing were selected as additional surrogate measures to indicate the functional integrity of the brainstem. Both rotarod and grip strength data were compared pre- and post-MRgFUS delivery to the rat brainstem **(Fig. 2.6).** Comparison of post procedure performance with pre-procedure untreated performance provided an internal negative control. No statistically significant differences were identified in rotarod performance when comparing performance between groups. However, animals within each group demonstrated improved performance on post-procedure testing which may be attributed to the expected improvement in performance by animals with repeated measurements. **(Fig. 2.6 - A).** These findings were also found in grip strength testing **(Fig. 2.6 - B).**

These findings demonstrate that there was no functional impairment in the brainstem motor tracts as a result of MRgFUS mediated BBB disruption in the rodent brainstem.

A **Rotarod**
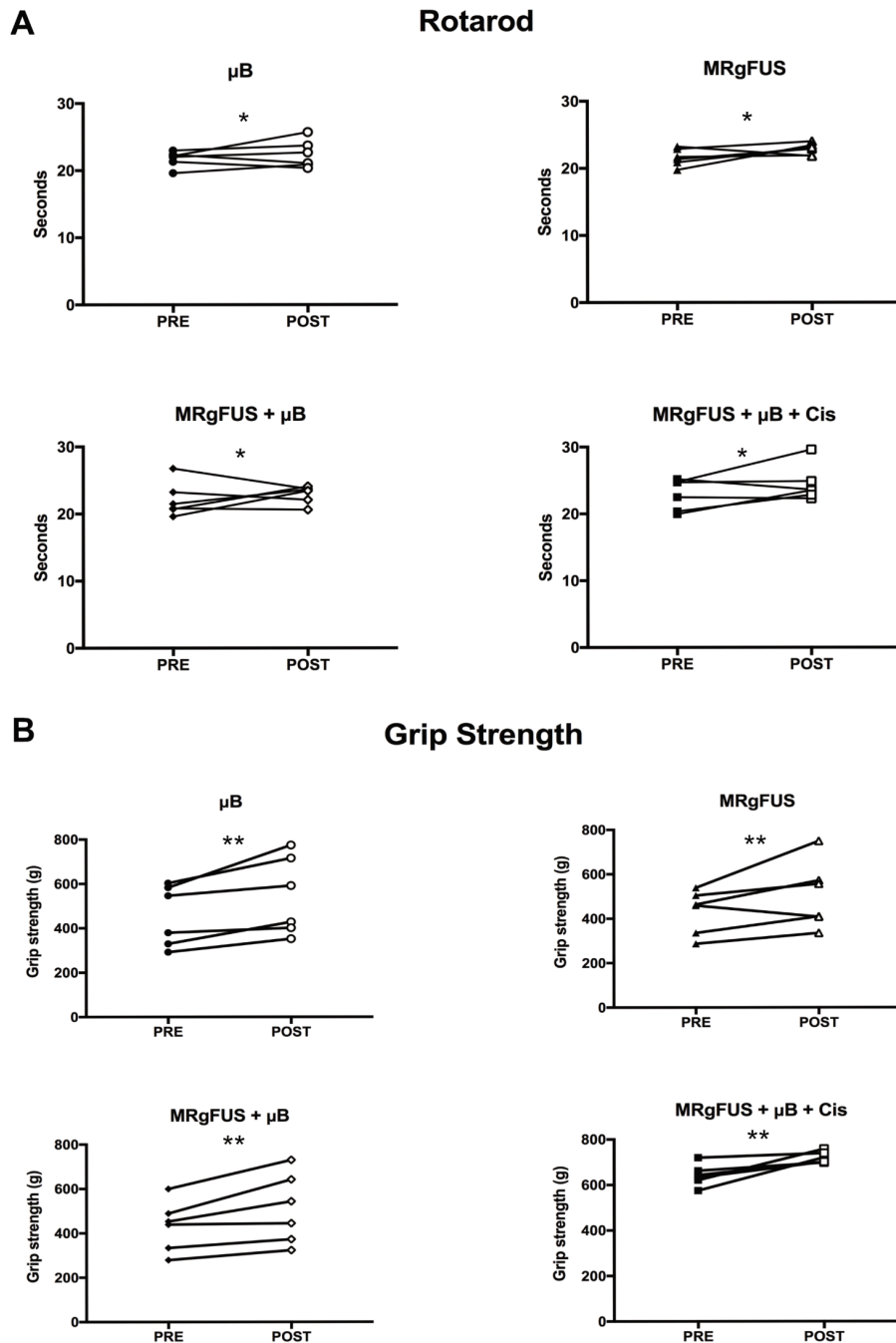
B **Grip Strength**

Figure 2.6: Comparison of rotarod and grip strength performance pre-and post-procedure. Rats were tested one week pre (filled shapes) and one week post (empty shapes) intervention with either microbubbles alone (µB), focused ultrasound alone (MRgFUS), focused ultrasound and microbubbles (MRgFUS + µB) or focused ultrasound with microbubbles and cisplatin (MRgFUS + µB + Cis). No difference in rotarod performance **(A)** or grip strength **(B)** was identified when comparing treatment groups (2 way mixed MANOVA with Tukey's post hoc test, * $p < 0.05$ for rotarod, ** $p < 0.001$ for grip strength). A significant improvement in performance was noted in both rotarod and grip strength pre- and post-procedure.

2.1.5 Brainstem tissue is preserved following MRgFUS brainstem BBB disruption

Three levels of the rodent brainstem were assessed **(Fig. 2.7 - A)**. Sections were stained with H&E for cell morphology, Caspase-3 for apoptosis and NeuN for neuronal number. These parameters were chosen as focused ultrasound could potentially cause tissue damage in the form of haemorrhage and tissue vacuolation, increased apoptosis and neuronal loss[187,223]. At both early (4 hours) and late (14 day) time points, H&E stained sections did not show evidence of tissue damage or haemorrhage in any of our groups when compared with untreated controls **(Fig. 2.7 - B)**. This was independently verified by a veterinary pathologist who was blinded to the sample groupings.
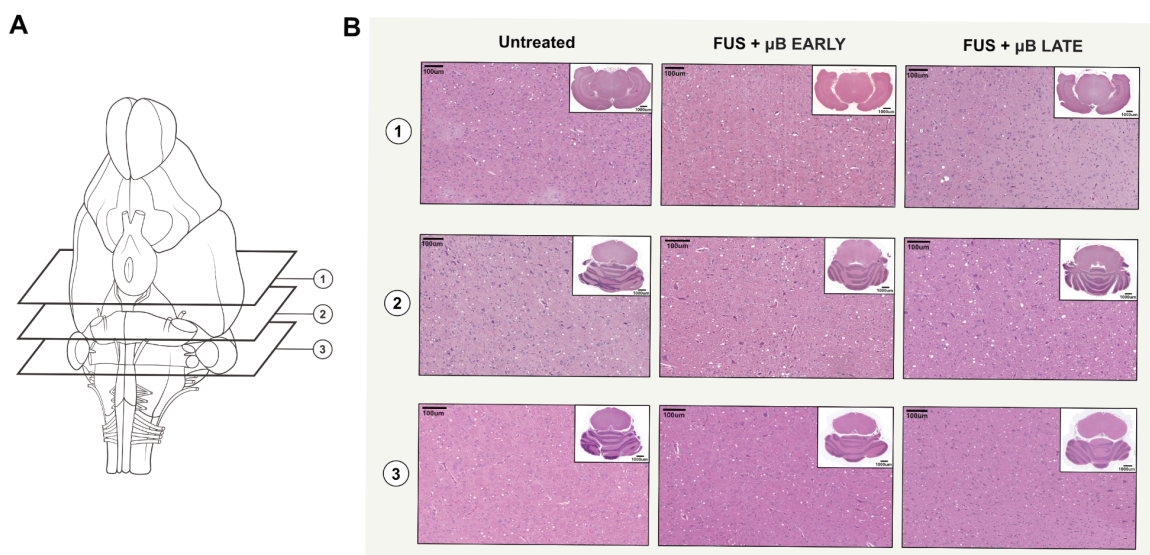
Figure 2.7: Hematoxylin and eosin (H&E) staining of brainstem sections. Following focused ultrasound delivery, brainstem samples were retrieved at early (4 hours) and late (14 days) post intervention. **(A)** Schematic demonstrating that three regions of the brainstem were sectioned and analysed. **(B)** Treated samples ("MRgFUS + µB") were compared to "untreated" controls. No evidence of tissue damage in the form of haemorrhage or vacuolation was seen at either the early or late time points.

In addition, we did not note any significant differences in positive caspase 3 staining for any groups compared to untreated controls **(Fig. 2.8 & 2.9)**. Similarly, there were no

changes in neuronal number between groups, at all levels of the brainstem **(Fig. 2.10 and**

2.11).

Hence MRgFUS mediated BBB disruption in the brainstem did not result in increased apoptotic activity or injury resulting in neuronal loss.
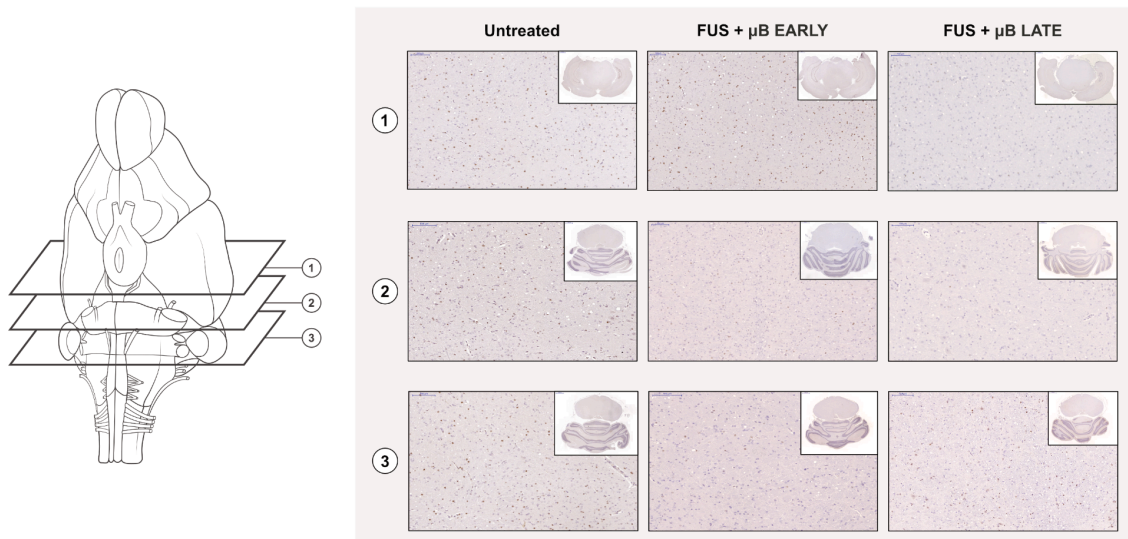
Figure 2.8: Caspase 3 stained sections at early and late time points. Following treatment with focused ultrasound and intravenously administered microbubbles, rodents were perfused and brainstems retrieved at 4-hour **(MRgFUS + µB EARLY)** and 14 day (**MRgFUS + µB LATE)** time points. Brainstems were sectioned at three levels and stained for Caspase 3 activity as a marker of apoptosis. Sections were compared to Caspase 3 stained sections of untreated controls **(Untreated).** No difference in the degree of Caspase 3 staining was noted. A high grade renal tumour was used as a positive control (data not shown).
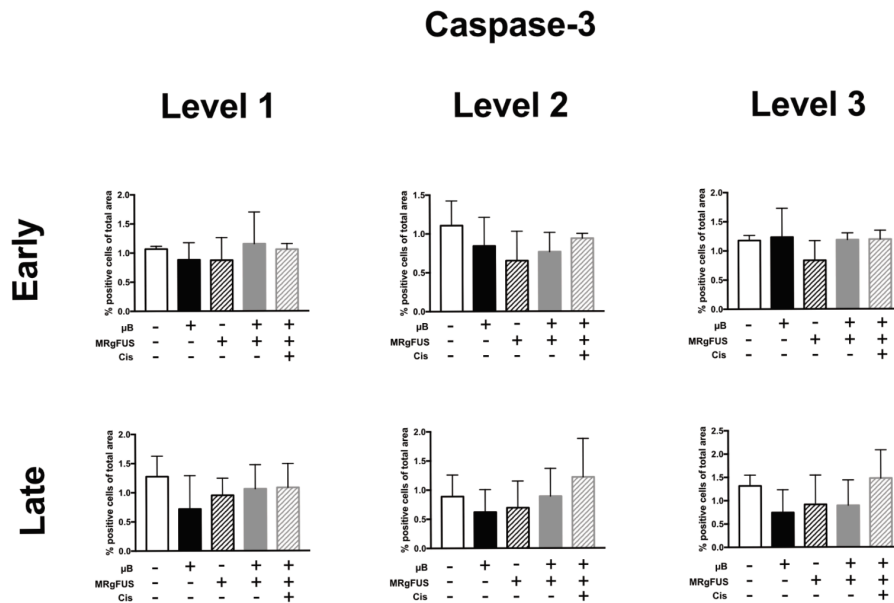
Figure 2.9: Quantification of Caspase 3 staining of brainstem samples. Histological analysis of brainstem samples was conducted at early (4 hours) and late (14 day) time points. Three levels of the brainstem were assessed for Caspase 3 staining as a marker of apoptosis. No significant difference in the percentage area of caspase 3 staining was identified across all groups at either time point (Three-way MANOVA with Tukey's post hoc test).
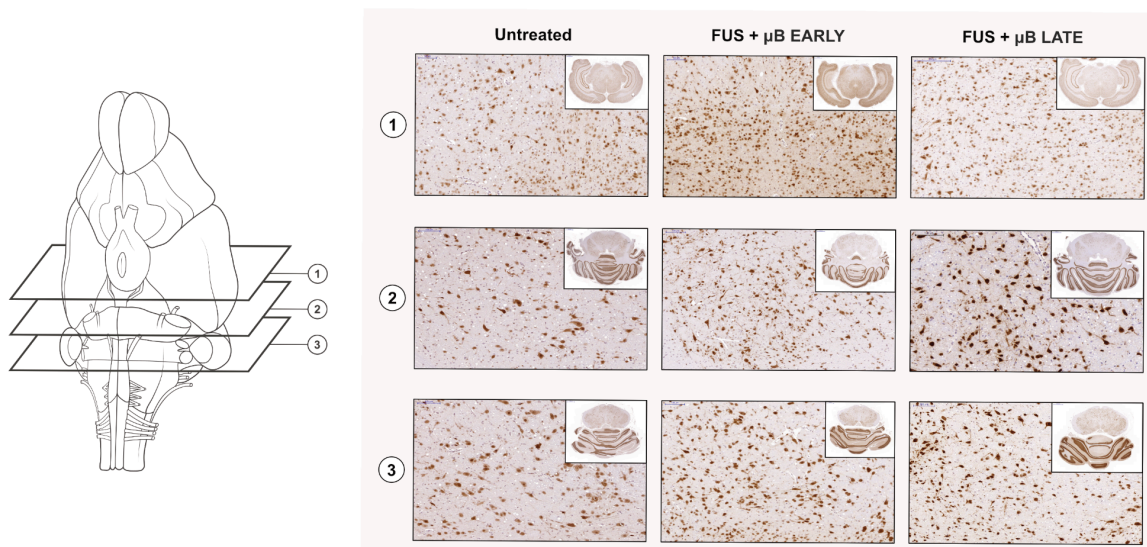
Figure 2.10: NeuN stained sections at early and late time points. Following treatment with focused ultrasound and intravenously administered microbubbles, rodents were perfused and brainstems retrieved at 4-hour **(MRgFUS + µB EARLY)** and 14 day **(MRgFUS + µB LATE)** time points. Brainstems were sectioned at three levels and stained for NeuN to quantify neuronal number. Sections were compared to Caspase 3 stained sections of untreated controls **(Untreated).** No difference in the number or morphology of neurons was identified.
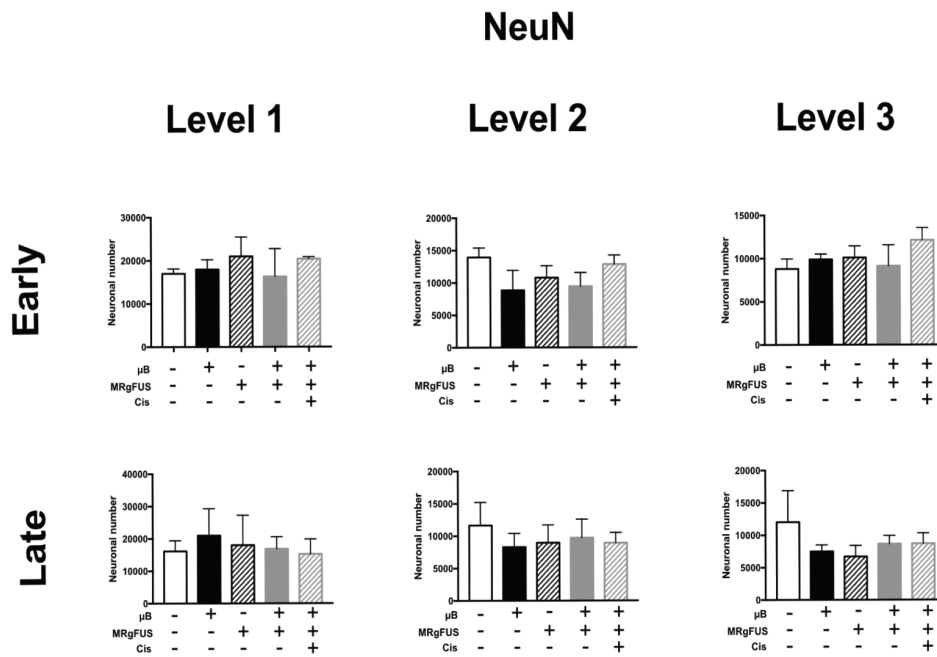
Figure 2.11: Quantification of NeuN staining of brainstem samples. Histological analysis of brainstem samples was conducted at early (4 hours) and late (14 day) time points. Three levels of the brainstem were assessed for NeuN staining of neuronal nuclei for quantification. No significant difference in the percentage area of caspase 3 staining or neuronal number was identified across all groups at either time point (Three-way MANOVA with Tukey's post hoc test).

2.1.6 Doxorubicin demonstrates *in vitro* efficacy in DIPG

An initial screen of eight conventionally used chemotherapy agents in three patient-derived DIPG cell lines was performed **(Fig. 2.12 – A)** Three agents; Etoposide, Doxorubicin and Mitoxantrone demonstrated significant toxicity across all three cell lines with correspondingly low IC_{50} values (mean values of 421nM, 49nM and 50nM respectively) **(Fig. 2.12 - B).** Carboplatin, BCNU and Melphalan also demonstrated toxicity, but were less effective, requiring higher drug concentrations. In contrast, both Temozolamide and Cisplatin demonstrated little to no toxicity in these cell lines. Twelve-point dose escalation curves for Doxorubicin and Temozolamide can be seen in (**Fig. 2.12 – C).**
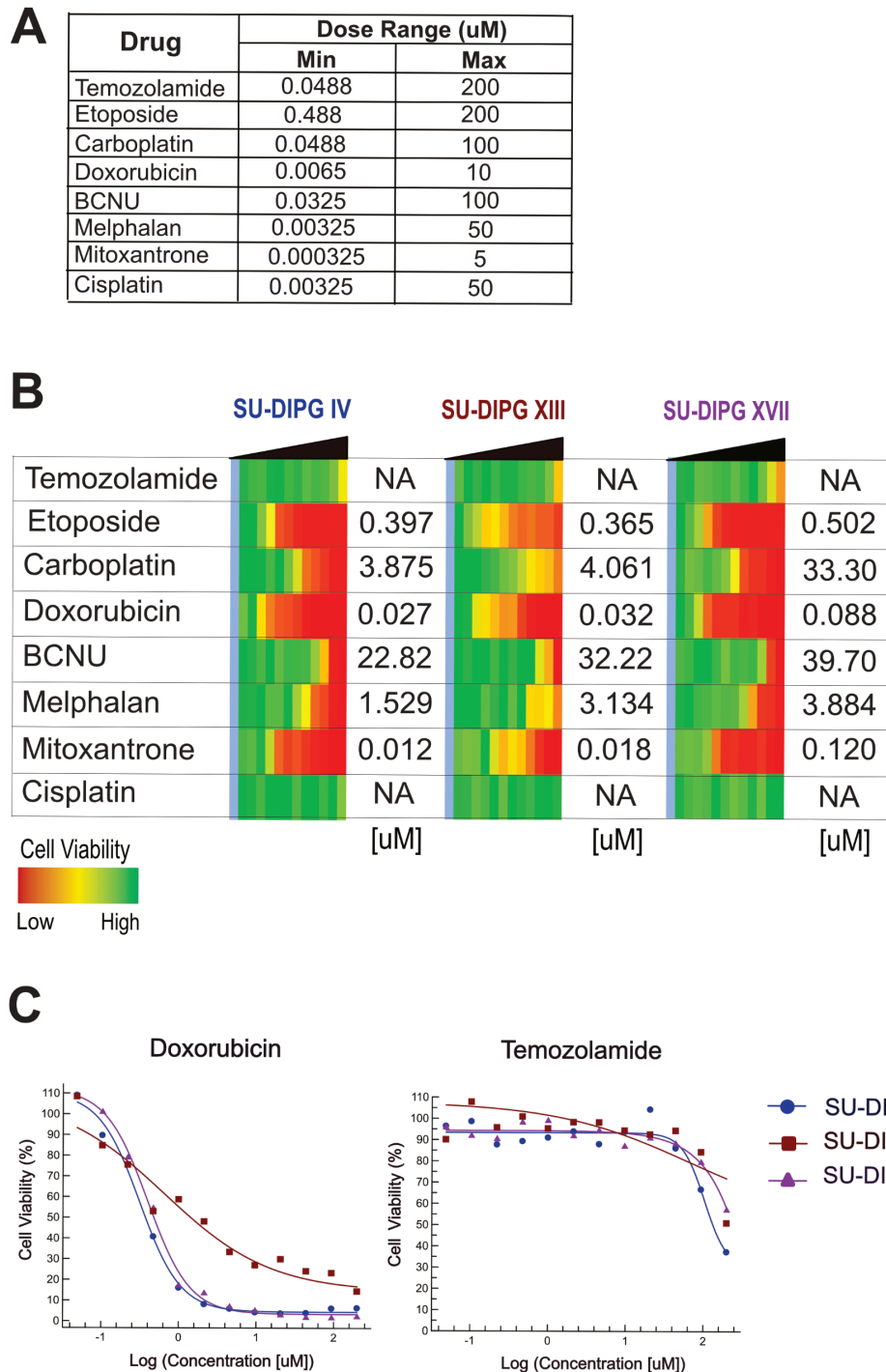
Figure 2.12: DIPG drug screen of conventional chemotherapeutics: A drug screen consisting of eight conventional chemotherapeutic agents was conducted in three patient derived DIPG cell lines (SU-DIPG IV, SU-DIPG XIII and SU-DIPG XVII). **(A)** Dose ranges for each drug tested are outlined and were obtained from previously published IC$_{50}$ data in the literature. **(B)** A heat map was generated from twelve-point dose escalation curves to demonstrate cell viability at escalating drug concentrations (left to right). **(C)** Dose escalation curves for Doxorubicin and Temozolamide are highlighted to demonstrate the differing efficacy of the two agents in our cell lines.

2.1.7 BBB disruption using MRgFUS enhances brainstem Doxorubicin uptake

Following its *in vitro* efficacy and with poor BBB permeability, Doxorubicin was selected as the chemotherapeutic agent with which to assess brainstem uptake when combined with focused ultrasound treatment **(Fig. 2.13).** The poor BBB permeability of Doxorubicin was confirmed in mice randomised to the "no intervention" group who received a 5mg/kg intravenous dose of Doxorubicin and who were subsequently found to have a mean brainstem value of 7.6ng/g at two hours. Similarly, low values of 18.7 ng/g and 12.31 ng/g were recorded in control groups receiving intravenous doxorubicin with either focused ultrasound energy alone (MRgFUS) or μBs alone. Successful BBB opening with MRgFUS and μB in combination with IV doxorubicin however, resulted in a significantly higher brainstem doxorubicin level of 431.5 ng/g. This is more than a 50-fold increase compared to the "no intervention" cohort and corresponds to a doxorubicin concentration of 824.2 nM (using a brain density of 1.04 g/m[224] This exceeds the mean IC$_{50}$ value of 49 nM of Doxorubicin recorded in our cell lines.

Furthermore, MRgFUS + μB + Doxorubicin treated mice showed significantly higher uptake in the brainstem alone as compared to the cerebrum and cerebellum (p<0.001). This is attributed to the targeted and focal disruption of the BBB in the brainstem using MR image guidance.
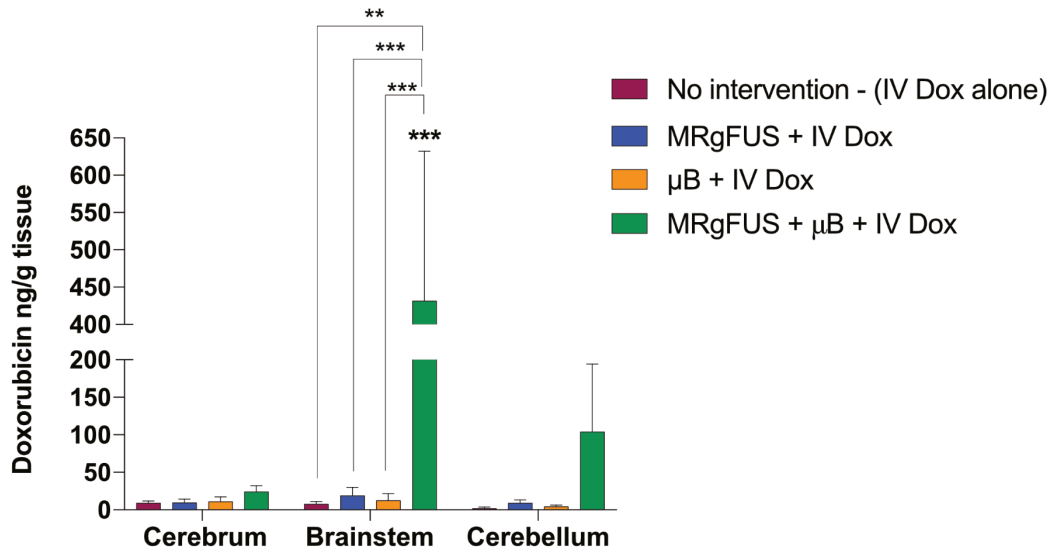
Figure 2.13: Brain Doxorubicin Distribution following MRgFUS delivery. NOD/SCID/GAMMA mice were injected with 5mg/kg intravenous Doxorubicin with either no intervention, microbubbles alone (B), focused ultrasound alone (MRgFUS) or both microbubbles and focused ultrasound (MRgFUS + B). Focused ultrasound, when used, was targeted at the brainstem specifically. Greatest Doxorubicin uptake was seen in the brainstem of the MRgFUS + B treated group as compared to all other groups and brain regions (two- way mixed ANOVA, ** $p < 0.01$, *** $p < 0.001$).

2.2 Discussion

In this study, it has been demonstrated that effective BBB disruption in the rodent brainstem can be achieved without evidence of tissue injury or functional motor deficit. By using a 4-point sonication grid in each half of the pons, it was possible to achieve diffuse BBB opening in the region, confirmed by both gadolinium contrast enhancement on T1 weighted imaging and Evans Blue staining of the tissue. Following BBB disruption, there were no statistically significant alterations in critical cardiorespiratory vital signs that would indicate functional injury to autonomic control centres located within the substance of the brainstem. In addition, evaluation of motor pathways and cerebellar function revealed no decline in function as measured by retained grip strength and rotarod

performance. Histological analysis of the sonicated regions of the brainstem at both early (4 hours) and late (14 day) time points revealed preserved brainstem architecture and neuronal numbers without activation of caspase 3 activity. BBB disruption and the administration of the chemotherapeutic agent, cisplatin (1.5 mg/kg), was well tolerated without evidence of physiological brainstem dysfunction.

Further to this, a drug screen of existing chemotherapy agents identified doxorubicin as an effective agent against patient derived DIPG cell lines. Doxorubicin is known to have poor BBB permeability[225,226] but when combined with MRgFUS BBB disruption, highly effective passage of the drug into the brainstem was demonstrated. Importantly, the concentration reached in brainstem tissue far exceeded the *in vitro* IC$_{50}$ concentration. The targeted brainstem BBB penetration also resulted in focally enhanced doxorubicin uptake to the region with limited uptake in other brain regions. Taken together, the data suggests that MRgFUS can be used to safely target the pons in an experimental model system and can significantly enhance drug delivery to the region. This technique may be a novel and exciting strategy to treat a brainstem-specific disorder, such as DIPG.

To date, all chemotherapy trials for DIPG have failed to show improvements in overall survival. While treatment failures may relate to the selection of non-targeted drugs for DIPG or intrinsic tumour cell resistance mechanisms, another reason for failures may be the difficulty associated with achieving sufficient intra-tumoral doses within the brainstem[227]. The eloquent location of tumour in the brainstem and preservation of the BBB favour methods of drug delivery that are both non-invasive and low risk. Although efforts should be made to improve our understanding of the chemosensitivity of DIPG tumour cells, focal disruption of the BBB in a transient manner would ensure adequate

delivery of appropriately selected drugs. As has been demonstrated in previous studies in the supratentorial compartment in human trials, MRgFUS allows for non-invasive, focal, reversible and repetitive BBB disruption[228].

Convection enhanced delivery (CED) is an additional technique that has been employed to improve the delivery of chemotherapeutics to the brainstem (see NCT01502917). The modality is currently not clinically approved but promising recent developments in the field include the successful completion of a phase 1 trial in patients with DIPG[229], FDA approval of a multi-port catheter and the safe delivery of sequential CED treatments[230]. However, no drugs are currently approved for direct delivery into the brain parenchyma and CED requires the invasive insertion of stereotactically guided catheters directly into the brainstem. In addition, CED has several limitations: Only small volumes ($\sim$ 3 – 4 mls) can be administrated safely; and only low infusion rates are tolerated[231]. In addition, with CED, drug reflux along the proximal catheter[141] and the limited extracellular space in the brainstem[231] hinder drug distribution, necessitating the use of multiple catheters[232]. As such, currently described methods of CED are best suited to short term drug delivery[141].

There were some limitations to MRgFUS disruption of the BBB in the brainstem in this study. In the rat, the depth of MRgFUS targeting is somewhat challenging due to the small size and shallow configuration of the cranial vault. As a result, the centre point of the MRgFUS target is set more posteriorly towards the cerebellum to minimize reflections of the ultrasound beam from the skull base. Such reflections can considerably increase the acoustic intensity and cause harm[233]. The use of a more posteriorly placed FUS target may help to explain the accumulation of some Evan's blue dye in the cerebellum relative to the brainstem in cross section. In mice, this also likely explains the increase in doxorubicin

detected in the cerebellum in the "MRgFUS + µB" group although this was not a statistically significant increase. In addition, we used a single FUS transducer in our rodent model. The use of a single transducer limits the specificity of the targeted focal area resulting in an ellipsoid shaped region of coverage[234]. The geometry of the human brain permits the use of multiple transducers which improve the ability to achieve discrete in-depth focusing. The clinical transducer is also better able to reduce the distortion of the ultrasound wave from variations in thickness of the skull[235]. Nonetheless, BBB disruption was confirmed on MRI following the administration of gadolinium using this technique. Evans Blue distribution in brainstem cross sections also clearly depicts that despite the aforementioned limitations, diffuse dye uptake was seen throughout the brainstem at the level of the pons. It is anticipated that even greater specificity of targeting of the pons will be possible with the use of MRgFUS in patients with DIPG where such anatomical constraints of the skull base are not so problematic.

The co-administration of cisplatin with the MRgFUS technique in this study was important to demonstrate that the delivery of a chemotherapeutic agent through the BBB and into the brainstem, did not cause harm. This was confirmed as rats in the "MRgFUS + µB + Cis" group did not show impaired function or tissue damage.

Cisplatin was chosen for use in the initial rat studies as it is a chemotherapy agent commonly used as part of combination chemotherapy regimens in the paediatric population. However, following its limited efficacy in DIPG cell lines, doxorubicin was chosen for use in the later mouse studies. In addition to its *in vitro* efficacy and poor BBB permeability, its pharmacokinetic profile has previously been studied in combination with MRgFUS mediated BBB disruption and the optimal delivery method to achieve high tissue penetrance whilst minimising toxicity has been determined[236].

Interestingly, in this study, both rat rotarod performance and grip strength were modestly improved after MRgFUS treatment of the brainstem. This is most likely attributed to enhanced performance by the rats from repeated measures as the same operator performed all measures pre- and post-procedure. This is a documented finding in the literature described as long-term improvement and is a more probable explanation than the μB or MRgFUS resulting in brain changes that would enhance their performance[237]. Throughout the motor assessments, a single operator was used to reduce the likelihood of variations attributed to technique.

The monitoring of cardiorespiratory parameters was undertaken for several minutes following MRgFUS and there is the potential that delayed cardiorespiratory effects arose. However, all rats reached the 14-day time point for histological analysis post treatment without any behavioural evidence of distress.

The μB dose used in our study was twice that of the maximum clinical dose. However, in clinical translation, more focal locations could be treated following a single bolus by scanning the ultrasound focus faster than is achievable with the small animal platform used in this study. Alternatively, a lower μB dose per injection could be used to allow more sonications within the allowable total dose[238]. Thus in practice, treatments could be performed without exceeding the maximum clinical dose.

Although the use of MRgFUS as a repeatable therapy is proposed, the safety of repeated treatments has not been assessed in this study. However, repeated focused ultrasound treatment of the visual pathways has been previously performed in rhesus macaques and did not result in either histological damage, behavioural change or the ability of the animals to perform complex visual tasks[233]. Kovacs *et al.* however, have described sterile inflammation arising in the brain parenchyma of rodents treated with

MRgFUS[239]. We attribute this to the group's use of a single, fixed ultrasound pressure as well as a significantly higher µB dose, with both factors having been shown to result in tissue injury[187]. Our utilisation of a hydrophone receptor enables the detection of ultra and subharmonic emissions indicating stable microbubble cavitation and the automated selection of a sonication pressure previously validated to achieve consistent BBB opening without tissue damage[187]. McMahon *et al.* have also conducted a study directly comparing these parameters. They were able to demonstrate contrasting differences in the degree of inflammatory response and tissue damage consequent to the differing parameters[240].

Following the demonstrated feasibility of MRgFUS BBB disruption in the rodent brainstem, the degree of enhanced drug uptake in the region was quantified using LC/MS. The high doxorubicin concentration recorded in the brainstem at two hours is considerable given both the short plasma and tissue half-life of unencapsulated doxorubicin (5.3 minutes and between 9-23 minutes respectively)[241]. This enhanced drug uptake in the region of MRgFUS and doxorubicin treated tissue has been shown to persist at 24 hours in a supratentorial high grade tumour model[242]. Rather uniquely, MRgFUS enables focal BBB opening with significantly enhanced doxorubicin uptake in the brainstem alone as compared to all other brain regions. However, the ability to reach brainstem concentrations that exceed *in vitro* IC50 concentration still may not confer a meaningful therapeutic response, and this will be the subject of further work validating the use of MRgFUS in DIPG mouse models. It is not clear from LC/MS whether the drug persists within the brainstem microvasculature or the parenchyma. However, the ability to achieve such a concentration with an intravenously administered drug confers significant promise in a disease process in which the BBB is a significant barrier to drug delivery.

3 Pre-clinical models of DIPG for MRgFUS delivered therapeutics

3.1 Results

3.1.1 Both the RCAS GEMM and SU-DIPG XVII xenograft show clinical relevance to DIPG

In order to investigate the effects of focused ultrasound mediated delivery of doxorubicin *in vivo*, I sought to recapitulate a mouse model of DIPG that reflects both the genetic aberrations and BBB impermeability of the tumour. Two mouse models were produced; an orthotopic xenograft of SU-DIPG-XVII and a genetically engineered mouse model using the RCAS/Tv-a system **(Fig. 3.1).** The specific focus of the latter model was to generate H3.3-K27M, PDGFB overexpression and p53 knockout in the Nestin compartment of brainstem neural progenitor cells. The model has previously been described in the literature as being a valid system for pre-clinical testing of therapeutics[28].

On histological analysis, the SU-DIPG-XVII xenograft exhibited an infiltrative growth pattern confined to the brainstem with absence of a clearly defined margin, closely resembling that seen in human DIPG **(Fig 3.1 - A).** Comparatively, the Nestin-Tva model resulted in a focal and discrete tumour localized to the brainstem **(Fig 3.1 - C).** Despite these morphological differences, both tumour models demonstrated a similar expression pattern of molecular markers for DIPG including Nestin positive expression, loss of p53 and histone H3K27 trimethylation with a high Ki-67 proliferative index **(Fig 3.1 - B and D).**

An assessment of survival of the respective models demonstrated a median survival of 48 days for the Nestin-Tva mouse model and 164 days for the SU-DIPG XVII xenograft **(Fig. 3.1 - E).** These survival times were significantly different compared to control mice (Nestin Tva mice not injected with RCAS vectors and NSG mice respectively)

and to one another by both the Mantel-Cox and Gehan-Breslow-Wilcoxon tests (log-rank p = 0.0001, GBW p = 0.0005; α threshold = 0.016 by Bonferroni correction for multiple comparisons).
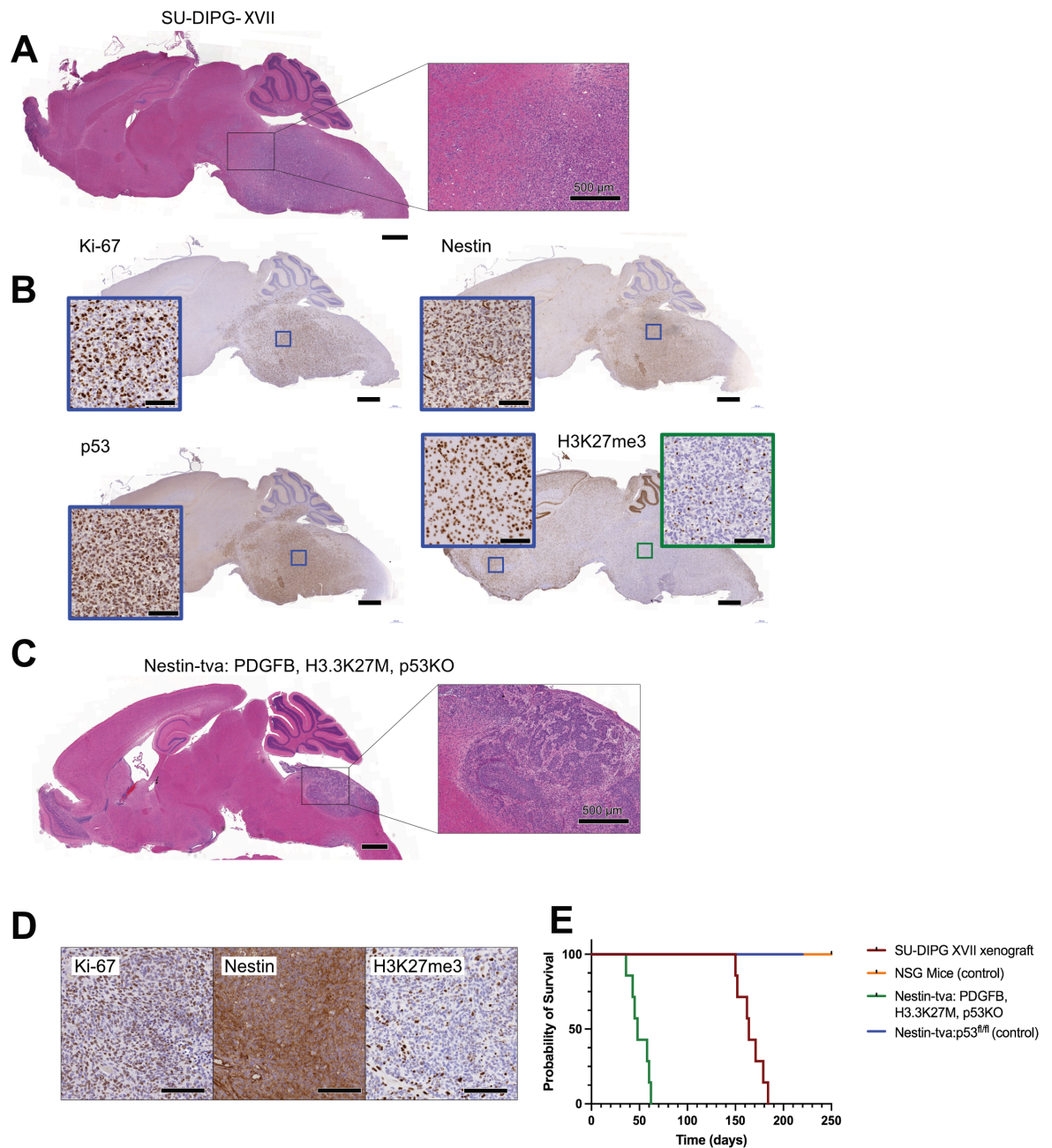
Figure 3.1: DIPG mouse models. The SU-DIPG XVII and RCAS DIPG mouse models exhibit different morphological features with the same molecular markers as clinical DIPGs. **(A)** The SU-DIPG XVII xenograft model produced a diffusely infiltrative tumour on H&E staining. **(B)** Immunohistochemistry on SU-DIPG XVII xenografts revealed expression patterns of four common DIPG molecular markers (Ki-67, Nestin, p53 and a loss of H3K27me3) that closely resembled those seen in clinical patient samples.

(C) H&E staining of 45 day old Nestin-Tva;p53 floxed mice injected with RCAS-Cre, RCAS-PDGFB and RCAS H3.3K27M vectors at P2 demonstrates a more focal and well circumscribed tumour in the brainstem. **(D)** Immunohistochemistry on RCAS DIPG tumours showed similar expression patterns as clinical samples. **(E)** Kaplan-Meier survival analysis of the SU-DIPG XVII xenograft model and Nestin-tva:PDGFB, H3.3K27M, p53KO mouse model.

3.1.2 The RCAS GEMM and SU-DIPG XVII xenograft differ significantly in their BBB permeability

MRI assessment of SU-DIPG-XVII xenografted animals at 100 days post tumour induction demonstrated brainstem tumours that were visible as hyperintense, poorly circumscribed lesions on T2-weighted images but were not discernible from normal brain tissue on T1-weighted imaging **(Fig 3.2 - A).** In addition, the tumours did not enhance following contrast agent administration **(Fig. 3.2 - A).** The absence of contrast enhancement indicates preservation of the BBB within the SU-DIPG-XVII tumour xenograft. The integrity of the BBB was maintained with progressive tumour growth at 170 days post tumour induction **(Fig. 3.2 - B).**

Imaging of RCAS/Tva DIPG mice demonstrated tumour lesions that were similarly evident on the T2-weighted images to the SU-DIPG XVII xenografted mice; however, they also appeared hyperintense and discrete on contrast-enhanced T1-weighted images after gadolinium administration **(Fig. 3.2 - C).** This indicator of BBB disruption in the tumour was further exhibited by the leaching of intravenously administered Evans Blue dye on tissue analysis **(Fig. 3.2 - D)**. There was no leaching of Evans Blue dye in the tumours of the SU-DIPG XVII model **(Fig. 3.2 - E)** or in the brainstem of control NSG mice **(Fig. 3.2 - F).** Hence the RCAS Tva DIPG model produced a tumour that resulted in BBB disruption in its development. This is unlike the clinical imaging findings of DIPG in children and confers a

confounding factor in the utility of the RCAS Tva DIPG model in testing focused ultrasound delivered chemotherapeutics.
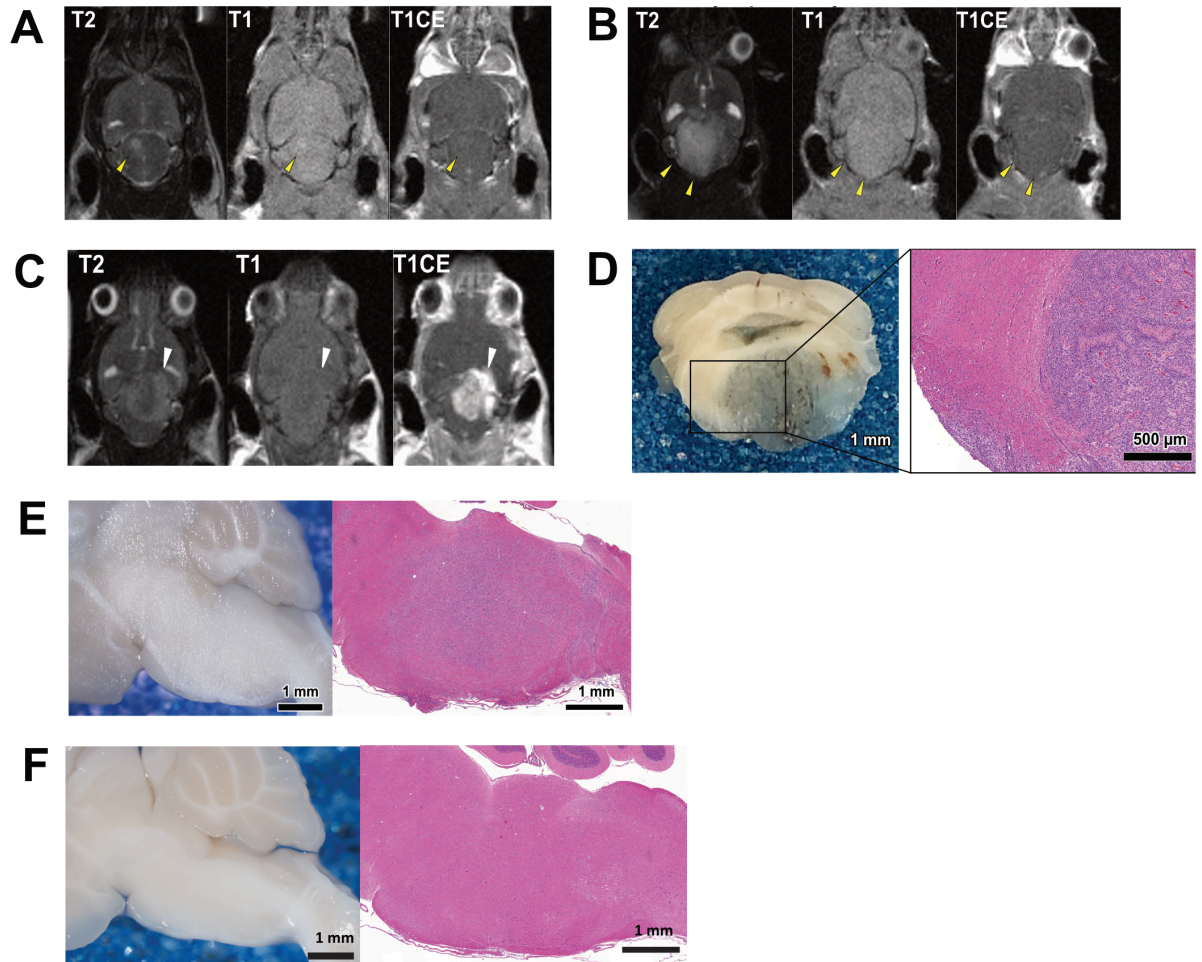
Figure 3.2: BBB permeability in DIPG mouse models. (A) MR Imaging of the SU-DIPG XVII mouse model at 100 days post induction revealed a diffusely infiltrative tumour on T2 weighted sequences (yellow arrowhead). The tumours were not distinguishable on T1 weighted images (T1), even after contrast administration (T1CE). **(B)** These findings were consistent even at 170 days as the tumours grew larger. **(C)** The RCAS DIPG model was avidly contrast enhancing following gadolinium administration (T1CE). **(D)** RCAS model tumours also demonstrated uptake of Evans Blue dye. **(E)** SU-DIPG XVII mice tumours did not demonstrate Evans Blue staining which was consistent with control NSG mice **(F).**

3.1.3 SU-DIPG-XVII Xenografts demonstrate brainstem impermeability to doxorubicin

To corroborate the preservation of the BBB in the SU-DIPG XVII mouse model, intravenous doxorubicin was administered at a dose of 5mg/kg doxorubicin to a cohort of animals. The brainstem tissues were extracted for the targeted tumour area. There was no significant difference between the levels of drug in the brainstem, plasma and the brainstem/plasma ratio of normal NSG mice (49.36 ± 8.36 ng/g$_{tissue}$, 229.9 ± 39.6 ng/ml, 0.24 ± 0.05, respectively; n = 8) and SU-DIPG-XVII xenografts (52.29 ± 6.65 ng/g$_{tissue}$, 334.6 ± 67.3 ng/ml, 0.17 ± 0.037; n = 8) via LC-MS/MS **(Fig. 3.3).** This provided further evidence of BBB integrity in the SU-DIPG XVII brainstem xenografts. Thus, the SU-DIPG XVII xenograft is the more appropriate and translatable model with which to determine how effective temporary BBB disruption with MRgFUS enhances tumour treatment.
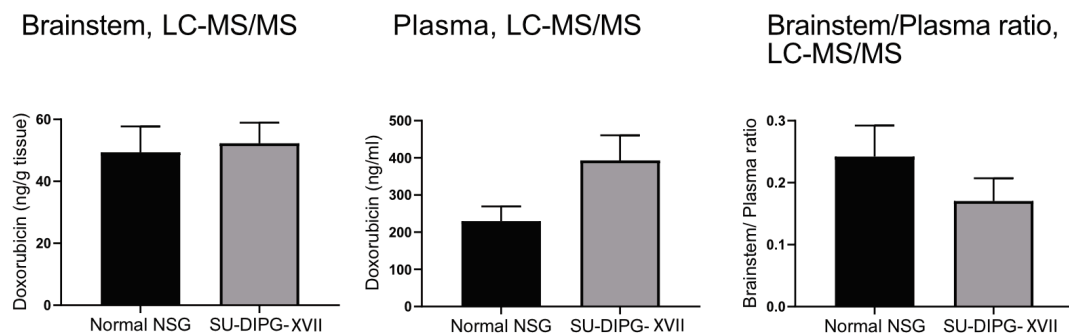
Figure 3.3: SU-DIPG XVII brainstem impermeability to doxorubicin. Intravenously administered doxorubicin showed no difference in uptake between SU-DIPG XVII xenografts and NSG brainstems as measured by LC-MS/MS (n =8; p = NS).

3.2 Discussion

In order to assess the pre-clinical utility of MRgFUS in the treatment of DIPG, two murine models were developed; a genetically engineered mouse model utilising the RCAS-Tva viral system to produce p53 knockout, H3K27M and PDGFβ expression in nestin

expressing cells of the neonatal brainstem and a xenograft using brainstem transplantation of the SU-DIPG XVII patient derived cell line. These models both expressed key molecular markers of DIPG but showed distinct differences in their brainstem BBB permeability, survival and tumour histology. Tumorigenesis in the RCAS model develops in the early neonatal period and median survival was limited to 48 days. However, the resultant tumour was discrete and resulted in disruption of the BBB limiting its utility in the pre-clinical study of MRgFUS delivered therapeutics. Conversely, the SU-DIPG XVII xenograft resulted in a longer median survival of 164 days, a more diffuse tumour growth pattern and rather crucially, preserved integrity of the brainstem BBB.

The development of two DIPG mouse models was integral to the long-term goal of determining whether MRgFUS delivered therapeutics confer treatment potential. The RCAS modelling system enabled the targeting of specific Nestin expressing postnatal cell population within the murine brainstem to develop into tumours. This resulted in a geographically and temporally accurate pre-clinical model of DIPG. Furthermore, the key genetic aberrations of H3.3K27M and TP53 inactivation were present. However, it should be noted that Pdgfβ overexpression was utilised in this model but this is rarely amplified in the disease. Its utility is in generating a highly aggressive tumour type, particularly in combination with TP53 loss and this likely led to the poor survival of these mice[243]. It is also known that H3.3K27M is the initiating mutation in the clonal evolution of DIPG[36,244] and although the mechanism as to how this leads to tumour formation is not yet understood, in the RCAS model, its role is rather that of an accessory mutation introduced at the same time as the other genetic mutations. Its contribution to tumorigenesis in this model may not be the same as that seen in the disease. Prior studies suggest that it contributes to accelerated tumour growth and progression although the comparative

difference to RCAS-Cre p53KO PDGFB H3.3WT mice survival was minimal[28]. Indeed other pre-clinical models have failed to achieve tumorigenesis with H3.3K27M as an isolated mutation[89]. PDGRFA signalling however, has been shown to achieve tumorigenesis with wild-type H3.3[28,197].

The observed brainstem BBB permeability in the RCAS derived DIPG model is likely a consequence of the paracrine effects of PDGFB which have been shown to cause vascular remodelling and angiogenesis[88]. Such extensive BBB permeability therefore precludes its use in the pre-clinical testing of MRgFUS delivered chemotherapeutics. In addition, several practical factors are also unfavourable; the short survival time limits the window for therapeutic intervention and the small size of the mice at the time of intervention renders them susceptible to the effects of hypothermia when placed in ultrasound gel for optimised conduction of focused ultrasound.

Hence the SU-DIPG XVII model provides a histologically and phenotypically relevant model of DIPG for use in pre-clinical studies of MRgFUS delivered therapeutics. Interestingly, use of the model has not previously been published. Further characterisation however is required to determine whether tumour progression and dissemination mimics that of the clinical disease. In addition, the generation of a model from a single patient derived cell line in an adult mouse may bring into question the validity of any therapeutic response seen. This is of relevance as *in vitro* drug susceptibility varies considerably between cell lines[81]. A means to improve this could be the utilisation of cells obtained from multiple tumour biopsies or from heterogenous regions of the tumour that are combined prior to implantation[245,246]. An immunodeficient model may also not accurately depict a possible adverse inflammatory reaction from MRgFUS which is a concern previously raised by Kovacs *et. al*[239] That said, there is significant utility in the

quantification of drug delivery beyond an intact BBB and optimisation of this is the first step prior to the expectation of a meaningful treatment response.

Since the completion of this study, DIPG mouse models have been developed that introduce the H3.3K27M mutation into neural precursor/stem cells (NPCs) using the technique of in utero electroporation (IUE) at embryonic day 13.5 in transgenic mice[88,89]. This timing has been chosen to coincide with the peak of pontine neurogenesis. These studies suggest that when H3K27M arises in specific NPC populations *in utero,* it disrupts neurogenesis and leads to the development of highly penetrant tumours. This may explain why DIPG occurs so specifically in early childhood. Furthermore, the presence of H3.3K27M in NPCs seems to be of greater significance in combination with pdgfra over activation and dominant negative Trp53 (dnTrp53), demonstrating a shorter latency to neurological symptoms and a more significant reduction in overall survival[88]. This significance is not apparent when H3.3K27M is combined with PDGFB and dnTrp53. Interestingly, the gene expression profiles have been shown to differ significantly depending on whether PDGFB or pdgfra over expression is present. PDGFB tumours show a high expression of proneural genes whereas pdgfra tumours show a higher expression of genes associated with classical and mesenchymal subtypes. As such, DIPG is the likely result of a complex interaction between these mutations that arise *in utero* and their resultant gene expression profiles. Pathania *et al*. also demonstrated genetic signatures that closely approximated those of human K27M tumour signatures in their model.[89] Given their faithful recapitulation of the human disease, it would be interesting to assess the integrity of the BBB in these models and determine their suitability for MRgFUS mediated drug delivery.

4 Drug screen of new molecular therapies and synergy analysis

4.1 Results

4.1.1 PARP inhibitors are potent against DIPG cell culture

A drug screen consisting of ten molecular therapies classified as either PARP inhibitors, tyrosine kinase inhibitors or HDAC inhibitors were tested in DIPG cell lines (**Fig. 4.1 and 4.2**). The PARP inhibitors Niraparib and Talazoparib along with the HDAC inhibitors Panobinostat and Vorinostat demonstrated particular potency with the lowest IC50 values (mean values of $0.86\mu M$, $0.3\mu M$, $0.01\mu M$ and $0.65\mu M$ respectively). Panobinostat was the most potent drug in the SU-DIPG IV cell line (not tested in SU-DIPG XVII). Talazoparib however was tested in both cell lines and demonstrated potency in both. In addition, the SU-DIPG IV cell line was more susceptible to the effects of the PARP inhibitors than the SU-DIPG XVII cell line, requiring lower drug concentrations to achieve 50% growth inhibition **(Fig. 4.1 A-C).**

Drug	IC50 (uM)	
	SU-DIPG IV	**SU-DIPG XVII**
Olaparib	3.50	14.70
Niraparib	0.72	1.00
Talazoparib	0.06	0.54
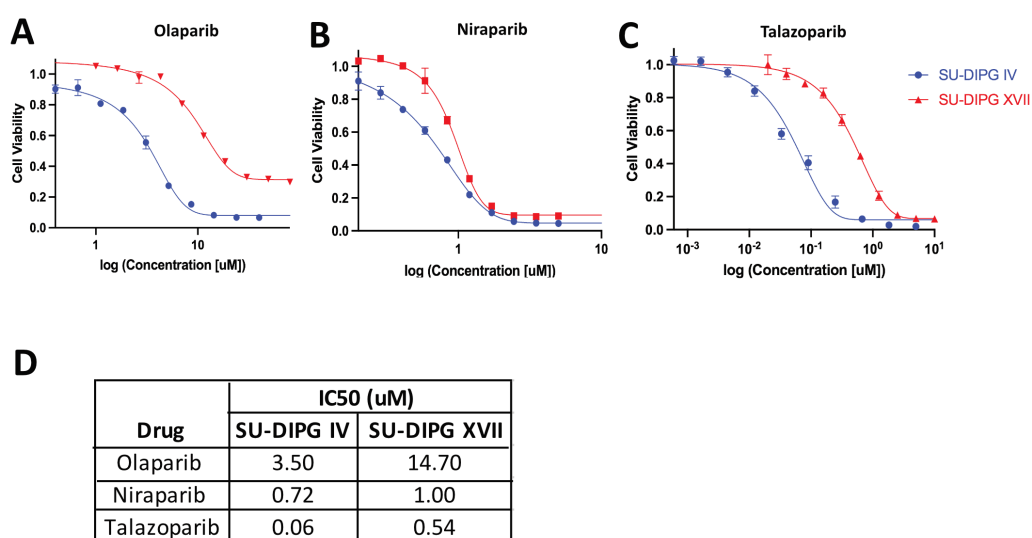
Figure 4.1: *In vitro* efficacy of PARP inhibitors against DIPG. (A - C) Dose response curves for Olaparib **(A)**, Niraparib **(B)** and Talazoparib **(C)** in SU-DIPG IV (blue) and SU-DIPG XVII (red) cell lines at 72 hours

post treatment. **(D):** IC50 data in SU-DIPG IV and SU-DIPG XVII cell lines demonstrates the superior potency of Talazoparib among the three tested PARP inhibitors.
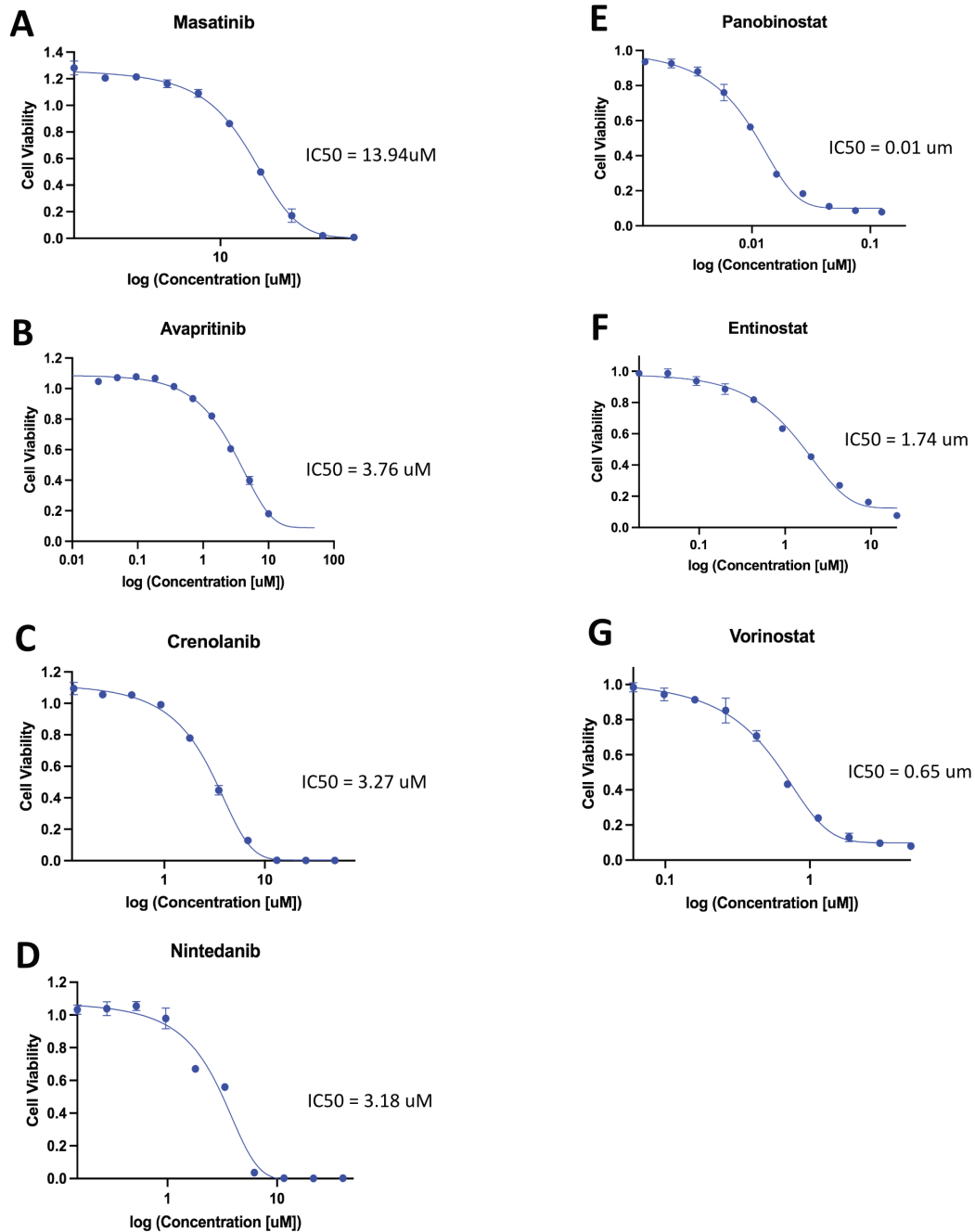
Figure 4.2: Dose response curves for Tyrosine Kinase (A - D) and Histone Deacetylase inhibitors (E - G). Dose response curves for the tyrosine kinase inhibitors Masatinib **(A),** Avapritinib **(B)**, Crenolanib **(C)** and Nintedanib **(D)** and the HDAC inhibitors Panobinostat **(E)**, Entinostat **(F)** and Vorinostat **(G)** in

SU-DIPG IV cell lines at 72 hours post treatment. Panobinostat demonstrates the highest potency overall. The TK inhibitors achieve almost 100% growth inhibition at high doses.

4.1.2 PARP inhibitors act synergistically with doxorubicin

The PARP inhibitors Olaparib, Niraparib and Talazoparib demonstrate a synergistic effect with Doxorubicin in the SU-DIPG IV and SU-DIPG XVII cell lines with positive summary delta scores by the zero-interaction potency (ZIP) model of synergy analysis **(Fig. 4.3 and Fig. 4.4)**. The summary delta score represents the average overall interaction effect over all dose pairs for the three respective drug combinations with a positive score indicating a synergistic combination, a score of zero indicating dose additivity/zero interaction and a negative score indicating drug antagonism[218]. Furthermore, all three drug combinations exceeded a delta threshold of 0.05 which represents a 5% response beyond the expectation of zero interaction between the two drugs and indicates a high level of drug synergy[218].

Niraparib and doxorubicin demonstrated the highest synergy score in the SU-DIPG IV cell line **(Fig. 4.3 - D)** and Talazoparib and doxorubicin were the most synergistic combination in the SU-DIPG XVII cell line (ZIP synergy scores of 4.98 and 6.63 respectively) **(Fig. 4.4 - F).**

On review of the 2D synergy interaction landscape of niraparib and doxorubicin in SU-DIPG IV, **(Fig. 4.3 - D)** a dose combination of 409nM Niraparib with 9.3nM of doxorubicin resulted in the highest degree of synergy with a response that was 30% greater than that expected by the ZIP model. Similarly, in SU-DIPG XVII, 30% above expected inhibition was seen when Talazoparib was combined with doxorubicin but the effective dose combination was 79.5nM Talazoparib and 22.7nM doxorubicin. These highly synergistic regions correspond to the midpoint of the dosing range for both drugs.

In addition, both of these synergy maps demonstrate a strong degree of synergy across most of the dose – response matrix.

Although Olaparib demonstrated synergistic activity with Doxorubicin in both cell lines, the highest percentage above expected inhibition was 10% in SU-DIPG IV **(Fig 4.3 - B)** and 20% in SU-DIPG XVII **(Fig. 4.4 - D).** To achieve this in SU-DIPG XVII also required a high nanomolar concentration of Olaparib (4308.9 nM).
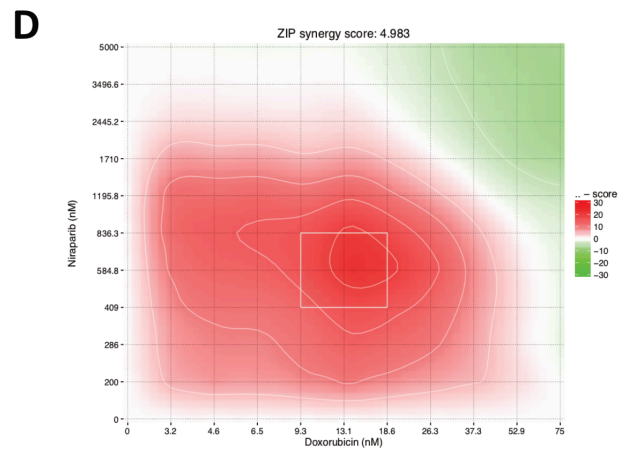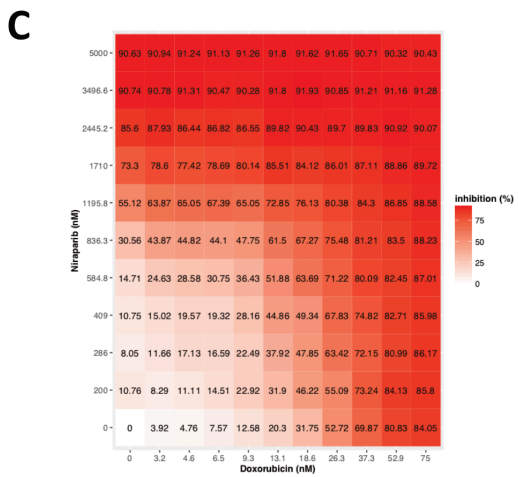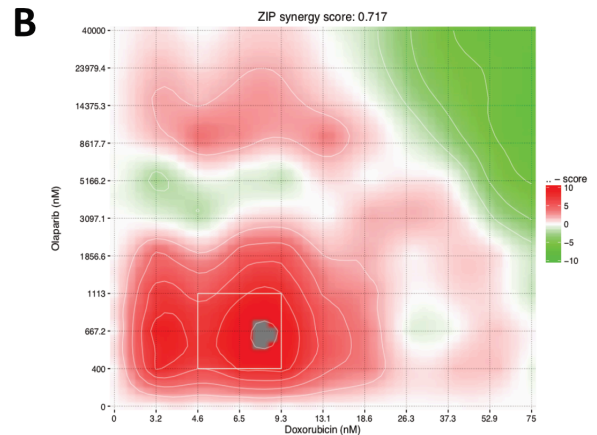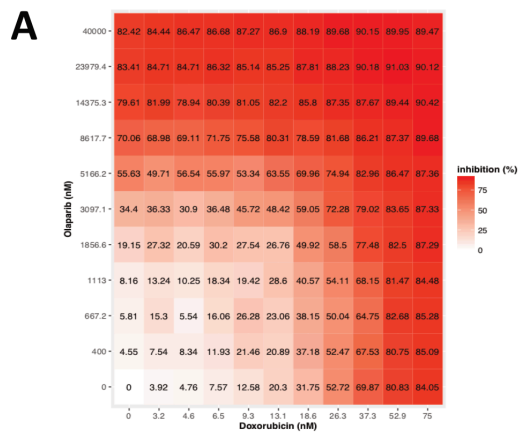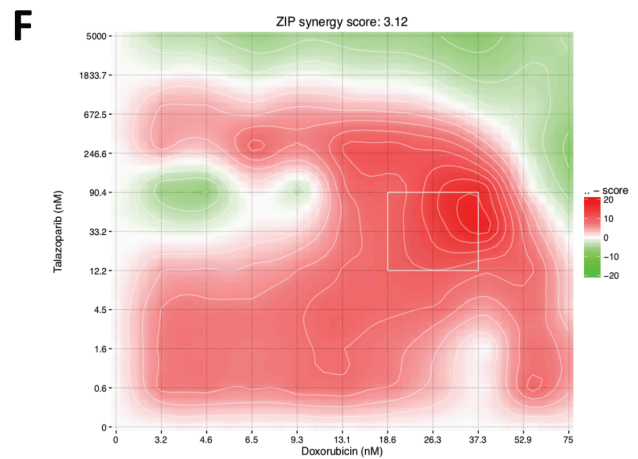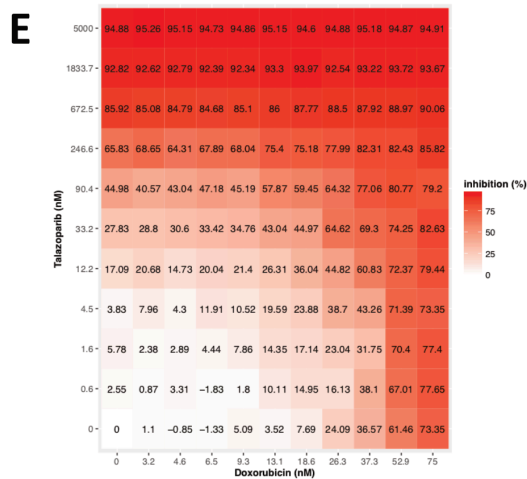
Figure 4.3: Zero interaction potency (ZIP) synergy analysis of PARP inhibitors (Olaparib, Niraparib and Talazoparib) with Doxorubicin in SU- DIPG IV cell lines. (A, C, E): Dose response matrices for Olaparib **(A)**, Niraparib **(C)** and Talazoparib **(E)** in combination with Doxorubicin in SU-DIPG IV cell lines at 72 hours post treatment. **(B,D,F)** 2D Synergy maps and corresponding ZIP synergy scores of Olaparib **(B)**, Niraparib **(D)** and Talazoparib **(F)** in combination with Doxorubicin demonstrate positive synergy scoring in all three combinations with Niraparib having the highest synergy score. These maps also demonstrate significant synergy across most of the dose-response matrix.
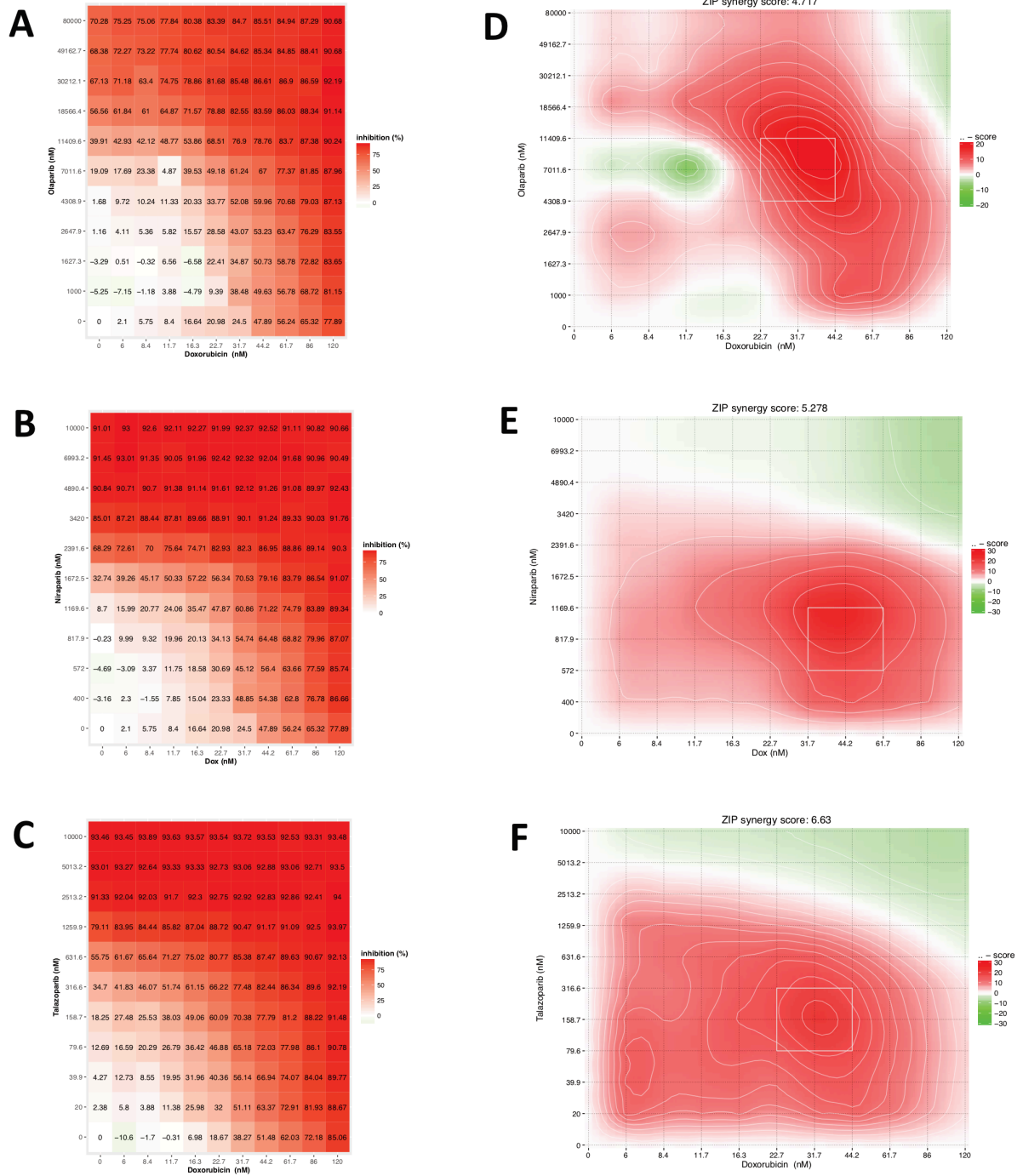
Figure 4.4: Zero interaction potency (ZIP) synergy analysis of PARP inhibitors (Olaparib, Niraparib and Talazoparib) with Doxorubicin in SU-DIPG XVII cell lines. (A - C) Dose response matrices for Olaparib **(A)**, Niraparib **(B)** and Talazoparib **(C)** in combination with Doxorubicin in SU-DIPG XVII cell lines at 72 hours post treatment. **(D - F)** 2D Synergy maps and corresponding ZIP model synergy scores of Olaparib **(D)**, Niraparib **(E)** and Talazoparib **(F)** in combination with Doxorubicin again demonstrate positive synergy scoring in all three combinations but Talazoparib has a stronger synergistic effect with doxorubicin in the SU-DIPG XVII cell line specifically. Regions of high synergy in the Niraparib and

Talazoparib synergy landscapes correspond to a growth inhibition response that is 30% higher than expected.

4.1.3 HDAC and TK inhibitors have an antagonistic action with doxorubicin

In contrast to the drug synergy between the PARP inhibitors and doxorubicin, the tyrosine kinase and HDAC inhibitors in this study demonstrated mostly an antagonistic action when combined with doxorubicin in DIPG cell culture **(Fig. 4.5 and 4.6).** The dose response matrices for TK inhibitors Masatinib, Crenolanib and Nintedanib show that at the highest doses of combination treatment, close to 100% cell inhibition is achieved **(Fig. 4.5 – A-D).** Despite this, synergy scores with doxorubicin were weakly positive for Masatinib and Nintedanib and negative for Avapritinib and Crenolanib **(Fig. 4.5 – E-H).** The 2D synergy maps highlight the vast areas of antagonistic drug action (green colour) in addition to areas of weak synergy (pale red) compared to the PARP inhibitors.

Despite the potency of Panobinostat monotherapy in SU-DIPG IV **(Figure 4.2 – E)**, the drug demonstrated a strongly antagonistic action with doxorubicin *in vitro* and this was also true for the HDAC inhibitors entinostat and vorinostat (ZIP synergy scores of - 2.44, -3.36 and -0.74 respectively) **(Fig. 4.6 D-F) .**
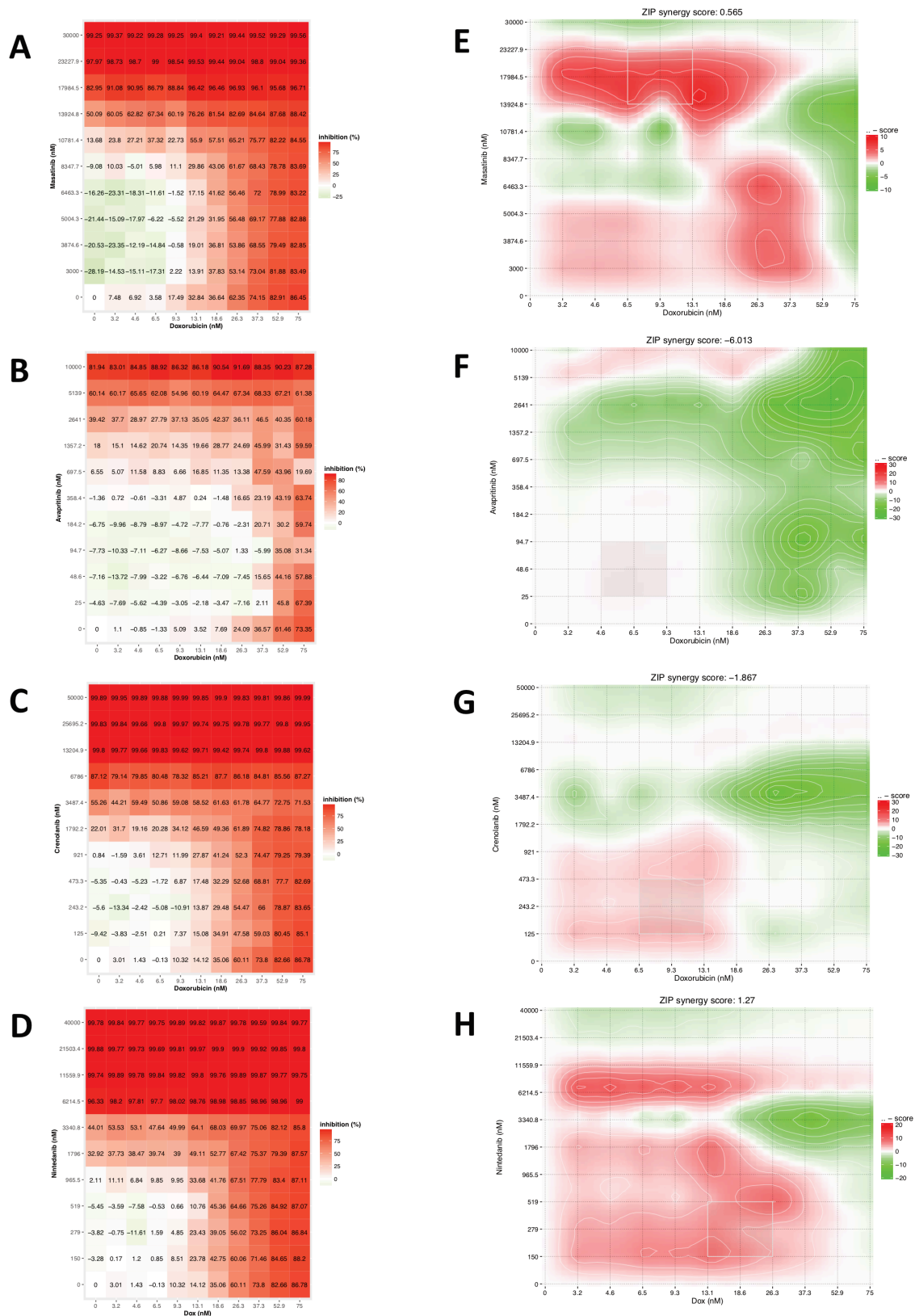
Figure 4.5: Zero interaction potency (ZIP) synergy analysis of tyrosine kinase inhibitors with Doxorubicin. (A-D): Dose response matrices of Masatinib **(A)**, Avapritinib **(B)**, Crenolanib **(C)** and Nintedanib **(D)** in combination with Doxorubicin in SU-DIPG IV cell lines at 72 hours post treatment. **(E-H):** 2D synergy analysis of TK inhibitors with Doxorubicin demonstrates antagonism of Avapritinib and

Crenolanib and minimally synergistic activity of Masatinib and Nintedanib when combined with Doxorubicin.
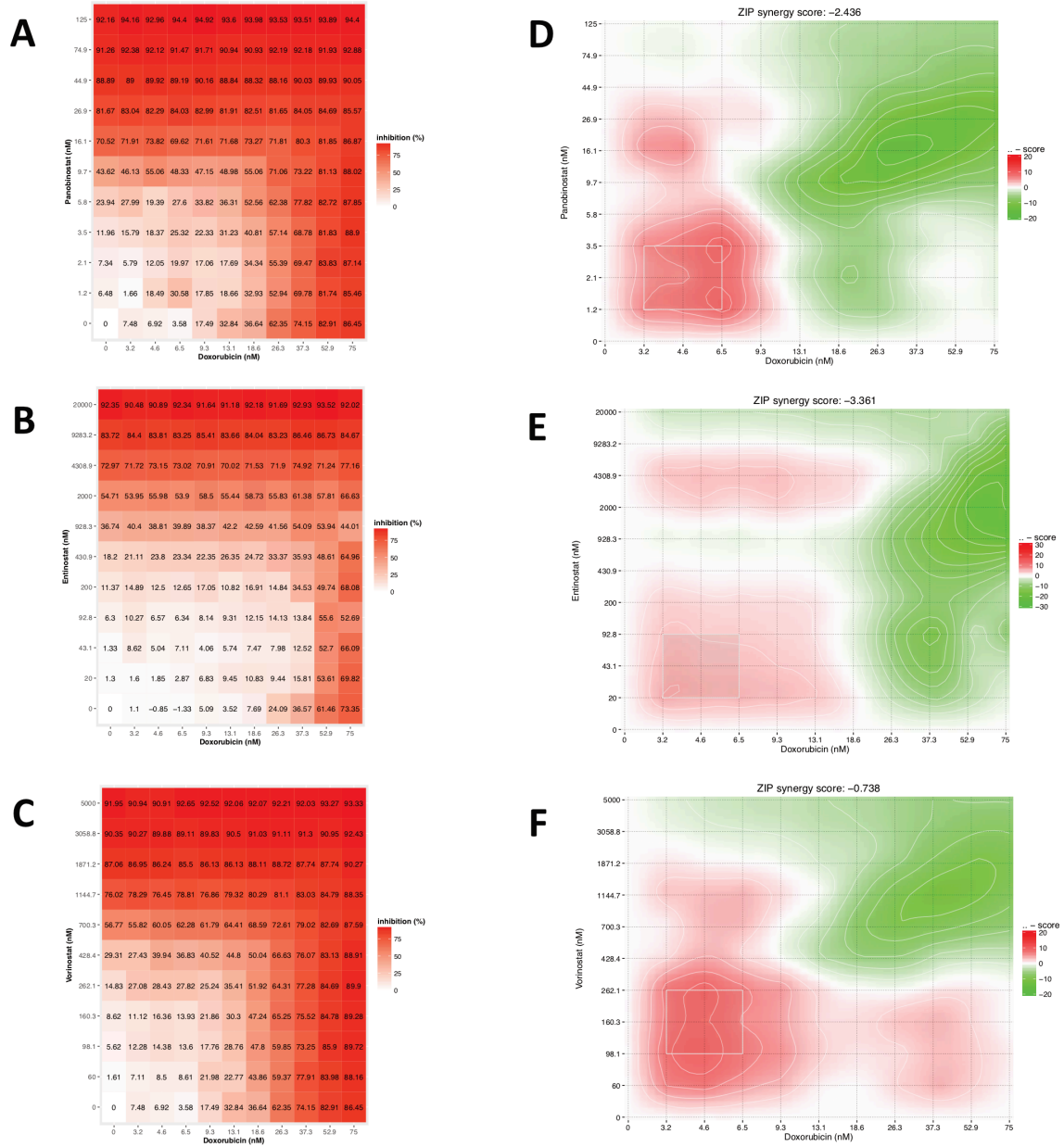
Figure 4.6: Zero interaction potency (ZIP) synergy analysis of histone deacetylase (HDAC) inhibitors with Doxorubicin. (A-C): Dose response matrices of Panobinostat **(A)**, Entinostat **(B)** and Vorinostat **(C)** in combination with Doxorubicin in SU-DIPG IV cell lines at 72 hours post treatment. **(D-F):** 2D synergy landscapes of HDAC inhibitors with Doxorubicin demonstrate areas of synergistic activity but a negative ZIP score overall indicating drug antagonism when combined with Doxorubicin.

4.2 Discussion

Newer molecular therapies were assessed *in vitro* for potential combination therapy with doxorubicin. The PARP inhibitors Olaparib, Niraparib and Talazoparib were shown to have strong synergistic activity with doxorubicin. Of these, Talazoparib appeared to have a low IC50 in addition to having strong synergistic activity with doxorubicin in SU-DIPG cell lines. Comparatively, TK and HDAC inhibitors had a largely antagonistic action with doxorubicin.

The synergistic effect of doxorubicin and PARP inhibitors can be explained by their mechanistic action; doxorubicin inhibits topoisomerase I and II causing single and double stranded DNA breaks (DSB)[247] and PARPi both promote DSB and impair the recruitment of enzymes instrumental in homologous recombination and the successful repair of these breaks[248]. Talazoparib is also a potent PARP trapper, binding to the PARP-Chromatin complex and trapping the enzyme in a non-effective state at chromatin[205,248].

PARP inhibitor therapy for the treatment of DIPG has previously been trialled, but this was primarily based upon their potential role as radiosensitisers in solid tumours[249]. Children with newly diagnosed DIPG were enrolled in a phase I/II trial of concomitant Veliparib and radiation therapy followed by maintenance treatment with Veliparib and Temozolamide[207]. Unfortunately, although the regimen was well tolerated, interim analysis failed to show a survival benefit and the trial was subsequently stopped due to futility.

Talazoparib however has been shown to have a more potent anti-tumour effect across multiple cancers due to its larger and more stereospecific structure which results in comparatively stronger trapping of PARP1 and PARP2[250,251]. This enhanced potency, however, is associated with greater toxicity to normal tissues and hence this profoundly

limits the maximum tolerated dose of Talazoparib as compared to other PARP inhibitors. This is reported to be as significant as 300 to 1200 times lower[205]. Niraparib however, demonstrated potency and an almost equivalent degree of synergy with doxorubicin but has been well tolerated in an adult clinical study[252]. In addition, it has been shown to have superior efficacy to Veliparib and Olaparib in DIPG cell culture and conferred improved survival in an orthotopic paediatric high-grade astrocytoma (pHGA) xenograft[206]. Niraparib and doxorubicin may therefore be a more practical combination to explore in further pre-clinical studies.

Drug toxicity is not limited to Talazoparib with doxorubicin known to have multi-organ effects with the most prominent being that of cardiotoxicity. The drug alters the structure of cardiac myocytes resulting in their enlargement which in turn causes cardiac hypertrophy. This injury to cardiac myocytes is believed to have several mechanisms including; increased gene expression of brain natriuretic peptide (BNP) and atrial natriuretic peptide (ANP), an increase in oxygen free radicals causing activation of apoptosis and stimulation of cytotoxic T lymphocytes resulting in an exuberant inflammatory response[247]. To help mitigate these adverse effects, dose limits are commonly imposed and liposomal formulations of doxorubicin are commercially available. Loading of doxorubicin within pegylated liposomes significantly reduces its bioavailability and the hydrophilic polyethylene glycol (PEG) coating prevents the binding of circulating opsonins and therefore recognition and removal by the reticuloendothelial system[253]. The pharmacokinetic effects are that of a reduced volume of distribution and delayed rate of clearance compared to standard doxorubicin[254]. A reduction in myocyte uptake of such formulations has been shown in clinical studies to reduce the cardiac toxicity of the drug[255].

In addition, doxorubicin has been shown to have neurotoxic effects both in the presence of an intact BBB[256] and when combined with an osmotic BBB disrupting therapy[257,258]. In the former study, despite the absence of doxorubicin in the brain parenchyma, circulating TNF-α was noted to be elevated following doxorubicin administration and resulted in increased brain levels with subsequent mitochondrial dysfunction and apoptosis. The extent of neurotoxicity however was more profound in studies where BBB disruption was performed with overt neurological deficits and pathological evidence of neuronal damage. Despite these concerning findings, Aryal *et al* were able to deliver a liposomal doxorubicin formulation with MRgFUS mediated BBB disruption in a multi-session treatment regimen with minimal brain tissue injury[259]. The results of this latter study should be taken with some degree of caution as the area of BBB disruption was smaller than that which is required for brainstem targeting and the location of opening was in the cerebral hemispheres and therefore a less eloquent region of the brain. Furthermore, the brain tissue injury seen may under-represent doxorubicin neurotoxicity as the drug levels detected in the brain were not distinguished as being in the free or encapsulated form. If the latter is predominant, more significant toxicity may be seen when the drug is subsequently released. However, histological analysis at 76 days would suggest that the majority of drug would be released. Unfortunately, the clinical condition of the rats following treatment was not reported and therefore it is not known if the tissue injury seen was sufficient to have clinical manifestations.

This latter study also raises an important point regarding the effect of focused ultrasound on liposomal drug formulations. The study suggested that high intensity focused ultrasound resulted in inertial cavitation and subsequent doxorubicin release from liposomes that caused tissue injury[259]. In contrast, Francois *et al*. have demonstrated

that low pressure ultrasound can enhance drug release from liposomal doxorubicin when conjugated to polymer microbubbles by as much as 70% [260]. This was dependent on a state of stable microbubble cavitation. Inertial cavitation in their study resulted in a more rapid but ineffective drug release from liposomes. Hence the presence of a hydrophone receptor for the detection of microbubble activity and the subsequent ability to achieve consistent stable cavitation is particularly important when considering the use of liposomal drug formulations with MRgFUS. Using such a formulation may enable reduced systemic toxicity and enhanced drug delivery but further work is required to confirm their safety and utility in brainstem delivery via MRgFUS.

Standard doxorubicin therapy has been mathematically modelled for use with MRgFUS BBB disruption with the finding that drug infusion over 20-60 minutes with either a single sonication or multiple sonications performed at 10-minute intervals would ensure significant intracellular doxorubicin delivery[236]. The slow infusion is also proposed to reduce the peak plasma concentration of the drug and therefore the associated cardiac toxicity. Several pharmacokinetic features also make it an attractive drug for use with MRgFUS. The distribution half-life is 3-5 minutes due to its rapid cellular uptake and it is able to accumulate intracellularly to 500 fold its extracellular concentration with a predilection for the nucleus where it has the capacity to intercalate at every fifth base pair on DNA[247]. Despite these promising properties doxorubicin is known to be actively expelled by permeability glycoprotein 1, (P-gp) – an ATP dependent transporter that removes drugs from the brain across the BBB as a protective mechanism[261] and is also over expressed in tumour cells, contributing to drug resistance[262]. The presence of these transporters reduces drug penetration into the brain by as much as $10 - 100$ fold[263]. It is therefore important to understand the role of MRgFUS on P-gp.

MRgFUS has been shown to inhibit P-gp expression in a magnitude specific manner such that higher acoustic pressures and a greater extent of BBB disruption result in greater P-gp suppression[264,265]. The downregulated expression is focal to the area of BBB disruption and persists for 48 hours after treatment with full recovery of expression by 72 hours[265]. This effect has been further characterised with the finding that P-gp transcription in brain vascular endothelium is downregulated via a c-Jun NH2-terminal kinase, (JNK) mediated pathway and that there was no such change in the expression of tight junction proteins suggesting the preservation of blood vessel integrity[266]. These findings in conjunction with the pharmacokinetic profile of doxorubicin make the drug a suitable first choice option for the assessment of therapeutic response in pre-clinical models of DIPG using MRgFUS.

Combination drug therapies are commonly used in cancer treatment due to intra-tumoral heterogeneity, the redundancy in oncogenic pathways and mechanisms of drug resistance[267]. The synergistic effect of doxorubicin and the PARP inhibitors has been successfully quantified in this study with Niraparib demonstrating a comparably favourable profile with a synergistic response 30% above its expected additive effect with doxorubicin. Rather importantly, a strong degree of synergy was evident across most of the 2D synergy map in both cell lines. Therefore, if there is variability in the dose of each drug reaching the target tissue, a more potent treatment response would still be seen with the combination therapy. This is particularly important as MRgFUS relies upon systemically administered drugs that will undergo varying degrees of metabolism prior to reaching their target. In addition, it may also be possible to reduce the doses of doxorubicin and niraparib administered, thereby reducing their toxicity but still achieving a significant treatment response. Identifying antagonistic drug combinations is equally important and

better identified in less costly *in vitro* studies. At times, this may also elucidate mechanisms of drug interaction that were not previously known.

Limitations to drug synergy analysis exist with each model due to the assumptions that they are based on and as such, it may be prudent to confirm drug synergy in more than one model. Further to this, many combination therapies have failed in clinical trials despite demonstrating pre-clinical efficacy. Reasons for this include insufficient drug dosing, a failure to assess biomarkers of treatment response as well as combination drug toxicity[268]. The findings of this study should therefore be used to inform further pre-clinical studies of MRgFUS delivered therapeutics in the SU-DIPG XVII xenograft.

5 Conclusion and Future Work

DIPG remains a particularly tragic disease with a rapid course and fatal prognosis. This fact remains unchanged despite significant gains in our understanding of the molecular events that underpin the disease. The search for potential therapeutics is an important focus for research but of equal importance is their successful brainstem delivery given the preservation of the BBB. In this study I chose to focus on the use of MRgFUS to disrupt the BBB in the murine brainstem. Although high frequency MRgFUS is in clinical use for tissue lesioning worldwide and low frequency ultrasound has been delivered as part of several ongoing clinical trials[228], the feasibility and safety of attempting brainstem BBB disruption was unclear. Hence in this study I was able to demonstrate murine BBB disruption whilst preserving brainstem architecture and without subsequent tissue injury. Key brainstem functions of cardiorespiratory control, motor strength and co-ordination were shown to be preserved. Further to this, I was able to successfully deliver the chemotherapy agent doxorubicin achieving a drug concentration within the brainstem that was 50 -fold higher than that achieved in control mice. To date there is no other published data demonstrating brainstem BBB disruption using focused ultrasound making this a novel therapeutic approach.

I chose to conduct these experiments using a non-invasive MRI-compatible pre-clinical low frequency ultrasound delivery system (LP-100, FUS Instruments Inc, Toronto). This decision was based on the knowledge of an equivalent non-invasive commercially available device for future clinical translation (Exablate Neuro, Insightec, Inc., Haifa, Israel). An alternative ultrasound delivery system has been used in the brain for BBB disruption[269,270]. The SonoCloud-1 (CarThera, Paris) however, requires a burr hole for

implantation into the skull and delivers unfocused ultrasound energy via nine 1cm transducers arranged in a grid. Both devices have their limitations[271]. The SonoCloud-1 requires surgical implantation, and the location of implantation is determined by the area to be targeted. Therefore, the treatment of two remote targets would require more than one implantation. The unfocused nature of the ultrasound energy also results in a more diffuse area of BBB opening which may not always be desired. The Exablate neuro is entirely non-invasive, has over 500 transducers for very focal BBB opening and can treat more than one target without adjustment. The treatment of larger areas however requires considerably more time. Given the intent to treat a paediatric patient population and the potential for disseminated disease following local control, I felt that the attributes of the non-invasive delivery system were more appropriate.

Recognising the need for further pre-clinical studies in MRgFUS brainstem drug delivery, I produced two DIPG mouse models and along with the work of Dr Ishida, we were able to demonstrate that the PDX SU-DIPG XVII mouse model faithfully recapitulated a diffuse brainstem tumour with histological markers of DIPG, shortened survival and an intact BBB. This was a surprising finding particularly as the GEMM demonstrated a discrete rather than diffuse tumour growth pattern and a disrupted BBB. As previously mentioned, the findings in the GEMM are likely secondary to the paracrine effects of PDGFB which result in angiogenesis. The ability of the xenograft to generate diffuse tumours is not understood and may be due to the behaviour of the cell lines which requires further study and characterisation to determine.

Following this, I identified doxorubicin and the PARP inhibitors Talazoparib and Niraparib as having a high degree of synergy for a potential effective combination therapy.

This study has therefore laid the groundwork for further pre-clinical investigation of MRgFUS as a modality for drug delivery in DIPG. Several avenues could be investigated as further work. Firstly, developing a treatment regimen that balances efficacy with tolerability and a delivery schedule that is optimised to the pharmacokinetic properties of the agents being administered. Thereafter, assessing surrogate measures of treatment effect as well as potential improvements in survival recognising that the latter may require several experimental iterations. I hypothesise that a combination drug regimen of doxorubicin and niraparib administered with MRgFUS in a repeated fashion would result in a statistically significant improvement in survival of SU-DIPG XVII mice.

In conclusion, in this study I have demonstrated the pre-clinical feasibility of brainstem BBB disruption using MRgFUS. I have also demonstrated the potential for increased and focal drug delivery to the brainstem. Now that the main molecular genetic drivers of DIPG are known, there is also a need for rational targeting of these tumours with highly specific pathway inhibitors. It is my hope that MRgFUS may play an important role in overcoming the BBB and providing a safe and reliable drug delivery strategy for the future treatment of DIPG.

Rather excitingly, the work in this study has been used to support an application for a phase I/II clinical trial protocol for MRgFUS mediated doxorubicin delivery to patients with DIPG at The Hospital for Sick Children, Toronto, Canada. The protocol is currently in the final stages of review at Health Canada

6 Materials and methods

6.1 Cell culture

DIPG cell lines (SU-DIPG-IV, SU-DIPG-VI, SU-DIPG-XIII, SU-DIPG-XVII, SU-DIPG-XXXVI) were generously provided by Dr. Michelle Monje (Stanford University, Stanford, CA). Cells were propagated in a medium formulation designated as Tumour Stem Base medium (TSM Base) in which growth factors were added immediately prior to cell feeding and/or passage. TSM Base consisted of 50% Neurobasal-A medium (Invitrogen – 10888-022), 50% Dulbecco's Modified Eagle's Medium/Nutrient Mixture F12 (Invitrogen – 11330-032), 10mM HEPES (Invitrogen – 15630-080), 1mM MEM Sodium Pyruvate Solution (Invitrogen – 11360-070), 100μM MEM Non Essential Amino Acids (Invitrogen – 11140-050), 1X GlutaMAX-I Supplement (Invitrogen – 35050-061) and 1X Antibiotic-Antimycotic (Invitrogen – 15240-096). The solution was filter-sterilized by negative pressure through a 0.2μm membrane. Complete tumour stem medium (TSM) consisted of TSM Base supplemented with 1X B-27 Supplement minus vitamin A (Invitrogen – 12587-010), 20ng/mL human recombinant epidermal growth factor (Shenandoah Biotech – 100-26), 20ng/mL human recombinant fibroblast growth factor basic-154 (Shenandoah Biotech – 100-146), 10ng/mL human recombinant platelet derived growth factor AA, 10ng/mL human recombinant platelet derived growth factor BB and 2ug/mL Heparin (StemCell Technologies Inc. – 07980). For expansion and passaging, 3 million cells were seeded per T75 tissue culture flask in 20mL of TSM, and re-seeded at differing intervals for each specific cell line dependent upon their growth rates. SU-DIPG IV, XIII and XVII were grown in surface-treated flasks (Thermo-Fisher–156499), while SU-DIPG VI lines were grown in

suspension flasks (ThermoFisher – 156800) due to their neurosphere growth configuration. All cell lines were maintained at 37°C in a 5% CO_2 humidified incubator.

6.1.1 Cell Passage

T75 tissue culture flasks containing an SU-DIPG cell line and TSM were decanted using a 25mL pipette into a 50mL conical tube. 7mL of TrypLE Express (Invitrogen – 12604-039) supplemented with 70µL Deoxyribonuclease I (Worthington – LS002007) was added to the flask and incubated at 37°C for 5 minutes. Meanwhile, cells in the conical tube were pelleted via centrifugation at 300g for 5 minutes. The supernatant (old medium) was then transferred to a fresh 50mL conical tube whilst preserving the cell pellet. The flask containing TrypLE was then removed from the incubator, triturated, and its contents were transferred to the conical tube containing the cell pellet. The pellet was triturated in the TrypLE solution. A further 5mL of TrypLE Express and 50uL of Deoxyribonuclease I were added to the flask, triturated, and the volume was transferred to the conical tube. The tube was nutated at 37°C for 5 minutes, followed by another round of trituration to fully dissociate the cells. 22mL of pre-warmed Hank's Balanced Salt Solution (HBSS, Fisher – MT21022CV) was added to the cell mixture, from which a 500µL sample was collected for cell counting. The cells were pelleted via centrifugation at 300g for 7 minutes, after which the supernatant was discarded. The pellet was then resuspended in a 1:1 mixture of fresh TSM and conditioned TSM (old media), and cells were subcultured at 3 million cells per T75 flask.

6.1.2 SU-DIPG cell line validation by DNA fingerprinting

SU-DIPG cell pellets were collected following passage and placed in a microcentrifuge tube. 500µL of lysis buffer (10mM Tris-Cl, 0.1M EDTA and 0.5% SDS) and 10µL Proteinase K (ThermoFisher – EO0491) were added to the mixture, which was vortexed and then

incubated overnight in a 55°C thermomixer. The next day, the solution was cooled to room temperature, and 500μL phenol was added to the tube. The sample was emulsified by inversion and left to incubate for 5 minutes, after which the tube was centrifuged at 10000g for 10 minutes at room temperature. The aqueous phase of the sample was then transferred to a new microcentrifuge tube containing 500uL phenol. The sample was again inverted to create an emulsion, incubated, and centrifuged at 10000g for 10 minutes. Phase lock gel 1.5mL heavy tubes (ThermoFisher – A33248) were prepared by centrifugation for 30 seconds at 12000g and 500uL phenol-chloroform-isoamyl alcohol was added to each tube. The aqueous phase of the sample was placed in the phase lock gel tubes and inverted to create an emulsion. The samples were then centrifuged at 12000g for 5 minutes at room temperature. The aqueous phase was again transferred to a new microcentrifuge tube, to which 1mL 100% ethanol and 100uL ammonium acetate were added, and the tube was mixed by inversion. The sample was centrifuged for 10 minutes at room temperature. The supernatant was removed, and the pellet was washed in 1mL 75% ethanol, followed by a 5-minute centrifugation. This wash step was repeated. The ethanol was then removed, and the pellet was stored in an open tube to remove any trace of ethanol by evaporation. 20μL of sterile water was added to the pellet and triturated. DNA concentration was determined via absorbance at 260nm using a Nanodrop 8000 Spectrophotometer (Thermo Scientific). A 10μL sample at 10ng/μL concentration was provided to the DNA sequencing facility at The Centre for Applied Genomics, SickKids Research Institute. The resultant DNA fingerprint was compared to that provided by the Monje Lab, from which the cell lines were obtained **(Table 2 and 3 - Appendix)**. A threshold of 80% was used as a quality control metric[272].

6.1.3 Confirmation of H3 mutation in SU-DIPG cell lines

Western Blotting

Cultures of DIPG cells were washed twice with PBS, and lysed in either 500µL RIPA buffer containing protease inhibitor cocktail (Roche 11836153001) at 4°C for 20 minutes, or using the Epiquick Total Histone Extraction Kit (EpiGentek OP-0006-100). The lysates were collected by scraping and centrifuged at 18000g for 5 minutes. The supernatants were collected, and protein concentration was measured in triplicate in 96 well format using the bicinchoninic acid (BCA) assay (Thermo Scientific 23227). 40µg of protein lysate was loaded into each well of a 5-20% gradient tris-glycine SDS polyacrylamide gel. A directional current was applied to the gels at a constant 30mA for 1.5 hours, followed by a constant 120V for 1.5 hours. Polyvinylidene difluoride (PVDF) membranes with 0.45µm pore size were activated in 100% Methanol for 10 minutes. The proteins were transferred from the gels to the PVDF membranes using a Trans-Blot electrophoretic transfer cell apparatus (Bio-Rad 1703930) in tris-glycine transfer buffer (250mM tris, 1.9M glycine, 10% methanol) at constant 120V for 1 hour. Two PVDF membranes were stacked together to ensure capture of the low-molecular weight histones. Upon completion, membranes were stained with 0.1% Ponceau S to confirm protein transfer, followed by 4 washes with TBS-T (20mM Tris-Cl, 150mM NaCl, 0.1% Tween 20). Membranes were blocked for 1 hour in 5% skim milk (Bioshop-SKI400) in TBS-T at room temperature on a rotator. Subsequently, membranes were probed using antibodies against human histone H3 (mutated K27M) protein (15kDa, Abcam ab190631, 1:1000) and β-Actin (45kDa, Cell Signaling #4970, 1:1000) in block buffer, overnight at 4°C with gentle agitation. Membranes were then washed three times in TBS-T, and incubated with horseradish peroxidase-conjugated anti-rabbit IgG (1:10000, Cell Signalling #7074) in blocking solution for 1 hour at room

temperature   on   a   rotator.

Following incubation, membranes were washed in three times with TBS-T, and visualized

on a ChemiDoc XR system (Bio-Rad) using enhanced chemiluminescence substrate

(PerkinElmer NEL105001EA) as per manufacturer's instructions **(Fig. SF 3 – Appendix)**

6.2 Z-Scoring SU-DIPG Cell lines in 384 or 96 well format

Each SU-DIPG cell line was plated at various densities (1000, 2000 and 4000 cells per well)

in 40uL of the corresponding Working Tumour Stem Medium in a 384 well or 96 well

format using a Thermos Multidrop Combi nL Reagent Dispenser (Thermofisher-580400)

24 hours prior to dosing with the D300e digital dispenser (TECAN). 1uM staurosporin and

equivalent volume of DMSO were dispensed at various points across the plate to facilitate

z-scoring calculation. A twelve-point dose range (2nM – 1uM) of staurosporine was also

dispensed in the upper left quadrant, middle quadrant and lower right quadrant. Viability

was assessed 96 hours after dosing using Alamar Blue® Cell Viability Reagent

(ThermoFischer Scientific, Canada) via the Thermo Multidrop, and 3 hours of incubation.

Optical absorbance values at 550nm-590nm from each well were measured using a plate

reader (Spectra Max Gemini EM).

6.2.1 Drug Screen

Eight conventional chemotherapy agents were selected from prior published *in

vitro* efficacy in either DIPG or paediatric high-grade glioma cell lines[81,273]. Each DIPG cell

line (SU-DIPG IV, SU-DIPG XIII and SU-DIPG XVII) was plated into a 384 well or 96 well plate

(containing the chemotherapy agents) using the Thermo Multidrop (ThermoFischer

Scientific, Canada) at 4000 cells per well SU DIPG IV, VI and XVII) or 8000 cells per well (SU-

DIPG XIII) and placed in an incubator overnight. At 24 hours, the HP-300 Digital Drug

Dispenser was used to enable automated and accurate dispensing of drugs in a 384 or 96 well format. For each compound, a twelve-point dose range, customised from previously published IC50 data **(Fig. 10A)**, was dispensed in a scrambled format to reduce plating artefacts. Viability was assessed at 96 hours. Alamar Blue® Cell Viability Reagent (ThermoFischer Scientific, Canada) was added to each well, again using the Thermo Multidrop, and incubated for 3 hr. Optical absorbance values at 550nm-590nm from each well were measured using a plate reader (Spectra Max Gemini EM). Percent cell viability at each drug concentration was determined relative to vehicle control (DMSO) and IC50 values were calculated in excel using the XLfit Plugin (IDBS) or GraphPad Prism version 9 (California, USA) with the Boltzmann sigmoidal curve fitting algorithm. At least three replications were conducted for each cell line.

Following identification of doxorubicin as a favourable chemotherapy agent *in vitro*, ten newer molecular therapies classified as either HDAC inhibitors (Panobinostat, entinosta, vorinostat), PARP inhibitors (Olaparib, niraparib and talazoparib) or tyrosine kinase inhibitors (masitinib, avapritinib, crenolanib, nintedanib) were screened based upon their mechanistic action, prior published efficacy in DIPG cell lines and potential for synergistic effect with doxorubicin.

6.3 Zero interaction potency (ZIP) synergy analysis

To assess drug synergy, SU-DIPG cell lines were plated at a previously optimised plating density (see above) in a 50uL volume of Working Tumour Stem medium in a 96 well format using a thermos multidrop 24 hours prior to dosing. A 10-point dose range was delivered for each drug alone, or in combination with a second drug at each concentration of the 10-point dose range in a checkerboard format. Viability was assessed at 4 days after the addition of Alamar Blue® Cell Viability Reagent for 3 hours using a plate reader as

previously described (Spectra Max Gemini EM). Percent viable cells at each concentration of drug alone or with drug combinations was determined relative to vehicle control (DMSO).

The resultant data was uploaded into the SynergyFinder web application version 2.0 in table format and synergy analysis was conducted using the zero interaction potency (ZIP) method[218]. Subsequent output files were exported in PDF format.

6.4 Magnetic Resonance guided Focused Ultrasound of the Brainstem

6.4.1 Animals

The use of animals and all animal procedures was approved by the Animal Care Committee at Sunnybrook Health Sciences Centre. All protocols used were in accordance with the guidelines established by the Canadian Council on animal care and the Animals for Research Act of Ontario, Canada.

For experiments pertaining to the safety of MRgFUS in the brainstem, female Sprague Dawley rats (Jackson Laboratory) were used, weighing 150 – 250g at the start of each experiment. For experiments assessing Doxorubicin delivery to the brainstem, female NOD/SCID/GAMMA (NSG) mice (20 – 25g, Jackson Laboratory) were used. All animals were housed at constant temperature (23 ± 1°C) and relative humidity (60 ± 5%) with free access to food and water and a fixed 12-h light/dark cycle.

6.4.2 Brainstem BBB disruption in Sprague Dawley Rats

Forty-two female Sprague Dawley rats (weight 150 – 250g) were anaesthetised using inhaled isoflurane anaesthesia in an animal chamber prior to repositioning in a nose-cone. Hair over the dorsal aspect of the skull was shaved and further removed with depilatory cream. A 22g angio-catheter was inserted into the tail vein. The animal was placed and secured in a supine position, on a mount designed for targeted focused

ultrasound delivery. Registration of the animal's position within the mount was conducted with a 7T MRI scanner (BioSpin 7030; Bruker, Billerica, Mass). The exposed scalp was positioned on the water pack portion of the mount with ultrasound gel used between the 2 surfaces to achieve acoustic wave coupling. Initial T2 and T1 weighted axial and sagittal images were performed and used to set right and left sided brainstem targets. Following imaging and registration, the mount and attached animal were returned to the focused ultrasound system. The water pack portion of the mount was positioned to overlie a chamber of degassed, deionized water containing the transducer[274].

An in-house-built three-axis focused ultrasound system was used. Ultrasound was generated using a 1.68MHz spherically-focused transducer (radius of curvature = 60mm, external diameter = 75mm, focal number 0.8). The transducer was driven by a function generator (33220A; Agilent Technologies, Santa Clara, CA) and a radiofrequency amplifier (NP2519; NP Technology, Newbury Park, CA). Each transcranial sonication consisted of 10-millisecond bursts at a 1-Hz pulse repetition frequency for a total of 2 minutes. Microbubbles (uBs) (Definity® Lantheus Medical Imaging, Inc., N. Billerica, MA, U.S.A) were diluted 1:10 in normal saline and administered intravenously (0.02mL/kg) at the onset of sonication. Microbubble emissions were detected during sonication by a custom built polyvinylidene difluoride hydrophone[275] connected to a scope card located in the controlling PC. Pressure amplitude was incremented after each burst (starting pressure 0.25, pressure increments of 0.025) until sub or ultraharmonic emissions were detected in the fast fourier transform, (FFT) of the captured hydrophone signal by the PC. The remainder of the sonication proceeded at 50% of this threshold pressure amplitude. This sonication protocol has been devised to ensure effective and replicable BBB opening without tissue injury[187].

A region consisting of a 4-point overlapping grid was treated in the right side of the pons and then repeated on the left side of the pons (**Fig. 1A**). The same dose of uBs was injected at the onset of the left sided sonication. Hence, the total uB dose delivered was 2 x 20uLkg. It should be noted that this is twice the clinically advised maximum dose of Definity microbubbles as an ultrasound contrast agent. The two regions were sonicated at least five minutes apart to allow clearance of μBs from the initial injection (microbubble half-life ≈ 5-7 minutes in Sprague Dawley rats)[276]. Rodents allocated to the μB control group received the same intravenous doses of μBs and gadolinium contrast but not the delivery of focused ultrasound. They were however positioned in the FUS mount for the same duration of time as the treated animals. Rats allocated to the "MRgFUS" control group did not receive the doses of μBs but focused ultrasound and gadolinium contrast were administered at consistent time points as in the treated groups. Pre- and post-procedure imaging sequences were the same across all groups. Rats randomised to the "MRgFUS + μB + Cisplatin" group received an intravenous bolus dose of cisplatin (1.5 mg/kg) during the first (right sided) sonication delivered.

6.4.3 Intraprocedural physiological monitoring

An MRI compatible foot sensor of the MouseOx Plus physiological monitor (Starr Life Sciences Corp, Oakmont, USA) was attached to the left hind paw of the rat. Signal confirmation was achieved and physiological monitoring and recording of heart and respiratory rate was initiated. Duration of monitoring extended from at least 4 minutes prior to initial right sided brainstem sonication and completed at least 4 minutes after left sided brainstem sonication. The timing of interventions was documented to later cross reference with the monitoring data. Data extracted was plotted and graphed using Graphpad Prism version 7 (California, USA).

6.4.4 Brainstem BBB Disruption in NSG Mice

Sixteen female NSG mice (20 – 25g) were anaesthetised and prepared for MRgFUS delivery as above. A smaller 26 G catheter was used for tail vein catheterisation and a single 4-point overlapping grid was treated in the centre of the pons. The smaller cross-sectional area of the brainstem in mice did not necessitate an 8-point treatment regime to achieve coverage. All mice were intravenously administered 5mg/kg of Doxorubicin (Cat. No. S1208, Selleckchem) at the time of MRgFUS delivery, immediately following the intravenous administration of microbubbles. Five mice were randomly allocated to each group. Groups were; 1) "No intervention" – mice received no focused ultrasound intervention. Mice were placed on the focused ultrasound device for the same period of time and administered gadolinium contrast at the same dose and time points as mice receiving interventions 2) "MRgFUS" – control group receiving focused ultrasound delivery without intravenously administered microbubbles, 3) μB – control group receiving μBs without focused ultrasound energy and 4) "MRgFUS + μB" – treatment group receiving both focused ultrasound energy and intravenously administered μBs.

6.5 Assessment of BBB Disruption

6.5.1 Contrast enhanced T1 weighted Magnetic Resonance Imaging

Contrast enhanced (0.1ml/kg Gadovist; Bayer HealthCare Pharmaceuticals, Inc. Leverkusen, Germany) T1 weighted imaging was used to assess BBB disruption after focused ultrasound delivery. The contrast agent was delivered after the left sided brainstem sonication in rats and at the time of the single brainstem sonication in mice. This was four minutes prior to imaging. Images were extracted using the MIPAV (Medical Image Processing, Analysis and Visualization) application.

6.5.2 Evans Blue administration

A 4% Evans Blue dye was intravenously injected (4ml/kg) into a cohort of rats (n=5 for each group; "MRgFUS", "µB" and "MRgFUS + µB" and n = 4 for the "Control" group). following the post procedure contrast enhanced MR imaging. Control rats received no intervention. Animals were maintained under anaesthesia using intramuscularly injected ketamine (100mg/ml Narketan; Vetoquinol, Toronto, at a dose of 100mg/kg) and xylazine (20mg/ml Rompun; Sigma-Aldrich, Toronto, 10mg/kg dose). Animals were euthanised at one hour after Evans Blue administration. They were deeply anaesthetised and transcardially perfused with 4% paraformaldehyde. Sectioning through the level of the pons was performed and images were taken using a dissecting microscope (Olympus SZX16).

6.6 Assessment of Motor Function

6.6.1 Rotarod Testing

Rats were briefly pre-trained on an automated 4 lane rotarod unit (Rota Rod RS, Letica Scientific Instruments, Panlab Harvard Apparatus) initially on a fixed speed setting. An accelerating protocol was then used whereby rats were placed on a rod that accelerated smoothly from 4 to 40rpm over a period of 1 minute. The length of time that each animal was able to stay on the rod was recorded as the latency to fall, registered automatically by a trip switch under the floor of each rotating drum. Five successive recordings were taken for each rat (with 5-minute rest intervals between each trial) on five consecutive mornings one week prior and one week post brainstem sonication. The rats were not labelled regarding their randomization group and thus the operator conducting post-procedure testing was blinded to the intervention.

6.6.2 Grip Strength Testing

Rat forelimb grip strength was measured using an electronic digital force gauge grip-strength meter with accompanying grid fixture (Bioseb Instruments, Pinellas Park, Florida, USA). Rats were placed onto the grid, allowing forelimbs to take grip. Rats were drawn back in a straight line away from the sensor until they eventually released their grip. The peak force (g) exerted by the animal's grip was recorded. Eight trials were conducted (with 5-minute rest intervals between each trial), on three alternate days, one week prior to and one week post brainstem sonication. A single operator was used for all grip strength recordings to reduce operator variability and was also blinded to the intervention.

6.7 Liquid Chromatography-Tandem Mass Spectrometry (LC/MS/MS)

NSG mice were anaesthetised two hours following intravenous Doxorubicin delivery using intramuscularly injected ketamine (100mg/ml Narketan; Vetoquinol, Toronto, at a dose of 100mg/kg) and xylazine (20mg/ml Rompun; Sigma-Aldrich, Toronto, 10mg/kg dose). Once deeply anaesthetised, mice were transcardially perfused with 0.9% sodium chloride solution for seven minutes and then euthanised. Brains were extracted and divided into the cerebrum, cerebellum and brainstem, placed in individually labelled cryotubes and snap frozen in liquid nitrogen. Samples were stored at -80° C until analysis was conducted.

Samples were analysed by LC/MS/MS at the Analytical Facility for Bioactive Molecules (The Hospital for Sick Children, Toronto, Canada). Sample preparation was carried out under reduced light conditions and cold temperature (4°C) using only plasticware. Working solutions of daunorucin (0.2 µg/mL) and doxorubicin standard curve (nine points prepared by serial dilutions, ranging from 5 to 2500 ng/mL) were prepared fresh from 0.1mg/mL stock solutions kept at -80°C.

Frozen samples were weighed and transferred into Precellys homogenization tubes containing ceramic beads (Bertin Technologies, Rockville, Washington DC). Extraction solvent consisting of 60% acetonitrile and 40% 0.05 M ammonium acetate, pH 3.50 (v/v) was added to achieve 10mg/mL and homogenised using a Precellys 24 high-throughput homogenizer (Bertin Technologies, Rockville, Washington DC) - two 20 second bursts at 5500 rpm with a 30 second pause. 100 μL of the homogenised suspension (corresponding to 10 mg tissue) was transferred into a set of 1.5 mL Eppendorf tubes. Ten μL of working daunorubicin was added followed by 100 μL of extraction solvent. Samples were mixed by vortex, kept on ice for ten minutes and centrifuged at 20,000 g for fifteen minutes at 4°C. Supernatants were taken to dryness under N2 gas. Residues were reconstituted in 100 μL of MeOH/H2O (50/50) + 0.1% formic acid, centrifuged at 20,000 g for ten minutes at 4°C and transferred into 200 μL plastic inserts for LC/MS/MS analysis. Doxorubicin and daunorubicin were measured by LC/MS/MS using a QTRAP 5500 triple-quadruple mass spectrometer (Sciex: Framingham, Massachusetts, USA) in positive electrospray ionization mode by MRM data acquisition with an Agilent 1200 HPLC (Agilent Technologies: Santa Clara, California, USA). Chromatography was performed by automated injection of 3 μL on a Kinetex XB C18 column, 50 x 3 mm, 2.6 μm particle size (Phenomenex, Torrance, CA). The HPLC flow was maintained at 600 μL/minute with a gradient consisting of: A= Water + 0.1% Formic Acid and B = Acetonitrile + 0.1% Formic Acid. Total run time was 5 minutes.

Quantification was performed on Analyst 1.6.1 software (ABSciex: Framingham, Massachusetts, USA) by plotting the sample peak area ratios (analyte peak area/internal standard peak area) of doxorubicin against a standard curve generated from various concentrations of doxorubicin from 0.01 ng to 10 ng, spiked with the same amount of

daunorubicin used for the samples and extracted in the same conditions. The use of daunorubicin as an internal standard is due to its structural similarity to doxorubicin and therefore similar extraction recovery and chromatographic properties[277,278].

6.8 Histological analysis of MRgFUS treated rodent brainstems

6.8.1 Tissue preparation

Rats randomised to the "early" histology group (n = 3 per group) were euthanised 4 hours following their allocated intervention. The "late" histology group (n = 6 per group) were euthanised on day 14 post intervention, allowing for post procedure grip strength and rotarod testing. These time points were chosen to maximise the potential of capturing apoptosis which could arise in either an acute or delayed fashion. Furthermore, assessment of neuronal number following MRgFUS has previously been measured at 8 days following intervention[187]. A cohort (n = 5) of untreated rats were sacrificed to provide negative control tissue. Brains were extracted and stored in 10% neutral buffered formalin. Fixed tissues were dehydrated and embedded in paraffin. Brains were axially sectioned in three regions of the brainstem.

6.8.2 Haematoxylin and Eosin staining

Five μm thick axial sections were cut and mounted onto slides and deparaffinised using xylene, rehydrated and incubated in Hematoxylin (Gills Formula, Vector labs, Burlingame, CA) for 5 minutes. Sections were then washed in tap water for 5 minutes and incubated in Eosin Y (0.5% solution, Fisher Scientific) for 3 minutes, dehydrated and permounted with Permount (Fisher Scientific). H&E stained sections were independently reviewed by a veterinary pathologist who was blinded to the sample labels.

6.8.3 Immunohistochemistry

Prior to immunostaining, 5µm thick paraffin sections were deparaffinized, rehydrated, and pretreated in citrate buffer, pH 6.0 for 1 minutes. Sections were blocked in 10% goat serum and incubated in primary antibodies for 1 hour at room temperature: NeuN (Abcam, 1:1000) and cleaved caspase 3 (cell signalling, 1:100) to evaluate neuronal integrity and apoptosis respectively. After three washes, biotinylated secondary antibody 1:100 (Vector Labs – PK – 6102) was applied for 30 minutes at room temperature and incubated in the Avidin-Biotin detection system for 40 minutes at room temperature. After three washes, signal was detected using DAB (Vector Labs-SK4100), counterstained in Hematoxylin (Vector Labs-H3-401) and mounted on slides in Permount (Vector Labs-H-5000). Sections were imaged using a 3D Histech Panoramic 250 slide scanner. Quantification of staining was performed using the Quantification Centre (QC) feature of the Panoramic Viewer software application (3DHistech, Budapest, Hungary) which uses a colorimetric algorithm to calculate the percentage of positive pixels over a designated tissue area, defined as relative mask area (rMA). A protocol was created in the "histology" sub-feature and the brainstem was outlined in each sample as the region of interest.

6.9 Statistical Analysis

6.9.1 Sprague Dawley Rats

Rotarod and grip strength data were analysed using a two-way mixed multivariate analysis of variance (MANOVA) with Tukey's post hoc test. Histology data was compared using a three-way MANOVA with Tukey's post-hoc test. Significance was deemed an alpha level of $P < 0.05$ (*) or $P < 0.01$ (**) with a 95% confidence interval.

Physiological monitoring of heart and respiratory rate were analysed using a two-way multivariate mixed model analysis of variance.

6.9.2 NSG Mice

Doxorubicin quantities between treatments and across brain regions (cerebrum, brainstem and cerebellum) by two-way mixed ANOVA. Significance levels were either $P < 0.05$ (*), $P < 0.01$ (**) or $P < 0.001$ (***) with a 95% confidence interval. A two-way mixed ANOVA was used to compare doxorubicin quantities across brain regions.

6.10 DIPG Mouse Models

The use of animals and all animal procedures were approved by the Institutional Animal Care and Use Committee at The Centre for Phenogenomics and Sunnybrook Research Institute (Toronto, ON, Canada). All protocols used were in accordance with the guidelines established by the Canadian Council on animal care and the Animals for Research Act of Ontario, Canada.

6.10.1: Breeding strategy for RCAS Nestin-Tva;p53$^{fl/fl}$ Mouse Model

Nestin-Tva;p53$^{fl/fl}$ mice have previously been described[279]. Nestin-Tva transgenic mice were purchased (Jackson Laboratory #003529) and intercrossed with p53$^{fl/fl}$ mice generously provided by Dr. Michael Taylor (SickKids Research Institute). Offspring mouse tail biopsies were genotyped and Nestin-Tva;p53$^{fl/wt}$ mice were selected and backcrossed with the p53$^{fl/fl}$ mice. Mouse tail biopsies were again genotyped to select Nestin-Tva;p53$^{fl/fl}$ offspring.

Male Nestin-Tva;p53$^{fl/fl}$ mice were time mated with C57BL/6J females. Pregnant mice were sacrificed by cervical dislocation at embryonic day 14. Embryos were removed, and their hindbrains and hands were harvested. The hand tissues were lysed in 30μL Allele-In-One Lysis Buffer (Allele Biotechnology ABP-PP-MT01500) overnight at 55°C to extract genomic DNA (gDNA). Hindbrains were minced in 1mL of TRIzol reagent (Thermo Fisher 15596026) and subsequently stored at -80°C.

To identify Nestin-Tva transgene positive mice, gDNA extracted from embryonic hands was diluted 1:20, and endpoint PCR was performed using REDExtract-N-Amp PCR ReadyMix kit (Sigma Aldrich R4775). The following primers were used: Tva forward 5'-CAGATTTGAGAGCTCATGTCCA-3', Tva reverse 5'-ACGGACAACGGCACAGAG-3', control forward 5'-CTAGGCCACAGAATTGAAAGATCT-3', control reverse 5'-GTAGGTGGAAATTCTAGCATCATCC-3'. PCR was performed in a thermocycler as per the following protocol: Initial denaturation for 10 minutes at 94°C, followed by 35 cycles of 1 minute at 94°C, 45 seconds at 58°C and 1 minute at 72°C, followed by a final extension step of 5 minutes at 72°C. Reaction products were subject to electrophoresis on a 1% agarose gel and visualized using RedSafe dye (FroggaBio 21141) on a UV transilluminator. Positive mice were expected to show an amplicon of 191bp.

To validate Tva expression, hindbrains in Trizol from transgene-positive mice were thawed on ice. 0.2mL of chloroform was added and tubes were mixed vigorously for 15 seconds. Samples were incubated at room temperature for 1 minute and then centrifuged at 12000g for 15 minutes at 4°C. 400μL of the colourless upper phase was transferred to a correspondingly labelled RNase free tube. An equal volume of 70% ethanol was added to obtain a final ethanol concentration of 35%. Samples were vortexed, and 400μL from each tube was transferred to a PureLink RNA mini prep cartridge (Thermo Fisher 12183018A). Samples were centrifuged at 2000 x g for 15 seconds at room temperature and the flow through was then discarded. This was repeated with a further 400uL of sample. 700uL of Wash Buffer 1 was added to the spin cartridge, which was then centrifuged at 12,000 x g for 15 seconds at room temperature. The flow through was discarded, and the spin cartridge was transferred to a new tube. 500uL of Wash Buffer 2 with ethanol was added to the spin cartridge, which was centrifuged at 12,000 x g for 15

seconds at room temperature. Flow through was discarded and the spin cartridge was replaced into the same collection tube. Addition of Wash Buffer 2 and centrifugation was repeated. The spin cartridge and collection tube were centrifuged again at 12,000 x g for 2 minutes at room temperature to dry the membranes containing the attached RNA. The spin cartridge was then transferred to a recovery tube. 40µL of RNase-free water was added to the centre of the spin cartridge, which was incubated at room temperature for 1 minute. The samples were centrifuged for 2 minutes at 12000 x g at room temperature, after which the purified RNA in the recovery tube was placed on ice. Total RNA was quantified via absorbance at 260nm on a NanoDrop 8000 spectrophotometer (Thermo Scientific). Samples were diluted to a 100ng/µL concentration. Complementary DNA (cDNA) was generated using a High-Capacity cDNA Reverse Transcription kit (Thermo Fisher #4374966). Quantitative real-time PCR (qRT-PCR) was then performed using PowerUp SYBR Green Master Mix (Thermo Fisher A25778) on a StepOnePlus system (Applied Biosystems). The oligonucleotide primers used to measure Tva receptor expression were: Forward 5'-TCCGGTAACGGTTCTTTGTC-3'; Reverse 5'-GCAGTGATCAGCATCCACAT-3'. The primers against housekeeping gene GAPDH were: Forward 5'-CGGGTTCCTATAAATACGGACTGC-3'; Reverse 5'-CCCAATACGGCCAAATCCGT-3'. The level of Tva expression was measured using the delta-delta cycle threshold (ΔΔCt) method.

Female Nestin-Tva;p53$^{fl/fl}$ mice were time mated with male C57BL/6J mice. Neonatal offspring were sacrificed by decapitation, and their hindbrains and hands were harvested. The hand samples of neonatal progeny were used to identify Tva transgene-positive mice as described above. Similarly, hindbrain samples were used to validate Tva receptor expression. Male and female Nestin-Tva;p53$^{fl/fl}$ breeders who consistently

produced progeny with robust Tva receptor expression were then selected and bred. Subsequent progeny from these breeders received intracranial brainstem injections of RCAS plasmids at postnatal day 2-4.

6.10.2 Genotyping protocols

Genomic DNA was isolated from mouse tail biopsies taken 14 days prior to weaning as described above. PCR was performed using REDExtract-N-Amp PCR ReadyMix kit (Sigma Aldrich R4775) using 100ng of gDNA. The transgenic Nestin-Tva allele was detected using the primers described above. The primers used for the detection of the p53-floxed allele were: forward 5'-GGTTAAACCCAGCTTGACCA-3', reverse 5'-GGAGGCAGAGACAGTTGGAG-3'. Endpoint PCR and gel electrophoresis was carried out as described above. The p53-wildtype allele was expected to produce an amplicon of 270bp, whereas the p53-floxed allele was expected to produce an amplicon of 390bp.

6.10.3 Bacterial transformation and propagation of RCAS vectors

RCAS plasmids (RCAS-Cre, RCAS-PDGFB and RCAS-H3.3K27M) were kindly provided by Dr. Oren Becher at Northwestern University. One Shot Stbl3 Chemically Competent *E. coli* (Thermo Fisher C737303) were thawed on ice. Three 10µl aliquots were then dispensed into microcentrifuge tubes, and 1µl of each RCAS vector was added into its corresponding tube. Vials were incubated on ice for 30 minutes, heat shocked for 45 seconds at 42°C, and then placed back on ice for 2 minutes. 500µL of Terrific Broth (Thermo Fisher A1374301) was added to each vial, which was then placed in a shaking incubator at 37°C for 1 hour at 225 rpm. 100µl from each transformation was streaked on a pre-warmed LB agar plate containing 0.1mg/ml ampicillin. Plates were then inverted and incubated at 37°C overnight.

The next day, using a sterile pipette tip, one isolated bacterial colony from each plate was collected and placed into a correspondingly-labelled test tube containing 5ml Terrific Broth and 0.1mg/ml ampicillin. Tubes were capped loosely and placed in a shaking incubator at 37°C and 225 rpm overnight.

6.10.4 DNA mini-prep of RCAS vectors from Stbl3 bacteria

After the Stbl3 clones transformed with RCAS plasmids were propagated overnight, the bacteria were collected by centrifugation. Plasmid DNA was isolated using a high-speed plasmid miniprep kit (IBI Scientific IB47101) according to manufacturer's instructions. Resultant plasmid DNA eluted in water was quantified using a Nanodrop-8000 Spectrophotometer (Thermo Scientific).

6.10.5 DF-1 Transfection with RCAS plasmids

UMNSAH/DF-1 chicken fibroblast cells were purchased from ATCC (#CRL-12202; Manassas, VA) and cultured in DMEM (Wisent Bioproducts 319-005-CL) supplemented with 10% heat-inactivated foetal bovine serum (Wisent Bioproducts 080-450), 100 units/mL penicillin, and 100μg/mL streptomycin, at 39°C and 5% CO_2 on surface-treated culture vessels. One day prior to transfection, cells were subcultured at a ratio of 1:12. Cells were transfected with RCAS plasmids (RCAS-PDGF-B, RCAS-Cre, and RCAS-H3.3WT or RCAS-H3.3K27M) using X-tremeGENE 9 DNA Transfection Reagent (Sigma-Aldrich 6365787001) according to manufacturer's instructions. Transfection efficiency was confirmed via GFP expression. Following transfection, the cells underwent a minimum of 6 passages prior to being used for *in vivo* experiments in order to ensure sufficient RCAS viral load.

6.10.6 Brainstem injection of DF-1 clones

Stable DF-1 clones expressing RCAS-PDGF-B, RCAS-Cre and RCAS-H3.3K27M were combined at a 1:1:1 ratio and 1ul of the cell suspension (300,000 cells/uL in PBS) was injected into the brainstem of postnatal day 2-4 Nestin-Tva; p53$^{fl/fl}$ mice. Brainstem co-ordinates used were midline, 3mm posterior to the lambdoid suture and 3mm deep. Following tumour induction, mice were monitored for general health during recovery. Mice were euthanized by CO_2 inhalation when signs of tumour burden were evident or experimental endpoint (20% of body weight loss or deterioration of condition) was reached. Brains were dissected and fixed in 10% neutral buffered formalin for 48h and embedded in paraffin blocks (FFPE). Sections were stained with haematoxylin and eosin (HE) to examine pathological features.

6.10.7 SU-DIPG XVII Xenograft Model

NOD scid gamma (NSG) mice between 6 and 11 weeks of age were anaesthetized with 4% isoflurane and administered meloxicam analgesic (2mg/kg). Their heads were immobilised on a pre warmed stereotactic frame (Stoelting Co), after which a skin incision and 0.5mm craniotomy were performed at 0.8mm posterior and 0.8mm right of the lambdoid suture. A 32G syringe (Hamilton Company) was used to dispense 1uL of an SU-DIPG XVII cell suspension (300,000 cells/uL in PBS) into the brainstem at a depth of 5mm below the surface of the skull.

6.11 MR Imaging in DIPG mouse models

SU-DIPG XVII xenografted mice were imaged at 100 and 170 days post tumour induction. DIPG mice generated with the RCAS system were imaged 35 days after DF-1 cell injection. Animals were anaesthetised using isoflurane. A 26G angio-catheter was inserted into the tail vein. Mice were immobilised in a supine position on a custom MR compatible

sled. T1 and T2 weighted FSE images were acquired with a 7T MRI scanner (Biospin 7030; Bruker). Gadolinium contrast agent (Gadovist; 0.1ml/kg; Bayer Healthcare Pharmaceuticals) was administered intravenously by bolus infusion through the tail vein catheter and a repeat T1 weighted image was obtained for tumour detection.

6.12 Doxorubicin administration in SU-DIP XVII mice and NSG mice

In a subset of SU-DIPG XVII mice and NSG mice, IV doxorubicin (Selleck Chemicals) at a dose of 5mg/kg was administered IV via tail vein. Mice were anaesthetised two hours following intravenous Doxorubicin delivery using intramuscularly injected ketamine (100mg/ml Narketan; Vetoquinol, Toronto, at a dose of 100mg/kg) and xylazine (20mg/ml Rompun; Sigma-Aldrich, Toronto, 10mg/kg dose). Once deeply anaesthetised, mice were transcardially perfused with 0.9% sodium chloride solution for seven minutes and then euthanised. The collected blood was fractionated to isolate plasma, and the brainstems were removed. The plasma and tissues were snap-frozen and stored at -80° for LC-MS/MS analysis. Samples were analysed by LC-MS/MS at the Analytical Facility of Bioactive Molecules (The Hospital for Sick Children, Toronto) as previously described.

6.13 Histological analysis of DIPG mouse models

6.13.1 Tissue preparation

Following tumour induction, mice were monitored for general health during recovery. Mice were euthanized by CO_2 inhalation when signs of tumour burden were evident or experimental endpoint (20% of body weight loss or deterioration of condition) was reached. Brains were dissected and fixed in 10% neutral buffered formalin for 48h and embedded in paraffin blocks (FFPE). Sections were stained with haematoxylin and eosin (HE) to examine pathological features.

6.13.2 Immunohistochemistry

Once tissues were processed into FFPE blocks, 5 µm thick sections were cut and deparaffinized, rehydrated, and pretreated in citrate buffer (pH 6.0) for 15 min. These were blocked in 10% goat serum and incubated for 1 h at room temperature in one of the following primary antibodies: rabbit anti-Ki-67 (CRM325A; Biocare Medical), mouse anti-Nestin (556309; BD Biosciences), mouse anti-p53 (sc-126; Santa Cruz), rabbit anti-H3K27me3 (9733; Cell Signaling). After three washes, biotinylated secondary antibody 1:100 (ABC kit, Vector Labs) was applied for30 min at room temperature, and then incubated for 40 min at room temperature in the Avidin-Biotin detection system. After three washes, signal was detected using DAB, counterstained with hematoxylin, and mounted using Permount (Thermo Fisher Scientific). Whole slide images were captured with a Panoramic Flash II slide scanner (3DHistech).

6.14 Kaplan-Meier Survival Analysis of DIPG mouse models

Seven mice in each cohort were used to assess survival from the time of intracranial injection. Age-matched, xenograft-naïve Nestin-Tva;p53$^{fl/fl}$ and NSG mice were respectively used as controls for the RCAS GEMM and SU-DIPG-XVII xenograft models. Survival was analysed via the Kaplan-Meier estimate using either the log-rank or Grehan-Breslow-Wilcoxon test (p<0.05). Statistical analyses were conducted using Prism 9.0 (GraphPad Software, California, USA).

Appendix
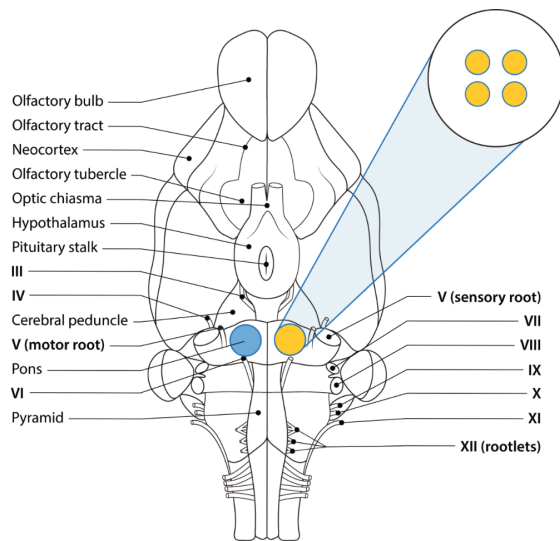
Figure SF 1: Brainstem sonication schema used in Sprague Dawley rats. MRgFUS was delivered to a region comprising a four-point overlapping grid in each half of the pons.
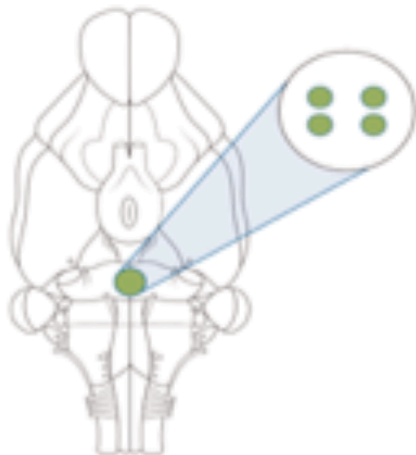
Figure SF 2: Brainstem sonication schema used in NSG Mice. MRgFUS was delivered to a region comprising of a four-point overlapping grid in the centre of the pons.
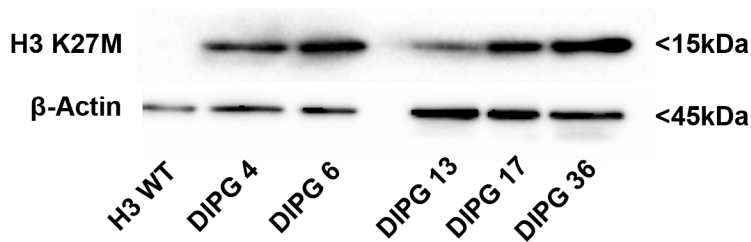
Figure SF 3: Western blot in SU-DIPG cell lines: Western blot to confirm the presence of the H3K27M mutation in DIPG cell lines used in this study.

	AMEL	CSF1PO1	D13S317	D16S539	D21S11	D5S818	D7S820	TH01	TPOX	vWA
SU-DIPG IV	X/X	9/10	7/12	9/12	29/31	12/13	10/11	6/9.3	8/	15/19
SU-DIPG VI	X/X	10/11	11/	8/13	29/31	10/12	8/9	7/8	8/11	17/18
SU-DIPG XIII	X/X	9/10	11/12	11/12	30/31	12/12	9/9	6/7	7/8	13/18
SU-DIPG XVII	X/Y	13/13	9/9	9/12	28/29	11/11	8/9	7/7	8/11	18/19

Table 2: Short Tandem Repeat (STR) DNA profiling of human DIPG cell lines. Results obtained from the Monje lab on transfer of cell lines.

	AMEL	CSF1PO1	D13S317	D16S539	D21S11	D5S818	D7S820	TH01	TPOX	vWA
SU-DIPG IV	X/X	9/10	7/12	9/9	29/31	12/13	10/11	6/903	8/8	15/19
SU-DIPG VI	X/X	10/11	11/	8/13	28/29	10/12	8/9	7/7	8/11	15/19
SU-DIPG XIII	X/X	9/10	11/12	11/12	30/31	11/12	9/10	6/9	7/8	13/18
SU-DIPG XVII	X/Y	13/13	9/9	9/12	28/29	11/11	8/9	7/7	8/11	18/19

Table 3: Short Tandem Repeat (STR) DNA profiling of human DIPG cell lines. Results obtained from cell lines prior to research paper publication. Differences are highlighted in red and each cell line is shown to have a $\geq$80% match with its original.

List of Abbreviations

μB	microbubbles
μL	microlitre
μM	micromolar
ACNU	nitrosurea, 1-(4-amino-2-methyl pyridimine-5-yl)-methyl-3-(2-chloroethyl)-3-nitrosurea hydrochloride
ACVR1	Activin A Receptor Type 1
ADP	Adenosine diphosphate
AKT	Ak strain transforming
ALK2	Activin receptor-like kinase-2
ANOVA	Analysis of variance
ATM	Ataxia telangiectasia mutated
ATP	Adenosine triphosphate
ATRX	α-thalassemia/mental retardation syndrome X-linked
BBB	Blood Brain Barrier
BCNU	bis-chloro-ethyl nitrosurea
BMP	Bone Morphogenic Protein
BPM	Beats per minute
CAF1	Chromatin Assembly Factor 1
CD6	Cyclin-dependent kinase 6
CDKN2A	Cyclin-dependent kinase inhibitor 2A
cDNA	Complementary DNA
CED	Convection Enhanced Delivery
CHK1	Checkpoint kinase 1
Cis	Cisplatin
CNS	Central Nervous System
Cre	Cyclic recombinase
CSF	Cerebrospinal Fluid
CT	Computed Tomography
Cys-A	Cyclosporin A

Da	Dalton
DAB	3,3'- Diaminobenzidine
DAXX	Death-domain associated protein
DF-1	Chicken embryo fibroblast cell line
DIPG	Diffuse Intrinsic Pontine Glioma
DNA	Deoxyribonucleic Acid
DSB	Double stranded breaks
EC50	Half maximal effective concentration
ECS	Extracellular space
EDTA	Ethylenediamine tetraacetic acid
EGFR	Epidermal Growth Factor Receptor
ERK	Extracellular signal-regulated kinases
EZH1/2	Enhancer of Zeste Homologue 1 or 2
FDA	US Food and Drug Administration
FFPE	Formalin Fixed Paraffin Embedded
FKBP12	FK506-binding protein 12
FLAIR	Fluid-attenuated Inversion Recovery
FOP	Fibrodysplasia ossificans progressive
FUS	Focused ultrasound
Gad	Gadolinium
GBM	Glioblastoma Multiforme
GEMM	Genetically Engineered Mouse Model
GS	Glycine-serine rich domain
H3K27M	Substitution of methionine for lysine 27 of histone H3.3
H3K27me3	Trimethylation of lysine 27 on histone H3 protein
HDAC	Histone Deacetylase
HGG	High Grade Glioma
H&E	Haematoxylin & Eosin
HIRA	Histone cell regulator
IA	Intra-arterial
IC	Intra-carotid
IC40	Half maximal inhibitory concentration

ID	Inhibitors of DNA binding and cell differentiation
Ink4a-ARF	Tumour suppressor proteins, p16(INK4a) and ARF
IP	Intra-peritoneal
IV	Intravenous
JNK	c-Jun N-terminal kinase
KDR	Kinase insert domain receptor
Kg	Kilogram
Ki-67	Nuclear protein Ki-67
KIT	c-KIT proto-oncogene
LC/MS/MS	Liquid Chromatography-Tandem Mass Spectrometry
MAPK	Mitogen activated protein kinase
MEK	Mitogen-activated protein kinase kinase
MET	Mesenchymal Epithelial Transition factor
Mg	Milligram
MHz	MegaHertZ
mM	Millimolar
MPa	Megapascal
MRI	Magnetic Resonance Imaging
MRgFUS	Magnetic Resonance Guided Focused Ultrasound
mTOR	Mechanistic Target of Rapamycin Kinase
MYCN	v-myc myelocytomatosis viral related oncogene, neuroblastoma derived
NAD	Nicotinamide adenine dinucleotide
NeuN	Neuronal Nuclear protein
ng	Nanogram
NHP	Non-human primates
nM	Nanomolar
NOS	Nitric oxide synthase
Np/m	Nepers per meter
NSG	NOD SCID Gamma
NVU	Neurovascular Unit
OS	Overall survival
p53KO	Tumour protein 53 gene knockout

PARP	Poly ADP Ribose Polymerase
PAX3	Paired Box 3 gene
PcG	Polycomb group
PCNA	Proliferating Cell Nuclear Antigen
PDGFA	Platelet Derived Growth Factor Subunit A
PDGFB	Platelet Derived Growth Factor Subunit B
PDGFR	Platelet Derived Growth Factor Receptor
PEEK	Polyether ether-ketone
PET	Positron-emission tomography
P-gp	P-glycoprotein
PI3KR1	phosphoinositide-3-kinase regulatory subunit 1
PK	Protein kinase domain
PPM1D	Protein Phosphatase, Mg2+/Mn2+ Dependent 1D
PRC2	Polycomb Repressive Complex 2
PTEN	Phosphatase and tensin homolog
PVDF	Polyvinylidene diflouride
RAF	Rapidly Accelerated Fibrosarcoma family of serine/threonine protein kinases
RAS	Rat sarcoma virus
RCAS	Replication Competent Avian Sarcoma-Leukosis Virus (ASLV)long terminal (LTR) with splice acceptor
RTK	Receptor Tyrosine Kinase
SDS	Sodium dodecyl sulfate
SET	Su(var)39, EZH2 and Trithorax
STR	Short Tandem Repeat
TGFβ	Transforming growth factor beta
TK	Tyrosine Kinase
TNFα	Tumour necrosis factor α
TSC2	Tuberous Sclerosis Complex Subunit 2
TSM	Tumour Stem Medium
Tv-a	Avian Tumour Virus receptor A
TP53	Tumour Protein p53

Vd	Volume of distribution
VEGF	Vascular endothelial growth factor
Vi	Volume of infusion
WHO	World Health Organisation
ZIP	Zero Interaction Potency

References

1. Ostrom, Q. T. *et al.* CBTRUS Statistical Report: Primary brain and other central nervous system tumors diagnosed in the United States in 2010–2014. *Neuro-Oncology* 19, v1–v88 (2017).

2. Dang, M. & Phillips, P. C. Pediatric Brain Tumors. *Continuum (Minneap Minn)* 23, 1727–1757 (2017).

3. Pollack, I. F., Agnihotri, S. & Broniscer, A. Childhood brain tumors: current management, biological insights, and future directions. *J Neurosurg Pediatr* 23, 261–273 (2019).

4. Cancer, I. A. for R. on & Wiestler, O. D. *WHO Classification of Tumours of the Central Nervous System*. (International Agency for Research on Cancer, 2016).

5. Louis, D. N. *et al.* The 2016 World Health Organization Classification of Tumors of the Central Nervous System: a summary. *Acta Neuropathol* 131, 803–820 (2016).

6. Louis, D. N. *et al.* The 2021 WHO Classification of Tumors of the Central Nervous System: a summary. *Neuro-oncology* 23, 1231–1251 (2021).

7. Jansen, M. H. A., Vuurden, D. G. van, Vandertop, W. P. & Kaspers, G. J. L. Diffuse intrinsic pontine gliomas: A systematic update on clinical trials and biology. *Cancer Treatment Reviews* 38, 27–35 (2012).

8. Tisnado, J., Young, R., Peck, K. K. & Haque, S. Conventional and Advanced Imaging of Diffuse Intrinsic Pontine Glioma. *Journal of Child Neurology* 31, 1386–1393 (2016).

9. Caretti, V. *et al.* Subventricular spread of diffuse intrinsic pontine glioma. *Acta Neuropathol* 128, 605–607 (2014).

10. Hargrave, D., Bartels, U. & Bouffet, E. Diffuse brainstem glioma in children: critical review of clinical trials. *The Lancet Oncology* 7, 241–248 (2006).

11. Hoffman, L. M. *et al.* Clinical, Radiologic, Pathologic, and Molecular Characteristics of Long-Term Survivors of Diffuse Intrinsic Pontine Glioma (DIPG): A Collaborative Report From the International and European Society for Pediatric Oncology DIPG Registries. *Journal of Clinical Oncology* 36, 1963–1972 (2018).

12. Wu, G. *et al.* Somatic histone H3 alterations in pediatric diffuse intrinsic pontine gliomas and non-brainstem glioblastomas. *Nature Publishing Group* 44, 251–253 (2012).

13. Wolffe, A. P. *Chromatin*. (Academic Press, 2012).

14. Tagami, H., Ray-Gallet, D., Almouzni, G. & Nakatani, Y. Histone H3.1 and H3.3 complexes mediate nucleosome assembly pathways dependent or independent of DNA synthesis. *Cell* 116, 51–61 (2004).

15. Goldberg, A. D. *et al.* Distinct Factors Control Histone Variant H3.3 Localization at Specific Genomic Regions. *Cell* 140, 678–691 (2010).

16. biochemistry, M. O. A. review of & 1991. The regulation of histone synthesis in the cell cycle. *annualreviews.org* 60, 827–861 (1991).

17. Gaillard, P.-H. L. *et al.* Chromatin assembly coupled to DNA repair: a new role for chromatin assembly factor I. *Cell* 86, 887–896 (1996).

18. Shibahara, K. & Stillman, B. Replication-dependent marking of DNA by PCNA facilitates CAF-1-coupled inheritance of chromatin. *Cell* 96, 575–585 (1999).

19. Shen, X. *et al.* EZH1 mediates methylation on histone H3 lysine 27 and complements EZH2 in maintaining stem cell identity and executing pluripotency. *Mol. Cell* 32, 491–502 (2008).

20. Ferrari, K. J. *et al.* Polycomb-Dependent H3K27me1 and H3K27me2 Regulate Active Transcription and Enhancer Fidelity. *Mol. Cell* 53, 49–62 (2014).

21. Wang, Z. *et al.* Combinatorial patterns of histone acetylations and methylations in the human genome. *Nat Genet* 40, 897–903 (2008).

22. Stock, J. K. *et al.* Ring1-mediated ubiquitination of H2A restrains poised RNA polymerase II at bivalent genes in mouse ES cells. *Nature Cell Biology* 9, 1428–1435 (2007).

23. Chan, K. M. *et al.* The histone H3.3K27M mutation in pediatric glioma reprograms H3K27 methylation and gene expression. *Genes & Development* 27, 985–990 (2013).

24. Bender, S. *et al.* Reduced H3K27me3 and DNA Hypomethylation Are Major Drivers of Gene Expression in K27M Mutant Pediatric High-Grade Gliomas. *Cancer Cell* 24, 660–672 (2013).

25. Castel, D. *et al.* Transcriptomic and epigenetic profiling of 'diffuse midline gliomas, H3 K27M-mutant' discriminate two subgroups based on the type of histone H3 mutated and not supratentorial or infratentorial location. *Acta Neuropathologica Communications* 1–13 (2018) doi:10.1186/s40478-018-0614-1.

26. Lewis, P. W. *et al.* Inhibition of PRC2 Activity by a Gain-of-Function H3 Mutation Found in Pediatric Glioblastoma. *Science* 340, 857–861 (2013).

27. Venneti, S. *et al.* Evaluation of Histone 3 Lysine 27 Trimethylation (H3K27me3) and Enhancer of Zest 2 (EZH2) in Pediatric Glial and Glioneuronal Tumors Shows Decreased H3K27me3 in H3F3AK27M Mutant Glioblastomas. *Brain Pathology* 23, 558–564 (2013).

28. Cordero, F. J. *et al.* Histone H3.3K27M Represses p16 to Accelerate Gliomagenesis in a Murine Model of DIPG. *Mol Cancer Res* 15, 1243–1254 (2017).

29. Stafford, J. M. *et al.* Multiple modes of PRC2 inhibition elicit global chromatin alterations in H3K27M pediatric glioma. *Sci Adv* 4, eaau5935 (2018).

30. Wang, X. *et al.* Regulation of histone methylation by automethylation of PRC2. *Genes & Development* 33, 1416–1427 (2019).

31. Saratsis, A. M. *et al.* Comparative multidimensional molecular analyses of pediatric diffuse intrinsic pontine glioma reveals distinct molecular subtypes. *Acta Neuropathol* 127, 881–895 (2013).

32. Huether, R. *et al.* The landscape of somatic mutations in epigenetic regulators across 1,000 paediatric cancer genomes. *Nature Communications* 5, 619–16 (2014).

33. Castel, D. *et al.* Histone H3F3A and HIST1H3B K27M mutations define two subgroups of diffuse intrinsic pontine gliomas with different prognosis and phenotypes. *Acta Neuropathol* 130, 815–827 (2015).

34. Liu, X., McEachron, T. A., Schwartzentruber, J. & Wu, G. Histone H3 Mutations in Pediatric Brain Tumors. *Cold Spring Harbor Perspectives in Biology* 6, a018689–a018689 (2014).

35. Khuong-Quang, D.-A. *et al.* K27M mutation in histone H3.3 defines clinically and biologically distinct subgroups of pediatric diffuse intrinsic pontine gliomas. *Acta Neuropathol* 124, 439–447 (2012).

36. Nikbakht, H. *et al.* Spatial and temporal homogeneity of driver mutations in diffuse intrinsic pontine glioma. *Nature Communications* 7, 573–8 (2016).

37. Valer, Sánchez-de-Diego, Pimenta-Lopes, Rosa & Ventura. ACVR1 Function in Health and Disease. *Cells* 8, 1366–26 (2019).

38. Lapin, D. H., Tsoli, M. & Ziegler, D. S. Genomic Insights into Diffuse Intrinsic Pontine Glioma. *Front. Oncol.* 7, 5–7 (2017).

39. Taylor, K. R., Vinci, M., Bullock, A. N. & Jones, C. ACVR1Mutations in DIPG: Lessons Learned from FOP. *Cancer Research* 74, 4565–4570 (2014).

40. Huse, M. *et al.* The TGF beta receptor activation process: an inhibitor- to substrate-binding switch. *Mol. Cell* 8, 671–682 (2001).

41. Yadin, D., Knaus, P. & Mueller, T. D. Structural insights into BMP receptors: Specificity, activation and inhibition. *Cytokine and Growth Factor Reviews* 27, 13–34 (2016).

42. Derynck, R. & Zhang, Y. E. Smad-dependent and Smad-independent pathways in TGF-beta family signalling. *Nature* 425, 577–584 (2003).

43. Schmierer, B. & Hill, C. S. TGFβ–SMAD signal transduction: molecular specificity and functional flexibility. *Nature Reviews Molecular Cell Biology* 8, 970–982 (2007).

44. Shen, Q. *et al.* The fibrodysplasia ossificans progressiva R206H ACVR1 mutation activates BMP-independent chondrogenesis and zebrafish embryo ventralization. *J. Clin. Invest.* 75, 215–11 (2009).

45. Song, G.-A. *et al.* Molecular Consequences of the ACVR1 R206HMutation of Fibrodysplasia Ossificans Progressiva. *J. Biol. Chem.* 285, 22542–22553 (2010).

46. Severino, M. *et al.* Novel asymptomatic CNS findings in patients with ACVR1/ALK2mutations causing fibrodysplasia ossificans progressiva. *Journal of Medical Genetics* 53, 859–864 (2016).

47. Buczkowicz, P. *et al.* Genomic analysis of diffuse intrinsic pontine gliomas identifies three molecular subgroups and recurrent activating ACVR1 mutations. *Nat Genet* 46, 451–456 (2014).

48. Project, the St. J. C. R. H. U. P. C. G. The genomic landscape of diffuse intrinsic pontine glioma and pediatric non-brainstem high-grade glioma. *Nat Genet* 46, 444–450 (2014).

49. Puget, S. *et al.* Mesenchymal Transition and PDGFRA Amplification/Mutation Are Key Distinct Oncogenic Events in Pediatric Diffuse Intrinsic Pontine Gliomas. *PLoS ONE* 7, e30313-14 (2012).

50. Bond, A. M., Bhalala, O. G. & Kessler, J. A. The dynamic role of bone morphogenetic proteins in neural stem cell fate and maturation. *Devel Neurobio* 72, 1068–1084 (2012).

51. Mackay, A. *et al.* Integrated Molecular Meta-Analysis of 1,000 Pediatric High-Grade and Diffuse Intrinsic Pontine Glioma. *Cancer Cell* 32, 520-537.e5 (2017).

52. Maclaine, N. J. & Hupp, T. R. The regulation of p53 by phosphorylation: a model for how distinct signals integrate into the p53 pathway. *Aging (Albany NY)* 1, 490–502 (2009).

53. Duchatel, R. J. *et al.* Signal Transduction in Diffuse Intrinsic Pontine Glioma. *Proteomics* 19, 1800479–15 (2019).

54. Monje, M., Mitra, S. S., the, M. F. P. of & 2011. Hedgehog-responsive candidate cell of origin for diffuse intrinsic pontine glioma. *National Acad Sciences* 1–6 (2011) doi:10.1073/pnas.1101657108/-/dcsupplemental.

55. Werbrouck, C. *et al.* TP53 Pathway Alterations Drive Radioresistance in Diffuse Intrinsic Pontine Gliomas (DIPG). *Clin. Cancer Res.* 25, 6788–6800 (2019).

56. Zarghooni, M. *et al.* Whole-Genome Profiling of Pediatric Diffuse Intrinsic Pontine Gliomas Highlights Platelet-Derived Growth Factor Receptor α and Poly (ADP-ribose) Polymerase As Potential Therapeutic Targets. *Journal of Clinical Oncology* 28, 1337–1344 (2010).

57. Bazenet, C. E., Gelderloos, J. A. & Kazlauskas, A. Phosphorylation of tyrosine 720 in the platelet-derived growth factor alpha receptor is required for binding of Grb2 and SHP-2 but not for activation of Ras or cell proliferation. *Molecular and Cellular Biology* 16, 6926–6936 (1996).

58. Heldin, C. H., Ostman, A. & Rönnstrand, L. Signal transduction via platelet-derived growth factor receptors. *Biochim. Biophys. Acta* 1378, F79-113 (1998).

59. Zhang, S. Q. *et al.* Shp2 regulates SRC family kinase activity and Ras/Erk activation by controlling Csk recruitment. *Mol. Cell* 13, 341–355 (2004).

60. Dai, C. *et al.* PDGF autocrine stimulation dedifferentiates cultured astrocytes and induces oligodendrogliomas and oligoastrocytomas from neural progenitors and astrocytes in vivo. *Genes & Development* 15, 1913–1925 (2001).

61. Shih, A. H. & Holland, E. C. Platelet-derived growth factor (PDGF) and glial tumorigenesis. *Cancer Letters* 232, 139–147 (2006).

62. Masui, K. *et al.* Glial progenitors in the brainstem give rise to malignant gliomas by platelet-derived growth factor stimulation. *Glia* 58, 1050–1065 (2010).

63. Koschmann, C. *et al.* Multi-focal sequencing of a diffuse intrinsic pontine glioma establishes PTEN loss as an early event. *npj Precision Oncology* 1–3 (2017) doi:10.1038/s41698-017-0033-y.

64. Wu, Y. L. *et al.* Dual Inhibition of PI3K/AKT and MEK/ERK Pathways Induces Synergistic Antitumor Effects in Diffuse Intrinsic Pontine Glioma Cells. *Translational Oncology* 10, 221–228 (2017).

65. Becher, O. J. *et al.* A phase I study of perifosine with temsirolimus for recurrent pediatric solid tumors. *Pediatr Blood Cancer* 64, e26409-9 (2016).

66. Truffaux, N. *et al.* Preclinical evaluation of dasatinib alone and in combination with cabozantinib for the treatment of diffuse intrinsic pontine glioma. *Neuro-Oncology* 17, 953–964 (2014).

67. Zitzmann, K. *et al.* Compensatory activation of Akt in response to mTOR and Raf inhibitors – A rationale for dual-targeted therapy approaches in neuroendocrine tumor disease. *Cancer Letters* 295, 100–109 (2010).

68. You, Z. *et al.* CtIP Links DNA Double-Strand Break Sensing to Resection. *Mol. Cell* 36, 954–969 (2009).

69. Ditch, S. & Paull, T. T. The ATM protein kinase and cellular redox signaling: beyond the DNA damage response. *Trends in Biochemical Sciences* 37, 15–22 (2012).

70. Jallo, G. I. *et al.* Experimental models of brainstem tumors: development of a neonatal rat model. *Childs Nerv Syst* 21, 399–403 (2005).

71. Jallo, G. I., Volkov, A., Wong, C., Sr., B. S. C. & Penno, M. B. A novel brainstem tumor model: functional and histopathological characterization. *Childs Nerv Syst* 22, 1519–1525 (2006).

72. Sho, A., Kondo, S., Kamitani, H., Otake, M. & Watanabe, T. Establishment of experimental glioma models at the intrinsic brainstem region of the rats. *Neurological Research* 29, 36–42 (2013).

73. Caretti, V. *et al.* Monitoring of Tumor Growth and Post-Irradiation Recurrence in a Diffuse Intrinsic Pontine Glioma Mouse Model. *Brain Pathology* 21, 441–451 (2010).

74. Aoki, Y. *et al.* An experimental xenograft mouse model of diffuse pontine glioma designed for therapeutic testing. *Journal of Neuro-Oncology* 108, 29–35 (2012).

75. Hashizume, R. *et al.* A human brainstem glioma xenograft model enabled for bioluminescence imaging. *Journal of Neuro-Oncology* 96, 151–159 (2009).

76. Bailey, S. *et al.* Diffuse intrinsic pontine glioma treated with prolonged temozolomide and radiotherapy â€" Results of a United Kingdom phase II trial (CNS 2007 04). *European Journal of Cancer* 49, 3856–3862 (2013).

77. Chassot, A. *et al.* Radiotherapy with concurrent and adjuvant temozolomide in children with newly diagnosed diffuse intrinsic pontine glioma. *Journal of Neuro-Oncology* 106, 399–407 (2011).

78. Monje, M. *et al.* Hedgehog-responsive candidate cell of origin for diffuse intrinsic pontine glioma. *Proc. Natl. Acad. Sci. U.S.A.* 108, 4453–4458 (2011).

79. Hashizume, R. *et al.* Characterization of a diffuse intrinsic pontine glioma cell line: implications for future investigations and treatment. *Journal of Neuro-Oncology* 110, 305–313 (2012).

80. Mueller, S. *et al.* Targeting Wee1 for the treatment of pediatric high-grade gliomas. *Neuro-Oncology* 16, 352–360 (2013).

81. Grasso, C. S. *et al.* Functionally defined therapeutic targets in diffuse intrinsic pontine glioma. *Nature Publishing Group* 21, 555–559 (2015).

82. Hoffman, L. M., Salloum, R. & Fouladi, M. Molecular biology of pediatric brain tumors and impact on novel therapies. *Curr Neurol Neurosci Rep* 15, 10–10 (2015).

83. Becher, O. J. *et al.* Preclinical evaluation of radiation and perifosine in a genetically and histologically accurate model of brainstem glioma. *Cancer Research* 70, 2548–2557 (2010).

84. Werder, A. von, Seidler, B., Schmid, R. M., Schneider, G. uuml nter & Saur, D. Production of avian retroviruses and tissue-specific somatic retroviral gene transfer in vivo using the RCAS/TVA system. *Nature Protocols* 7, 1–17 (2019).

85. Ahronian, L. G. & Lewis, B. C. Using the RCAS-TVA system to model human cancer in mice. *Cold Spring Harbor Protocols* 2014, 1128–1135 (2014).

86. Himly, M., Foster, D. N., Bottoli, I., Iacovoni, J. S. & Vogt, P. K. The DF-1 chicken fibroblast cell line: transformation induced by diverse oncogenes and cell death resulting from infection by avian leukosis viruses. *Virology* 248, 295–304 (1998).

87. Misuraca, K. L. *et al.* Pax3 expression enhances PDGF-B-induced brainstem gliomagenesis and characterizes a subset of brainstem glioma. *Acta Neuropathol Commun* 2, 134 (2014).

88. Patel, S. K. *et al.* Generation of diffuse intrinsic pontine glioma mouse models by brainstem targeted in utero electroporation. *Neuro-Oncology* 1–12 (2019) doi:10.1093/neuonc/noz197.

89. Pathania, M. *et al.* H3.3K27M Cooperates with Trp53 Loss and PDGFRA Gain in Mouse Embryonic Neural Progenitor Cells to Induce Invasive High-Grade Gliomas. *Cancer Cell* 32, 684-700.e9 (2017).

90. Lin, G. L. & Monje, M. A Protocol for Rapid Post-mortem Cell Culture of Diffuse Intrinsic Pontine Glioma (DIPG). *JoVE* 1–8 (2017) doi:10.3791/55360.

91. Misuraca, K. L., Cordero, F. J. & Becher, O. J. Pre-Clinical Models of Diffuse Intrinsic Pontine Glioma. *Front. Oncol.* 5, 205–7 (2015).

92. Plessier, A. *et al.* New in vivo avatars of diffuse intrinsic pontine gliomas (DIPG) from stereotactic biopsies performed at diagnosis. *Oncotarget* 8, 52543–52559 (2017).

93. Warren, K. E. Beyond the Blood:Brain Barrier: The Importance of Central Nervous System (CNS) Pharmacokinetics for the Treatment of CNS Tumors, Including Diffuse Intrinsic Pontine Glioma. *Front. Oncol.* 8, 815–11 (2018).

94. Banks, W. A. From blood–brain barrier to blood– brain interface: new opportunities for CNS drug delivery. *Nature Publishing Group* 1–18 (2016) doi:10.1038/nrd.2015.21.

95. Hawkins, B. T. & Davis, T. P. The Blood-Brain Barrier/Neurovascular Unit in Health and Disease. *Pharmacol Rev* 57, 173–185 (2005).

96. Maness, L. M., Banks, W. A., Zadina, J. E. & Kastin, A. J. Selective transport of blood-borne interleukin-1 alpha into the posterior division of the septum of the mouse brain. *Brain Res.* 700, 83–88 (1995).

97. Moinuddin, A., Morley, J. E. & Banks, W. A. Regional Variations in the Transport of Interleukin-1α across the Blood-Brain Barrier in ICR and Aging SAMP8 Mice. *Neuroimmunomodulation* 8, 165–170 (2000).

98. McCully, C. M. *et al.* Model for concomitant microdialysis sampling of the pons and cerebral cortex in rhesus macaques (Macaca mulatta). *Comp. Med.* 63, 355–360 (2013).

99. Sarkaria, J. N. *et al.* Is the blood–brain barrier really disrupted in all glioblastomas? A critical assessment of existing clinical data. *Neuro-Oncology* 20, 184–191 (2017).

100. Ghersi-Egea, J.-F. *et al.* Molecular anatomy and functions of the choroidal blood-cerebrospinal fluid barrier in health and disease. *Acta Neuropathol* 135, 337–361 (2018).

101. Morrison, P. F. & Dedrick, R. L. Transport of Cisplatin in Rat Brain Following Microinfusion: an Analysis. *J. Pharm. Sci.* 75, 120–128 (1986).

102. Nicholson, C. & Hrabětová, S. Brain Extracellular Space: The Final Frontier of Neuroscience. *Biophysj* 113, 2133–2142 (2017).

103. Bouffet, E. *et al.* Radiotherapy followed by high dose busulfan and thiotepa: a prospective assessment of high dose chemotherapy in children with diffuse pontine gliomas. *Cancer* 88, 685–692 (2000).

104. Broniscer, A. *et al.* Radiation Therapy and High-Dose Tamoxifen in the Treatment of Patients With Diffuse Brainstem Gliomas: Results of a Brazilian Cooperative Study. *Journal of Clinical Oncology* 18, 1246–1253 (2000).

105. Massimino, M. *et al.* Results of nimotuzumab and vinorelbine, radiation and re-irradiation for diffuse pontine glioma in childhood. *Journal of Neuro-Oncology* 1–8 (2014) doi:10.1007/s11060-014-1428-z.

106. Michalski, A. *et al.* The addition of high-dose tamoxifen to standard radiotherapy does not improve the survival of patients with diffuse intrinsic pontine glioma. *Journal of Neuro-Oncology* 100, 81–88 (2010).

107. Yamashita, J. *et al.* Intra-arterial ACNU therapy for malignant brain tumors. Experimental studies and preliminary clinical results. *Journal of Neurosurgery* 59, 424–430 (1983).

108. Joshi, S., Meyers, P. M. & Ornstein, E. Intracarotid Delivery of Drugs. *Anesthesiology* 109, 543–564 (2008).

109. Dedrick, R. L. Arterial drug infusion: pharmacokinetic problems and pitfalls. *JNCI Journal of the National Cancer Institute* 80, 84–89 (1988).

110. Saris, S. C., Wright, D. C., Oldfield, E. H. & Blasberg, R. G. Intravascular streaming and variable delivery to brain following carotid artery infusions in the Sprague-Dawley rat. *J. Cereb. Blood Flow Metab.* 8, 116–120 (1988).

111. Lutz, R. J. *et al.* Mixing studies during intracarotid artery infusions in an in vitro model. *Journal of Neurosurgery* 64, 277–283 (1986).

112. Saris, S. C. *et al.* Carotid artery mixing with diastole-phased pulsed drug infusion. *Journal of Neurosurgery* 67, 721–725 (1987).

113. Hori, T. *et al.* Influence of modes of ACNU administration on tissue and blood drug concentration in malignant brain tumors. *Journal of Neurosurgery* 66, 372–378 (1987).

114. Shapiro, W. R. *et al.* A randomized comparison of intra-arterial versus intravenous with or without intravenous 5-fluorouracil, for newly diagnosed patients with malignant glioma. *Journal of Neurosurgery* 76, 772–781 (1992).

115. Kochii, M. *et al.* Randomized comparison of intra-arterial versus intravenous infusion of ACNU for newly diagnosed patients with glioblastoma. *Journal of Neuro-Oncology* 49, 63–70 (2000).

116. Imbesi, F. *et al.* A randomized phase III study: comparison between intravenous and intraarterial ACNU administration in newly diagnosed primary glioblastomas. *Anticancer Res.* 26, 553–558 (2006).

117. Lutz, R. J., Warren, K., Balis, F., Patronas, N. & Dedrick, R. L. Mixing during intravertebral arterial infusions in an in vitro model. *Journal of Neuro-Oncology* 58, 95–106 (2002).

118. Fortin, D. *et al.* Unusual cervical spinal cord toxicity associated with intra-arterial carboplatin, intra-arterial or intravenous etoposide phosphate, and intravenous cyclophosphamide in conjunction with osmotic blood brain-barrier disruption in the vertebral artery. *American Journal of Neuroradiology* 20, 1794–1802 (1999).

119. Wetmore, S. J., Koike, K. J. & Bloomfield, S. M. Profound hearing loss from intravertebral artery cisplatin. *Otolaryngol Head Neck Surg* 116, 234–237 (1997).

120. Valtonen, S. *et al.* Interstitial chemotherapy with carmustine-loaded polymers for high-grade gliomas: a randomized double-blind study. *Neurosurgery* 41, 44-8-discussion 48-9 (1997).

121. Westphal, M. *et al.* A phase 3 trial of local chemotherapy with biodegradable carmustine (BCNU) wafers (Gliadel wafers) in patients with primary malignant glioma. *Neuro-Oncology* 5, 79–88 (2003).

122. Westphal, M. *et al.* Gliadel® wafer in initial surgery for malignant glioma: long-term follow-up of a multicenter controlled trial. *Acta Neurochir (Wien)* 148, 269–275 (2006).

123. Fojo, A., Akiyama, S., Gottesman, M. M. & Pastan, I. Reduced Drug Accumulation in Multiply Drug-resistant Human KB Carcinoma Cell Lines. *Cancer Research* 45, 3002–3007 (1985).

124. Schinkel, A. H. *et al.* Multidrug resistance and the role of P-glycoprotein knockout mice. *European Journal of Cancer* 31A, 1295–1298 (1995).

125. Tatsuta, T., Naito, M., Oh-Hara, T., Sugawara, I. & Tsuruo, T. Functional involvement of P-glycoprotein in blood-brain barrier. *J. Biol. Chem.* 267, 20383–20391 (1992).

126. Warren, K. E., Patel, M. C., McCully, C. M., Montuenga, L. M. & Balis, F. M. Effect of P-glycoprotein modulation with cyclosporin A on cerebrospinal fluid penetration of doxorubicin in non-human primates. *Cancer Chemother. Pharmacol.* 45, 207–212 (2000).

127. Asperen, J. V., Schinkel, A. H., the, J. B. J. J. of & 1996. Altered pharmacokinetics of vinblastine in Mdr1a P-glycoprotein-deficient Mice. *academic.oup.com*.

128. Greenberg, M. L. *et al.* Etoposide, vincristine, and cyclosporin A with standard-dose radiation therapy in newly diagnosed diffuse intrinsic brainstem gliomas: A pediatric oncology group phase I study. *Pediatr Blood Cancer* 45, 644–648 (2005).

129. Hinchey, J. *et al.* A reversible posterior leukoencephalopathy syndrome. *N. Engl. J. Med.* 334, 494–500 (1996).

130. Zhou, Z., Current, R. S. & 2017. Convection-enhanced delivery for diffuse intrinsic pontine glioma treatment. *ingentaconnect.com* doi:10.2174/1570159x14666160614093.

131. Barua, N. U. *et al.* Robot-guided convection-enhanced delivery of carboplatin for advanced brainstem glioma. *Acta Neurochir (Wien)* 155, 1459–1465 (2013).

132. Barua, N. U. *et al.* Intermittent convection-enhanced delivery to the brain through a novel transcutaneous bone-anchored port. *Journal of Neuroscience Methods* 214, 223–232 (2013).

133. Bienemann, A. *et al.* The development of an implantable catheter system for chronic or intermittent convection-enhanced delivery. *Journal of Neuroscience Methods* 203, 284–291 (2012).

134. Lewis, O. *et al.* Maximising coverage of brain structures using controlled reflux, convection-enhanced delivery and the recessed step catheter. *Journal of Neuroscience Methods* 308, 337–345 (2018).

135. Barua, N. U. *et al.* A novel implantable catheter system with transcutaneous port for intermittent convection-enhanced delivery of carboplatin for recurrent glioblastoma. *Drug Deliv* 23, 167–173 (2014).

136. Shasby, G. Erratum. The distribution, clearance, and brainstem toxicity of panobinostat administered by convection-enhanced delivery. *J Neurosurg Pediatr* 23, 133–9 (2018).

137. Saito, R. *et al.* Tissue affinity of the infusate affects the distribution volume during convection-enhanced delivery into rodent brains: Implications for local drug delivery. *Journal of Neuroscience Methods* 154, 225–232 (2006).

138. Mardor, Y. *et al.* Convection-enhanced drug delivery: increased efficacy and magnetic resonance image monitoring. *Cancer Research* 65, 6858–6863 (2005).

139. Allard, E., Passirani, C. & Benoit, J.-P. Convection-enhanced delivery of nanocarriers for the treatment of brain tumors. *Biomaterials* 30, 2302–2318 (2009).

140. Louis, N. *et al.* New therapeutic approaches for brainstem tumors: a comparison of delivery routes using nanoliposomal irinotecan in an animal model. *Journal of Neuro-Oncology* 136, 475–484 (2017).

141. Lewis, O. *et al.* Chronic, intermittent convection-enhanced delivery devices. *Journal of Neuroscience Methods* 259, 47–56 (2016).

142. Geer, C. P. & Grossman, S. A. Interstitial fluid flow along white matter tracts: a potentially important mechanism for the dissemination of primary brain tumors. *Journal of Neuro-Oncology* 32, 193–201 (1997).

143. Voges, J. *et al.* Imaging-guided convection-enhanced delivery and gene therapy of glioblastoma. *Ann Neurol.* 54, 479–487 (2003).

144. Heiss, J. D., Walbridge, S., Asthagiri, A. R. & Lonser, R. R. Image-guided convection-enhanced delivery of muscimol to the primate brain. *Journal of Neurosurgery* 112, 790–795 (2010).

145. DAVIDCROTEAU, M. D. S. B. S. P. M. P. D. J. B. M. D. A. V. M. D. D. B. S. M. B. A. E. O. M. D. A. L. M. D. Real-time in vivo imaging of the convective distribution of a low-molecular-weight tracer. *Journal of Neurosurgery* 102, 1–8 (2004).

146. Stine, C. A. & Munson, J. M. Convection-Enhanced Delivery: Connection to and Impact of Interstitial Fluid Flow. *Front. Oncol.* 9, 597–15 (2019).

147. Varenika, V. *et al.* Detection of infusate leakage in the brain using real-time imaging of convection-enhanced delivery. *Journal of Neurosurgery* 109, 874–880 (2009).

148. Sampson, J. H. *et al.* Clinical utility of a patient-specific algorithm for simulating intracerebral drug infusions. *Neuro-Oncology* 9, 343–353 (2007).

149. Lonser, R. R. Imaging of Convective Drug Delivery in the Nervous System. *Neurosurgery Clinics of North America* 28, 615–622 (2017).

150. Lonser, R. R. *et al.* Successful and safe perfusion of the primate brainstem: in vivo magnetic resonance imaging of macromolecular distribution during infusion. *Journal of Neurosurgery* 97, 905–913 (2002).

151. Lonser, R. R. *et al.* Real-time image-guided direct convective perfusion of intrinsic brainstem lesions. Technical note. *Journal of Neurosurgery* 107, 190–197 (2007).

152. Gimenez, F. *et al.* Image-guided convection-enhanced delivery of GDNF protein into monkey putamen. *NeuroImage* 54, S189–S195 (2011).

153. Ding, D. *et al.* Convection-enhanced delivery of free gadolinium with the recombinant immunotoxin MR1-1. *Journal of Neuro-Oncology* 98, 1–7 (2009).

154. Murad, G. J. A. *et al.* Image-guided convection-enhanced delivery of gemcitabine to the brainstem. *Journal of Neurosurgery* 106, 351–356 (2007).

155. Richardson, R. M. *et al.* Interventional MRI-guided Putaminal Delivery of AAV2-GDNF for a Planned Clinical Trial in Parkinson'ns Disease. *Molecular Therapy* 19, 1048–1057 (2009).

156. Su, X. *et al.* Real-time MR Imaging With Gadoteridol Predicts Distribution of Transgenes After Convection-enhanced Delivery of AAV2 Vectors. *Molecular Therapy* 18, 1490–1495 (2009).

157. Ksendzovsky, A. *et al.* Convection-enhanced delivery of M13 bacteriophage to the brain. *Journal of Neurosurgery* 117, 197–203 (2013).

158. Murad, G. J. A. Real-time, Image-Guided, Convection-Enhanced Delivery of Interleukin 13 Bound to Pseudomonas Exotoxin. *Clin. Cancer Res.* 12, 3145–3151 (2006).

159. Lonser, R. R., Sarntinoranont, M., Morrison, P. F. & Oldfield, E. H. Convection-enhanced delivery to the central nervous system. *Journal of Neurosurgery* 122, 697–706 (2015).

160. Luther, N. *et al.* The potential of theragnostic 124I-8H9 convection-enhanced delivery in diffuse intrinsic pontine glioma. *Neuro-Oncology* 16, 800–806 (2014).

161. Lonser, R. R. *et al.* Image-guided, direct convective delivery of glucocerebrosidase for neuronopathic Gaucher disease. *Neurology* 68, 254–261 (2007).

162. Souweidane, M. M. *et al.* Convection-enhanced delivery for diffuse intrinsic pontine glioma: a single-centre, dose-escalation, phase 1 trial. *The Lancet Oncology* 19, 1040–1050 (2018).

163. Vuurden, D. G. van. Convection-enhanced delivery: chemosurgery in diffuse intrinsic pontine glioma. *Lancet Oncology* 19, 1001–1003 (2018).

164. Wagner, S. *et al.* Secondary dissemination in children with high-grade malignant gliomas and diffuse intrinsic pontine gliomas. *Br J Cancer* 95, 991–997 (2006).

165. Mantravadi, R. V., Phatak, R., Bellur, S., Liebner, E. J. & Haas, R. Brain stem gliomas: an autopsy study of 25 cases. *Cancer* 49, 1294–1296 (1982).

166. Zünkeler, B. *et al.* Quantification and pharmacokinetics of blood-brain barrier disruption in humans. *Journal of Neurosurgery* 85, 1056–1065 (1996).

167. Inamura, T. & Black, K. L. Bradykinin selectively opens blood-tumor barrier in experimental brain tumors. *J. Cereb. Blood Flow Metab.* 14, 862–870 (1994).

168. Nomura, T., Inamura, T. & Black, K. L. Intracarotid infusion of bradykinin selectively increases blood-tumor permeability in 9L and C6 brain tumors. *Brain Res.* 659, 62–66 (1994).

169. Nakano, S., Matsukado, K. & Black, K. L. Increased Brain Tumor Microvessel Permeability after Intracarotid Bradykinin Infusion Is Mediated by Nitric Oxide. *Cancer Research* 56, 4027–4031 (1996).

170. Kroll, R. A. *et al.* Improving drug delivery to intracerebral tumor and surrounding brain in a rodent model: a comparison of osmotic versus bradykinin modification of the blood-brain and/or blood-tumor barriers. *Neurosurgery* 43, 879-86-discussion 886-9 (1998).

171. Warren, K. *et al.* Phase II trial of intravenous lobradimil and carboplatin in childhood brain tumors: a report from the Children's Oncology Group. *Cancer Chemother. Pharmacol.* 58, 343–347 (2006).

172. Wells, P. N. T. *Biomedical ultrasonics*. (Academic Pr, 1977).

173. Clement, G. T., Sun, J., Giesecke, T. & Hynynen, K. A hemisphere array for non-invasive ultrasound brain therapy and surgery. *Phys Med Biol* 45, 3707–3719 (2000).

174. Sapareto, S. A. & Dewey, W. C. Thermal dose determination in cancer therapy. *Radiation Oncology Biology* 10, 787–800 (1984).

175. Sivakumar, M. *et al.* Transdermal drug delivery using ultrasound-theory, understanding and critical analysis. *Cell. Mol. Biol. (Noisy-le-grand)* 51 Suppl, OL767-84 (2005).

176. Mitragotri, S. Healing sound: the use of ultrasound in drug delivery and other therapeutic applications. *Nature Publishing Group* 4, 255–260 (2005).

177. Miller, D. L., Pislaru, S. V. & Greenleaf, J. E. Sonoporation: mechanical DNA delivery by ultrasonic cavitation. *Somat. Cell Mol. Genet.* 27, 115–134 (2002).

178. Tsutsui, J. M., Xie, F. & Porter, R. T. The use of microbubbles to target drug delivery. *Cardiovasc Ultrasound* 2, 290–7 (2004).

179. BAKAY, L., BALLANTINE, H. T., HUETER, T. F. & SOSA, D. Ultrasonically produced changes in the blood-brain barrier. *AMA Arch Neurol Psychiatry* 76, 457–467 (1956).

180. Patrick, J. T. *et al.* Ultrasound and the blood-brain barrier. *Adv. Exp. Med. Biol.* 267, 369–381 (1990).

181. Edmonds, P. D., biology, K. S. U. in medicine & 1983. Evidence for free radical production by ultrasonic cavitation in biological media. *Elsevier* 9, 635–639 (1983).

182. Apfel, R. E. Acoustic cavitation: a possible consequence of biomedical uses of ultrasound. *Br. J. Cancer Suppl.* 5, 140–146 (1982).

183. Miller, D. L. Particle gathering and microstreaming near ultrasonically activated gas-filled micropores. *J. Acoust. Soc. Am.* 84, 1378–1387 (1988).

184. McDannold, N., Vykhodtseva, N. & Hynynen, K. Targeted disruption of the blood–brain barrier with focused ultrasound: association with cavitation activity. *Phys Med Biol* 51, 793–807 (2006).

185. Sheikov, N., McDannold, N., Vykhodtseva, N., Jolesz, F. & Hynynen, K. Cellular mechanisms of the blood-brain barrier opening induced by ultrasound in presence of microbubbles. *Ultrasound in Medicine & Biology* 30, 979–989 (2004).

186. Raymond, S. B., Skoch, J., Hynynen, K. & Bacskai, B. J. Multiphoton Imaging of Ultrasound/Optison Mediated Cerebrovascular Effects in vivo. *J. Cereb. Blood Flow Metab.* 27, 393–403 (2006).

187. O'Reilly, M. A. & Hynynen, K. Blood-Brain Barrier: Real-time Feedback-controlled Focused Ultrasound Disruption by Using an Acoustic Emissions–based Controller. *Radiology* 263, 96–106 (2012).

188. Clement, G. T. & Hynynen, K. A non-invasive method for focusing ultrasound through the human skull. *Phys Med Biol* 47, 1219–1236 (2002).

189. Hynynen, K. *et al.* 500-element ultrasound phased array system for noninvasive focal surgery of the brain: A preliminary rabbit study with ex vivo human skulls. *Magn. Reson. Med.* 52, 100–107 (2004).

190. Hynynen, K. *et al.* Pre-clinical testing of a phased array ultrasound system for MRI-guided noninvasive surgery of the brain—A primate study. *European Journal of Radiology* 59, 149–156 (2006).

191. Sheikov, N., McDannold, N., Sharma, S. & Hynynen, K. Effect of Focused Ultrasound Applied With an Ultrasound Contrast Agent on the Tight Junctional Integrity of the Brain Microvascular Endothelium. *Ultrasound in Medicine & Biology* 34, 1093–1104 (2008).

192. O'Reilly, M. A., Hough, O. & Hynynen, K. Blood-Brain Barrier Closure Time After Controlled Ultrasound-Induced Opening Is Independent of Opening Volume. *J Ultrasound Med* 36, 475–483 (2017).

193. Treat, L. H., McDannold, N., Zhang, Y., Vykhodtseva, N. & Hynynen, K. Improved Anti-Tumor Effect of Liposomal Doxorubicin After Targeted Blood-Brain Barrier Disruption by MRI-Guided Focused Ultrasound in Rat Glioma. *Ultrasound in Medicine & Biology* 38, 1716–1725 (2012).

194. Wei, K.-C. *et al.* Focused Ultrasound-Induced Blood–Brain Barrier Opening to Enhance Temozolomide Delivery for Glioblastoma Treatment: A Preclinical Study. *PLoS ONE* 8, e58995-10 (2013).

195. Alkins, R., Burgess, A., Kerbel, R., Wels, W. S. & Hynynen, K. Early treatment of HER2-amplified brain tumors with targeted NK-92 cells and focused ultrasound improves survival. *Neuro-Oncology* 18, 974–981 (2016).

196. Kinoshita, M., McDannold, N., Jolesz, F. A. & Hynynen, K. Noninvasive localized delivery of Herceptin to the mouse brain by MRI-guided focused ultrasound-induced blood–brain barrier disruption. *Proc. Natl. Acad. Sci. U.S.A.* 103, 1–5 (2006).

197. Hennika, T. *et al.* Pre-Clinical Study of Panobinostat in Xenograft and Genetically Engineered Murine Diffuse Intrinsic Pontine Glioma Models. *PLoS ONE* 12, e0169485-20 (2017).

198. Rodgers, L. T. *et al.* Characterizing the pharmacokinetics of panobinostat in a non-human primate model for the treatment of diffuse intrinsic pontine glioma. *Cancer Chemoth Pharm* 85, 827–830 (2020).

199. Uchida, Y. *et al.* Quantitative targeted absolute proteomics of human blood–brain barrier transporters and receptors. *J Neurochem* 117, 333–345 (2011).

200. Singleton, W. G. B. *et al.* The distribution, clearance, and brainstem toxicity of panobinostat administered by convection-enhanced delivery. *J Neurosurg Pediatrics* 22, 288–296 (2018).

201. Wang, Y., Luo, W. & Wang, Y. PARP-1 and its associated nucleases in DNA damage response. *Dna Repair* 81, 102651 (2019).

202. Chaudhuri, A. R. & Nussenzweig, A. The multifaceted roles of PARP1 in DNA repair and chromatin remodelling. *Nat Rev Mol Cell Bio* 18, 610–621 (2017).

203. Poirier, G. G., Murcia, G. de, Jongstra-Bilen, J., Niedergang, C. & Mandel, P. Poly(ADP-ribosyl)ation of polynucleosomes causes relaxation of chromatin structure. *Proc National Acad Sci* 79, 3423–3427 (1982).

204. Hanzlikova, H. *et al.* The Importance of Poly(ADP-Ribose) Polymerase as a Sensor of Unligated Okazaki Fragments during DNA Replication. *Mol Cell* 71, 319-331.e3 (2018).

205. Pommier, Y., O'Connor, M. J. & Bono, J. de. Laying a trap to kill cancer cells: PARP inhibitors and their mechanisms of action. *Sci Transl Med* 8, 362ps17-362ps17 (2016).

206. Chornenkyy, Y. *et al.* Poly-ADP-Ribose Polymerase as a Therapeutic Target in Pediatric Diffuse Intrinsic Pontine Glioma and Pediatric High-Grade Astrocytoma. *Mol Cancer Ther* 14, 2560–2568 (2015).

207. Baxter, P. A. *et al.* A Phase I/II Study of Veliparib (ABT-888) with Radiation and Temozolomide in Newly Diagnosed Diffuse Pontine Glioma: A Pediatric Brain Tumor Consortium Study. *Neuro-oncology* 22, 875–885 (2020).

208. Koncar, R. F. *et al.* Identification of Novel RAS Signaling Therapeutic Vulnerabilities in Diffuse Intrinsic Pontine Gliomas. *Cancer Res* 79, 4026–4041 (2019).

209. Davies, G., Boeree, M., Hermann, D. & Hoelscher, M. Accelerating the transition of new tuberculosis drug combinations from Phase II to Phase III trials: New technologies and innovative designs. *Plos Med* 16, e1002851 (2019).

210. Gotwals, P. *et al.* Prospects for combining targeted and conventional cancer therapy with immunotherapy. *Nat Rev Cancer* 17, 286–301 (2017).

211. Sun, W. *et al.* Synergistic drug combination effectively blocks Ebola virus infection. *Antivir Res* 137, 165–172 (2017).

212. Wood, K. B., Wood, K. C., Nishida, S. & Cluzel, P. Uncovering Scaling Laws to Infer Multidrug Response of Resistant Microbes and Cancer Cells. *Cell Reports* 6, 1073–1084 (2014).

213. Holbeck, S. L. *et al.* The National Cancer Institute ALMANAC: A Comprehensive Screening Resource for the Detection of Anticancer Drug Pairs with Enhanced Therapeutic Activity. *Cancer Res* 77, 3564–3576 (2017).

214. Law, M. R., Wald, N. J., Morris, J. K. & Jordan, R. E. Value of low dose combination treatment with blood pressure lowering drugs: analysis of 354 randomised trials. *Bmj* 326, 1427 (2003).

215. Berenbaum, M. C. What is synergy? *Pharmacol Rev* 41, 93–141 (1989).

216. BLISS, C. I. THE TOXICITY OF POISONS APPLIED JOINTLY1. *Ann Appl Biol* 26, 585–615 (1939).

217. LOEWE, S. The problem of synergism and antagonism of combined drugs. *Arznei-forschung* 3, 285–90 (1953).

218. Yadav, B., Wennerberg, K., Aittokallio, T. & Tang, J. Searching for Drug Synergy in Complex Dose–Response Landscapes Using an Interaction Potency Model. *Comput Struct Biotechnology J* 13, 504–513 (2015).

219. Ianevski, A., He, L., Aittokallio, T. & Tang, J. SynergyFinder: a web application for analyzing drug combination dose–response matrix data. *Bioinformatics* 33, 2413–2415 (2017).

220. Ianevski, A., Giri, A. K. & Aittokallio, T. SynergyFinder 2.0: visual analytics of multi-drug combination synergies. *Nucleic Acids Res* 48, W488–W493 (2020).

221. O'Reilly, M. A., Muller, A. & Hynynen, K. Ultrasound Insertion Loss of Rat Parietal Bone Appears to Be Proportional to Animal Mass at Submegahertz Frequencies. *Ultrasound in Medicine & Biology* 37, 1930–1937 (2011).

222. Hynynen, K., McDannold, N., Vykhodtseva, N. & Jolesz, F. A. Noninvasive MR Imaging–guided Focal Opening of the Blood-Brain Barrier in Rabbits. *Radiology* 220, 640–646 (2001).

223. McDannold, N., Vykhodtseva, N., Raymond, S., Jolesz, F. A. & Hynynen, K. MRI-guided targeted blood-brain barrier disruption with focused ultrasound: Histological findings in rabbits. *Ultrasound in Medicine & Biology* 31, 1527–1537 (2005).

224. Bothe, H. W., Bodsch, W. & Hossmann, K. A. Relationship between specific gravity, water content, and serum protein extravasation in various types of vasogenic brain edema. *Acta Neuropathol* 64, 37–42 (1984).

225. Rousselle, C. *et al.* New advances in the transport of doxorubicin through the blood-brain barrier by a peptide vector-mediated strategy. *Mol. Pharmacol.* 57, 679–686 (2000).

226. Ohnishi, T. *et al.* In vivo and in vitro evidence for ATP-dependency of P-glycoprotein-mediated efflux of doxorubicin at the blood-brain barrier. *Biochem. Pharmacol.* 49, 1541–1544 (1995).

227. Vanan, M. I. & Eisenstat, D. D. DIPG in Children – What Can We Learn from the Past? *Front. Oncol.* 5, v1-17 (2015).

228. Lipsman, N., Mainprize, T. G., Schwartz, M. L., Hynynen, K. & Lozano, A. M. Intracranial Applications of Magnetic Resonance-guided Focused Ultrasound. *Neurotherapeutics* 11, 593–605 (2014).

229. Souweidane, M. M. *et al.* A phase I study of convection enhanced delivery (CED) of 124I-8H9 radio-labeled monoclonal antibody in children with diffuse intrinsic pontine glioma (DIPG). *Journal of Clinical Oncology* 35, 2010–2010 (2017).

230. Bander, E. D. *et al.* Repeat convection-enhanced delivery for diffuse intrinsic pontine glioma. *J Neurosurg Pediatrics* 26, 661–666 (2020).

231. Anderson, R. C. E. *et al.* Convection-enhanced delivery of topotecan into diffuse intrinsic brainstem tumors in children. *J Neurosurg Pediatr* 11, 1–7 (2013).

232. Kroin, J. S. & Penn, R. D. Intracerebral chemotherapy: chronic microinfusion of cisplatin. *Neurosurgery* 10, 349–354 (1982).

233. McDannold, N., Arvanitis, C. D., Vykhodtseva, N. & Livingstone, M. S. Temporary Disruption of the Blood-Brain Barrier by Use of Ultrasound and Microbubbles: Safety and Efficacy Evaluation in Rhesus Macaques. *Cancer Research* 72, 3652–3663 (2012).

234. Jolesz, F. A. & Hynynen, K. H. *MRI-Guided Focused Ultrasound Surgery*. (CRC Press, 2007).

235. Burgess, A., Shah, K., Hough, O. & Hynynen, K. Focused ultrasound-mediated drug delivery through the blood–brain barrier. *Expert Review of Neurotherapeutics* 15, 477–491 (2015).

236. Nhan, T., Burgess, A., Lilge, L. & Hynynen, K. Modeling localized delivery of Doxorubicin to the brain following focused ultrasound enhanced blood-brain barrier permeability. *Phys Med Biol* 59, 5987–6004 (2014).

237. Buitrago, M. Short and long-term motor skill learning in an accelerated rotarod training paradigm. *Neurobiology of Learning and Memory* 81, 211–216 (2004).

238. Huang, Y., Alkins, R., Schwartz, M. L. & Hynynen, K. Opening the Blood-Brain Barrier with MR Imaging–guided Focused Ultrasound: Preclinical Testing on a Trans–Human Skull Porcine Model. *Radiology* 282, 123–130 (2017).

239. Kovacs, Z. I. *et al.* Disrupting the blood–brain barrier by focused ultrasound induces sterile inflammation. *Proc. Natl. Acad. Sci. U.S.A.* 114, E75–E84 (2017).

240. McMahon, D., Bendayan, R. & Hynynen, K. Acute effects of focused ultrasound-induced increases in blood-brain barrier permeability on rat microvascular transcriptome. *Scientific Reports* 1–15 (2017) doi:10.1038/srep45657.

241. Rahman, A., Carmichael, D., Harris, M. & Roh, J. K. Comparative Pharmacokinetics of Free Doxorubicin and Doxorubicin Entrapped in Cardiolipin Liposomes. *Cancer Research* 46, 2295–2299 (1986).

242. Park, J., Aryal, M., Vykhodtseva, N., Zhang, Y.-Z. & McDannold, N. Evaluation of permeability, doxorubicin delivery, and drug retention in a rat brain tumor model after ultrasound-induced blood-tumor barrier disruption. *Journal of Controlled Release* 250, 77–85 (2017).

243. Siddaway, R. & Hawkins, C. Modeling DIPG in the mouse brainstem. *Neuro-Oncology* 22, 307–308 (2020).

244. Hoffman, L. M. *et al.* Spatial genomic heterogeneity in diffuse intrinsic pontine and midline high-grade glioma: implications for diagnostic biopsy and targeted therapeutics. *Acta Neuropathol Commun* 1–8 (2015) doi:10.1186/s40478-015-0269-0.

245. Kemper, K. *et al.* Intra- and inter-tumor heterogeneity in a vemurafenib-resistant melanoma patient and derived xenografts. *Embo Mol Med* 7, 1104–1118 (2015).

246. Swanton, C. Intratumor Heterogeneity: Evolution through Space and Time. *Cancer Res* 72, 4875–4882 (2012).

247. Tacar, O., Sriamornsak, P. & Dass, C. R. Doxorubicin: an update on anticancer molecular action, toxicity and novel drug delivery systems. *J Pharm Pharmacol* 65, 157–170 (2013).

248. Zheng, F. *et al.* Mechanism and current progress of Poly ADP-ribose polymerase (PARP) inhibitors in the treatment of ovarian cancer. *Biomed Pharmacother* 123, 109661 (2020).

249. Haan, R. de *et al.* Study protocols of three parallel phase 1 trials combining radical radiotherapy with the PARP inhibitor olaparib. *Bmc Cancer* 19, 901 (2019).

250. Murai, J. *et al.* Stereospecific PARP Trapping by BMN 673 and Comparison with Olaparib and Rucaparib. *Mol Cancer Ther* 13, 433–443 (2014).

251. Shen, Y. *et al.* BMN 673, a Novel and Highly Potent PARP1/2 Inhibitor for the Treatment of Human Cancers with DNA Repair Deficiency. *Clin Cancer Res* 19, 5003–5015 (2013).

252. K, S., Shahneen *et al.* The poly(ADP-ribose) polymerase inhibitor niraparib (MK4827) in BRCA mutation carriers and patients with sporadic cancer: a phase 1 dose-escalation trial. *Lancet Oncol* 14, 882–892 (2013).

253. Lasic, D. D. & Needham, David. The "Stealth" Liposome: A Prototypical Biomaterial. *Chem Rev* 95, 2601–2628 (1995).

254. Plosker, G. L. Pegylated Liposomal Doxorubicin. *Drugs* 68, 2535–2551 (2008).

255. Xing, M., Yan, F., Yu, S. & Shen, P. Efficacy and Cardiotoxicity of Liposomal Doxorubicin-Based Chemotherapy in Advanced Breast Cancer: A Meta-Analysis of Ten Randomized Controlled Trials. *Plos One* 10, e0133569 (2015).

256. Tangpong, J. *et al.* Adriamycin-induced, TNF-α-mediated central nervous system toxicity. *Neurobiol Dis* 23, 127–139 (2006).

257. Kondo, A., Inoue, T., Nagara, H., Tateishi, J. & Fukui, M. Neurotoxicity of adriamycin passed through the transiently disrupted blood-brain barrier by mannitol in the rat brain. *Brain Res* 412, 73–83 (1987).

258. Neuwelt, E. A., Glasberg, M., Frenkel, E. & Barnett, P. Neurotoxicity of chemotherapeutic agents after blood-brain barrier modification: Neuropathological studies. *Ann Neurol* 14, 316–324 (1983).

259. Aryal, M., Vykhodtseva, N., Zhang, Y.-Z. & McDannold, N. Multiple sessions of liposomal doxorubicin delivery via focused ultrasound mediated blood–brain barrier disruption: A safety study. *J Control Release* 204, 60–69 (2015).

260. Yu, F. T. H., Chen, X., Wang, J., Qin, B. & Villanueva, F. S. Low Intensity Ultrasound Mediated Liposomal Doxorubicin Delivery Using Polymer Microbubbles. *Mol Pharmaceut* 13, 55–64 (2016).

261. Löscher, W. & Potschka, H. Blood-brain barrier active efflux transporters: ATP-binding cassette gene family. *Neurorx* 2, 86–98 (2005).

262. Bansal, T., Jaggi, M., Khar, R. & Talegaonkar, S. Emerging Significance of Flavonoids as P-Glycoprotein Inhibitors in Cancer Chemotherapy. *J Pharm Pharm Sci* 12, 46–78 (2009).

263. Schinkel, A. H. & Jonker, J. W. Mammalian drug efflux transporters of the ATP binding cassette (ABC) family: an overview. *Adv Drug Deliver Rev* 55, 3–29 (2003).

264. Cho, H. *et al.* Localized Down-regulation of P-glycoprotein by Focused Ultrasound and Microbubbles induced Blood-Brain Barrier Disruption in Rat Brain. *Sci Rep-uk* 6, 31201 (2016).

265. Aryal, M. *et al.* Effects on P-Glycoprotein Expression after Blood-Brain Barrier Disruption Using Focused Ultrasound and Microbubbles. *PLoS ONE* 12, e0166061-15 (2017).

266. Choi, H., Lee, E.-H., Han, M., An, S.-H. & Park, J. Diminished Expression of P-glycoprotein Using Focused Ultrasound Is Associated With JNK-Dependent Signaling Pathway in Cerebral Blood Vessels. *Front Neurosci-switz* 13, 1350 (2019).

267. III, F. E. & JP, E. *Cancer Medicine. Principles of Dose, Schedule, and Combination Therapy. Chapter 44*. (2003).

268. Boshuizen, J. & Peeper, D. S. Rational Cancer Treatment Combinations: An Urgent Clinical Need. *Mol Cell* 78, 1002–1018 (2020).

269. Beccaria, K. *et al.* Opening of the blood-brain barrier with an unfocused ultrasound device in rabbits: Laboratory investigation. *J Neurosurg* 119, 887–898 (2013).

270. Carpentier, A. *et al.* Clinical trial of blood-brain barrier disruption by pulsed ultrasound. *Sci Transl Med* 8, 343re2-343re2 (2016).

271. Beccaria, K. *et al.* Blood-brain barrier disruption with low-intensity pulsed ultrasound for the treatment of pediatric brain tumors: a review and perspectives. *Neurosurg Focus* 48, E10 (2020).

272. Reid, Y., Storts, D., Riss, terry & Minor, L. Authentication of Human cell Lines by STR DNA Profiling Analysis. *The Assay Guidance Manual* (2004).

273. Veringa, S. J. E. *et al.* In Vitro Drug Response and Efflux Transporters Associated with Drug Resistance in Pediatric High Grade Glioma and Diffuse Intrinsic Pontine Glioma. *PLoS ONE* 8, e61512-10 (2013).

274. Diaz, R. J. *et al.* Focused ultrasound delivery of Raman nanoparticles across the blood-brain barrier: Potential for targeting experimental brain tumors. *Nanomedicine: Nanotechnology, Biology, and Medicine* 10, e1075–e1087 (2014).

275. O'Reilly, M. A. & Hynynen, K. A PVDF Receiver for Ultrasound Monitoring of Transcranial Focused Ultrasound Therapy. *IEEE Trans. Biomed. Eng.* 57, 2286–2294 (2011).

276. Wu, S.-K. *et al.* Characterization of Different Microbubbles in Assisting Focused Ultrasound-Induced Blood-Brain Barrier Opening. *Scientific Reports* 1–11 (2017) doi:10.1038/srep46689.

277. Wei, G., Xiao, S., Si, D. & Liu, C. Improved HPLC method for doxorubicin quantification in rat plasma to study the pharmacokinetics of micelle-encapsulated and liposome-encapsulated doxorubicin formulations. *Biomed. Chromatogr.* 22, 1252–1258 (2008).

278. Arnold, R. D., Slack, J. E., B, R. S. J. of C. & 2004. Quantification of Doxorubicin and metabolites in rat plasma and small volume tissue samples by liquid chromatography/electrospray tandem mass spectroscopy. *Elsevier* 808, 141–152 (2004).

279. Halvorson, K. G. *et al.* A High-Throughput In Vitro Drug Screen in a Genetically Engineered Mouse Model of Diffuse Intrinsic Pontine Glioma Identifies BMS-754807 as a Promising Therapeutic Agent. *PLoS ONE* 10, e0118926-16 (2015).